1. Introduction

The management of high-level radioactive wastes (HLW) is one of the most important issues relevant to the nuclear energy production. The Accelerator Driven Systems (ADS) are proposed to burn or transmute HLW coming from the Light Water Reactors (LWR) in low level wastes [1][2][3]. In fact, these systems have worldwide attracted the attention of scientific community because the possibility to reduce the radio-toxicity as well as the amount of radioactive waste for future generations.

The neutronic characteristics of the reactor are conceived as to efficiently incinerate long lived fission products by transmutation, in order to reduce the need for very long term geological disposal of nuclear wastes produced in the nuclear reactor fuel cycle .
Because its good chemical, thermo physical and neutronic properties, the Lead Bismuth Eutectic (LBE) alloy was proposed as one of the most promising target materials as well as coolant for the reactor.

Moreover pure lead is under investigation as cooling fluid for a Fast Lead Reactor belonging to the family of the forth generation reactors under development in these last years[4]. The aim of these reactors is to increase the exploitation of the nuclear fuel while cutting the waste produced.

From the beginning of the most important research programs on these systems, the Lead Bismuth Eutectic (LBE) alloy was proposed as one of the most promising target materials as well as coolant for the reactor. Then, since 1999, several small devices as well as large loops and facilities have been operated at the CR ENEA Brasimone, one of the most active research centre in the European Union on the field of the heavy liquid metal technology, to perform experimental activities aimed to investigate thermal hydraulics, heat exchange, science of materials, qualification of components and operational procedures topics related to the use of LBE.

The present work is focused on the development of technology to be applied to the liquid metal systems.
Starting to the experience gained during the PEC experience on the Sodium reactors, the ENEA's know-how moved to the analysis of new problems. As a matter of fact, technological issues related to the use of standard components in a LBE environment, such as pressure transmitters, flow meters and pumps, often required to look for particular adjustments or new technical solution [5][6][7][8]

In this work the Oxygen monitor and control and the investigation about a black powder found in the facilities will be presented.

Another task performed, in the thermal-hydraulic field, is to investigate whether the gas injection technology (known as gas-lift, and used in the chemical industry) was adaptable to a liquid metal pool configuration. With particular interest to the two phase flow experiments that were prepared and performed. The results have been analized.

Finally the use of liquid metals for an industrial application is presented. In particular, the use of the sodium-potassium alloy for pressure transducer applications.

The experimental activities herein reported and discussed were often contemporary.

Bibliografy

[1] C. Rubbia, S. Buono, Y. Kadi and J.A. Rubio "Fast Neutron Incineration in the Energy Amplifier as an Alternative to Geologic Storage: the Case of Spain", European Organisation for Nuclear Research, CERN/LHC/97-01 (EET), Geneva, 17th February 1997.

[2] C. Rubbia, J.A. Rubio, S. Buono, F. Carminati, N. Fiétier, J. Galvez, C. Gelès, Y. Kadi, R. Klapisch, P. Mandrillon, J.P. Revol and Ch. Roche "Conceptual Design of a Fast Neutron Operated High Power Energy Amplifier", European Organisation for Nuclear Research, CERN/AT/95-44 (ET), Geneva, 29th September, 1995.CIRCE 1 SIEX 0001, General Specifications rev 2 (in Italian), 8/06/2001, DNU-STL

[3] M. Carta, G. Gherardi, S. Buono, L. Cinotti "The Italian R&D and Industrial Program for an Accelerator Driven System Experimental Plant", IAEA-TCM on Core Physics and Engineering Aspects of Emerging Nuclear energy Systems for Energy Generation and Transmutation, ANL, Argonne (USA), 28 November - 1 December 2000.

[4] A Technology Road map for Generation IV Nuclear Energy Systems – U.S. DOE Nuclear Energy Research Advisory Committee and Generation Iv International Forum – December 2002

[5] Zucchini, P. Agostini, E. Baicchi, J. Nucl. Mater. 336 (2005) 291-298

[6] Y. Dai, F. Barbagallo, F. Gröschel, J. Nucl. Mater. 317 (2003) 252-255.

[7] C. Foletti, G. Scaddozzo, G. Bertacci, A. Gessi, P. Agostini, M. Tarantino, G. Benamati, ENEA experience in LBE technology, 3rd International Workshop on Spallation Materials Technology IWSMT – 7, May 29 - June 3, 2005 - Thune, Switzerland.

[8] G. Scaddozzo, "Studio teorico-sperimentale per la caratterizzazione di materiali strutturali in metallo liquido per applicazioni ADS (Accelerator Driven System)", 2002 – Politecnico di Torino - Tesi di Laurea.

2. Experimental activities on the gas enhanced circulation performed in CIRCE

Summary

The injection of gas to promote the circulation of a process fluid is a well known technique usually adopted in chemical reactors (namely Air-lift Reactors) to realize oxidation process, chlorination process and the treatment of liquid waste. This technique allows the primary coolant circulation with a plant simplification in respect to the use of mechanical pumps, avoiding rotating parts immersed in the liquid. So, it is particularly suitable in the case of dangerous or corrosive liquids. Moreover, it can be assumed as an intrinsic safety system to ensure a required level of liquid flow rate, at least for short periods of time, since the gas can be pressurized and stored in suitable bottles.
The possibility to enhance the circulation of LBE by gas injection is considered of interest for the assessment of the feasibility and operability of an ADS prototype as well as for small modular reactors cooled by liquid metal. For instance, the reference design of the LBE cooled XADS developed by ANSALDO adopts a gas lift system for the primary coolant circulation.
However, the reliability of this technique has never been proved on significant scale in the case of LBE. So, in the frame of the TECLA project and ENEA's research on ADS, dedicated experimental campaigns on the CIRCE facility have been carried out in order to characterize the technique.

However, no information about the void fraction in the two phase region, nor about the influence of the temperature on the behaviour of the system were available.
So, even if the main objective of the first experimental campaign was reached, a lack of information remained. For this reason, a second campaign was planned and carried out in CIRCE with the same test configuration, in order to obtain the data needed to fully characterize the technique. In this case more attention was paid to the fluid-dynamic of the system, since the riser was instrumented to perform differential pressure measurements. Moreover, the second tests was performed under isothermal condition but for different level of temperature, in the range from 200 to 320 °C, to investigate the influence of the temperature on the system.
The present chapter is focused on the results obtained during this first and second experimental campaign performed on the CIRCE facility.

The experimental campaigns performed

Two experimental campaign have been performed on the CIRCE facility to characterize the gas lifting technique applied to the liquid LBE.
The first experimental campaign was aimed to demonstrate the reliability of the technique, so the tests were mainly focused on the possibility to entrain steady states of LBE circulation by the injection of gas and on the obtainment of a characteristic curve able to predict the LBE flow rate as function of the gas flow rate. For this reason a wide range of flow rate was investigated.
The tests were performed under isothermal condition at 200 °C. In fact, this temperature is the cold shutdown temperature in the LBE cooled XADS concept, and was considered as reference temperature during the pre-test analysis performed by Ansaldo using the RELAP 5/mod3.2.2 beta code.
The second experimental campaign has been carried out to better understand the fluid-dynamic of the system and the dependence from the temperature. So, the main objectives of the new tests were to measure the loss of pressure in the two phase region and to investigate the influence of the temperature on the LBE circulation. Therefore, the tests were performed once again under isothermal conditions, but were repeated at different temperatures in the range from 200 to 320 °C.
The loss of pressure measured along the riser allowed to estimate the void fraction distribution in the two phase region by means of the "manometric method".

Description of the test section

Figure 2-1 illustrates the handling of the test section used for the enhanced circulation tests in the PEC building, just before its insertion in the main vessel. When the test section is inserted, the configuration is able to reproduce the velocity fields expected for the reference XADS plant [1][2]. A schematic view of the test section is reported in Figure 2-2. It basically consists of:

- Riser : a pipe geometrically equal to one of the 22 pipes that forms the reference plant riser (diameter=202.7mm, height=3854mm). Since this element is scaled 1:1, the flow mapping achievable by tests will be easily applicable to the full scale reference plant. Inside the riser is housed the gas injection pipe, ending with the injector (see Figure 2-3). The outlet of the riser is 150 mm under the free level of the liquid metal (stagnant conditions).

- Dead Volume : delimited by the test section support ferrule, it maintains the real highness of the full scale dead volume, whereas the cross section is scaled 1:22. At present the dead volume do not take active place in the test run, so it is unfilled of lead-bismuth. However, future tests to study the coupled behaviour of the riser-dead volume system have been already planned.

- Fitting volume : It consists of a cylindrical volume delimited by two circular plates (diameter=982mm), 225mm spaced. It joints the feeding conduit to the riser. This element is designed and scaled to represent the upper plenum of the core, fitting the core outlet to the riser inlet.

- Feeding conduit : The Venturi-Nozzle flow meter is installed on the conduit, as well as a drilled disk, downstream the flow meter. The hole manufactured on this disk is calculate to provide a loss of head suitable to simulate the one relevant to the full scale core.

- Down comer : is the outer side of the test section, interested by the descending path of the LBE during the test. It is scaled to represent 1/17 of the full scale downcomer, so it is characterized

by a cross section of 0.7m^2

As previously reported, the riser houses the gas injection line that belongs to the GIS. This line ends at the bottom of the riser with an "U" bend on which the injection nozzle is installed. In Figure 2-3 the bottom part of the riser and a particular of the nozzle are depicted.

Figure 2-1- Handling of the test section N° 2 in the PEC building and inserting it inside the main vessel.

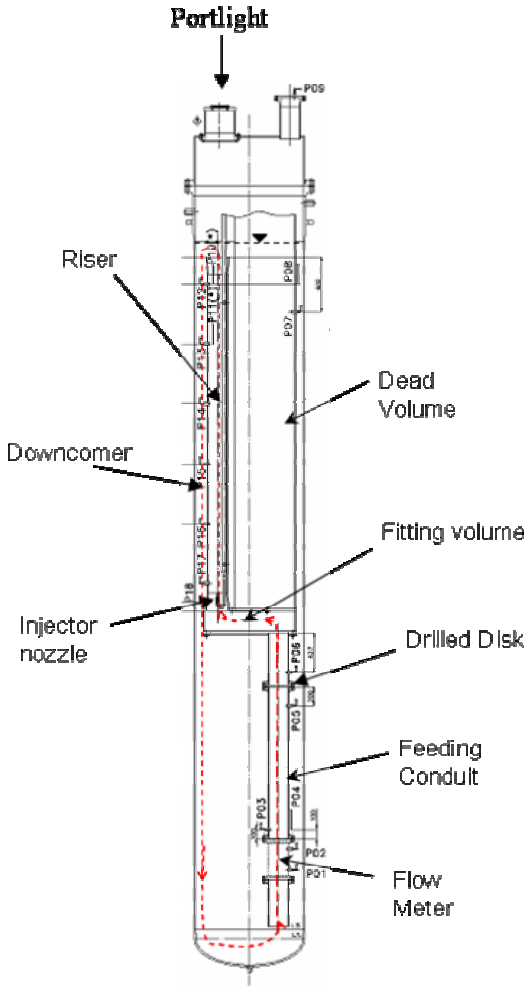

Figure 2-2– Test configuration in S100 during the gas enhanced circulation tests; the red dot line indicates the flow path during the tests

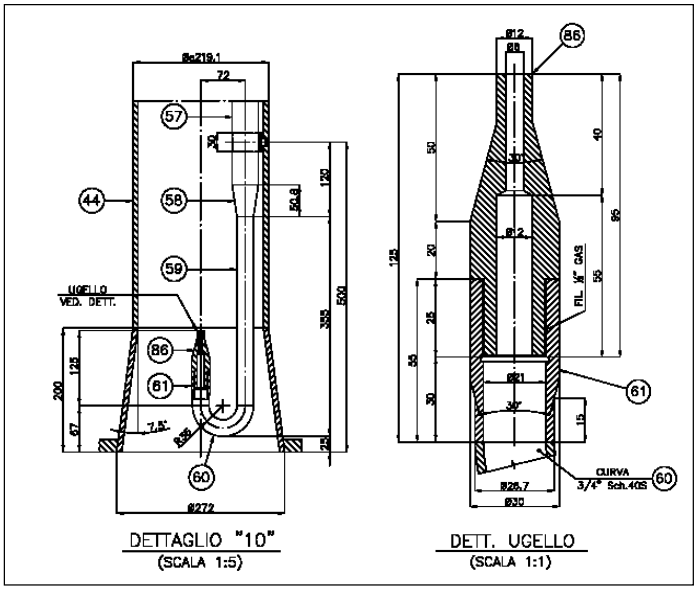

Figure 2-3- Assembling drawing of the bottom part of the riser, housing the gas injector pipe (on the left) and particular of the injector (on the right)

Test procedure

The test procedure [1] consists in to inject a selected gas flow rate through a nozzle located at the bottom of the riser. The gas flow rate can be regulated by mean of regulation valves, by pass line and, of course, a suitable management of the positive displacement blowers. In this way the range from 0.056 to 7.5 Nl/s of gas flow rate can be covered.
Therefore, to investigate the behaviour of the system, several gas flow rate have been injected in the riser in order to entrain an LBE flow rate. So, steady states characterized by different liquid flowrate have been obtained. Each steady state has been maintained at least for 20 – 25 min., then the gas flow rate has been changed (increased or decreased to obtain a new steady state).

The tests have been performed under isothermal conditions (during the second experimental campaign at different LBE temperatures); When the isothermal conditions at the selected temperature are reached, a gas flow rate is injected from the bottom of the riser through the injection nozzle (6 mm inner diameter, as shown in Figure 2-3) with a pressure of about 5 bar, needed to override the backpressure of the LBE column. Then, after a quick transient, a steady flow condition for the liquid metal is obtained. During the test, all the measurement performed are saved by the DAS, so data about the transient behaviour of the system are available too.

The scattering of the experimental data is mainly due to the uncertainness relevant to the adopted instrumentations.

Flow rate measurements

The gas flow rate injected during the tests has been measured by dedicated flow meters. In fact, the ARS includes three gas flow meters.
Concerning these gas flow meters, they have different measurement range; in particular, the first flow meter (FT208A) works in the range [0.056÷0.56 Nl/s], the second (FT208B) in the range[0.35÷3.5 Nl/s], while the third works in the range [2.2÷22 Nl/s].

So, after the gas flow rate to inject has been chosen, it is possible to switch on the appropriate flow meter, opening the associated insulation valve and excluding the other ones.

The output signal from the selected flow meter is corrected by the DAS and then stored. The correction follows the equation:

$$Q_{eff} = Q_m \cdot C_T \cdot C_p \qquad (1)$$

Q_{eff} is the corrected data, to be stored.
Q_m is the measured value
C_T and C_p are the temperature and the pressure coefficient respectively, defined as follow:

$$C_T = \sqrt{\frac{T_t}{T_e}} \qquad C_p = \sqrt{\frac{P_e}{P_t + 1}}$$

where:
T_t = 423 K (calibration temperature)
P_t = 4 bar(g)
T_e is the operating temperature (upstream the flow meter)
P_e is the operating pressure (upstream the flow meter)

The correction takes in account the difference between the calibration conditions and the operating conditions, in terms of pressure and temperature.

The LBE flow rate have been measured by the Venturi-Nozzle flow meter installed on the feeding conduit.
During each steady state obtained, the measurements of differential pressure through the flow meter have been preformed by the DPMS and stored by the DAS. The data have been then converted in flow rate values using the characteristic curve carried out by the calibration test of the Venturi-Nozzle flow meter.
However, the DPT cell (DPT002) related to the flow meter, has been checked and calibrated in order to obtain the gravimetric head between the two taps installed on the Venturi-Nozzle, like in the case of all the other DPT cells .

Differential pressure measurement

The measurement of differential pressure is demanded to the DMPS, that make use of bubble tubes and DPT cells at room temperature. The bubble tubes are continuously fed by a low argon flow rate, that is controlled by means of gas flow controllers placed in dedicated room nearby the main vessel. The flow rate adopted is in the range found to be suitable for the system during its calibration.

Results achieved in the first test campaign

In the first experimental campaign for each injected Ar flow rate a flow of LBE has been measured, but the system shows different behaviour for Ar flow rates higher or lower than 1 Nl/s.
With gas flow rates lower than 1 Nl/s the system shows a “pulsed” behaviour, with both the flow rates characterized by periodical oscillations. In fact, even if the test starts fixing a selected value of

the gas flow rate, both flow rates quickly undergo a periodical and quite regular oscillation, characterized by a frequency of about 30 mHz.
This behaviour is probably related to the bubbles growth and to the detachment mechanism, where a partial refilling of the injection line by LBE could take place at low gas flow rates. The detachment of gas corresponds to the peaks detected measuring the pressure in the injection line, downstream the gas flow meter. When the release of gas occurs, the pressure in the line decrease rather quickly, as far as the gas flow rate; this suggests an entry of liquid metal inside the injector. Then the pressure increase slowly and the liquid metal is pushed outside the injector until the next release of gas.
An analogous behaviour has been already noted during similar tests performed in water-air systems. In those cases, the phenomena was related to the coalescence that occurs to the bubbles at low gas flow rate all around the mixer, before the detachment.

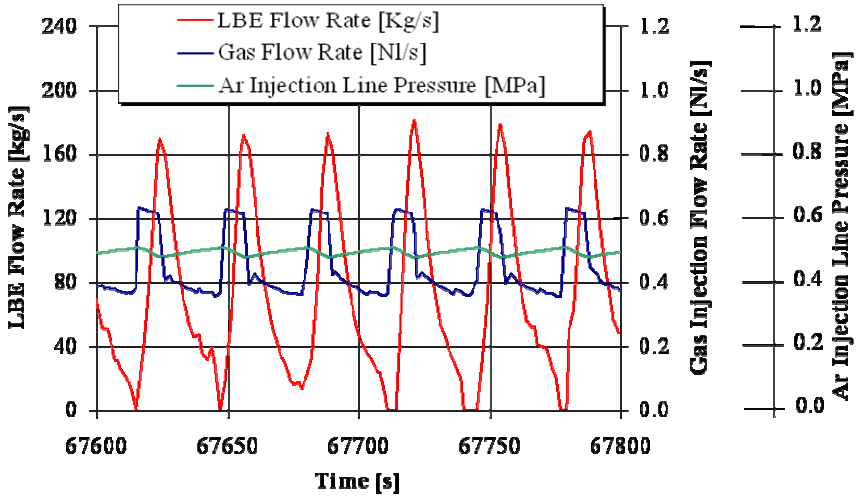

Figure 2-4- Pulsed behaviour showed by the system for injected flow rates lower than 1 Nl/s

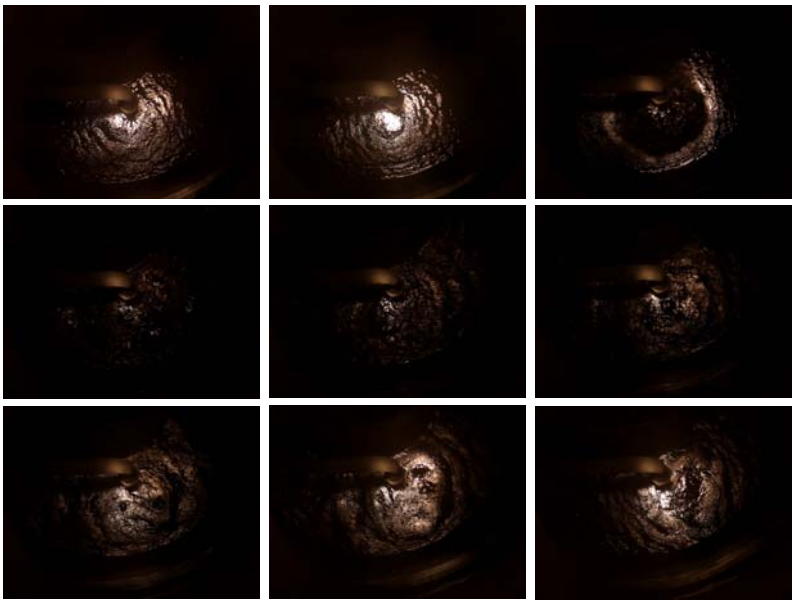

Figure 2-5– Evolution of the free level above the riser during a test at low gas flow rate; the snapshot were took, from the left to the right, at 1s, 5s, 10s, 12s, 18s, 22s, 24s, 26s, 30s; note as the injected gas begins to came out suddenly (3rd photogram) and continues for about 10sec. Then the free level returns to its initial quite smooth appearance.

In the case of gas flow rate higher than 1 Nl/s, the results obtained are absolutely different. In fact, a steady circulation of LBE has been achieved during every test performed. For instance, several

steady states characterised by different flow rates can be noted in Figure 2-6, where both the gas and the liquid metal flow rates realised during one of the test performed are displayed. However, the transition between each steady state has not been displayed in the picture.

A wide range of liquid flow rates has been investigated; in fact, has been possible to obtain flow rates of LBE in the range from ~100 to ~230kg/s, as the gas injected was in the range from ~1 to 7.4 Nl/s (from ~2 to ~13 g/s).

Moreover, the repeatability of the results has been confirmed, since they have been obtained during five different stage of test and for each one a wide flowrate range has been investigated, as can be noted in Figure 2-7; here the results obtained are depicted in terms of liquid versus gas flow rate.

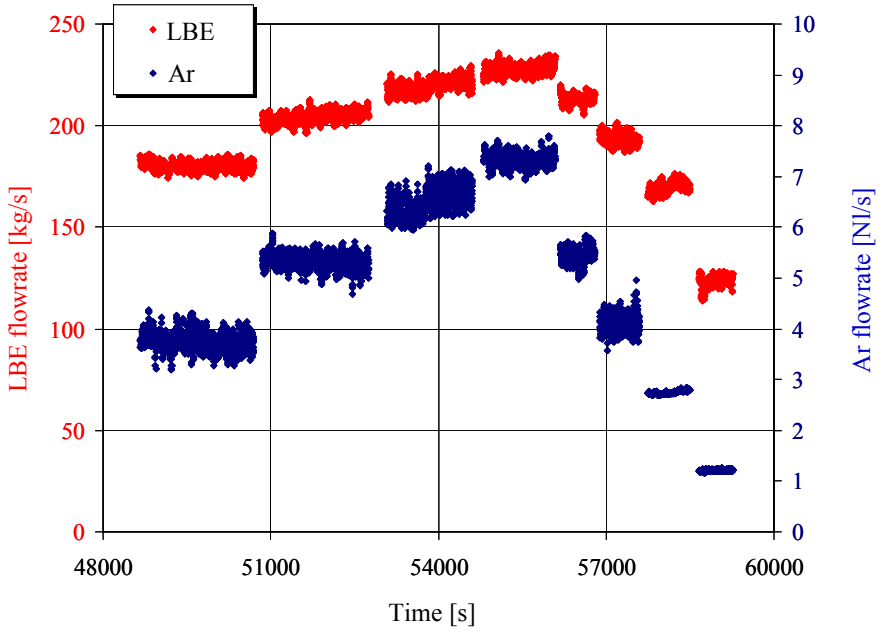

Figure 2-6-Several steady state of circulation obtained during the tests; the two flow rates are depicted

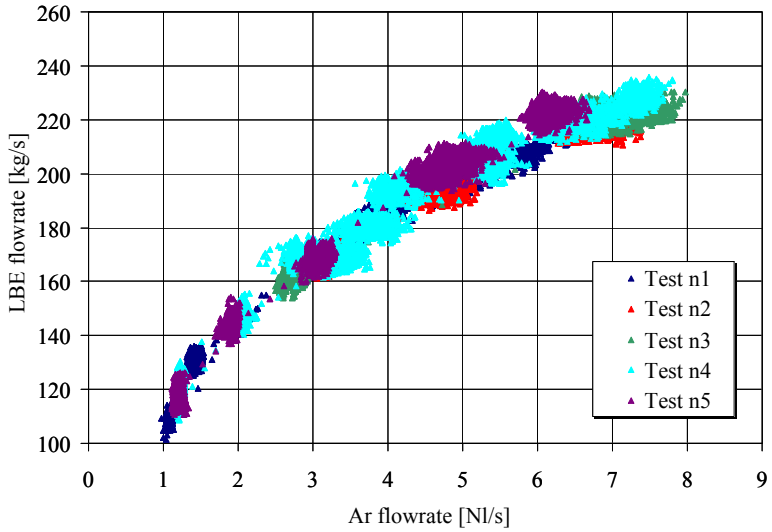

Figure 2-7– Experimental data obtained during the tests performed; a good repeatability can be noted

To easily deal with the data, for each steady state reached a mean value of the two flow rates has been calculated, as reported in the tables from 1 to 5. These data have been plotted in a bi-

logarithmic diagram as shown in Figure 2-6; as can be noted, the liquid flow rate increases as the gas flow rate increases and the two quantity seems to be related by a power law like the following:

$$\dot{m}_l = A \cdot \left(\dot{m}_g\right)^b \qquad (2)$$

where the exponent "b" is close to 0.33.

Test n1		
Steady states	Ar flow rate [g/s]	LBE flow rate [kg/s]
1	2,1	119
2	3,4	144,7
3	5,4	169,4
4	8,3	199,5
5	8,8	205,7
6	11	222,6
7	2,2	118,5

Table 1-Average values of gas and liquid flow rates characterizing the steady states obtained within test n1

Test n2		
Steady states	Ar flow rate [g/s]	LBE flow rate [kg/s]
8	3,7	148,6
9	5,6	168,5
10	6,7	180,2
11	9,5	204,4
12	13	227,7
13	9,7	213,3
14	7,3	193,6
15	4,9	169,9
16	2,2	123,5
17	4,9	161,4

Table 2-Average values of gas and liquid flow rates characterizing the steady states obtained within test n2

Test n3		
Steady states	Ar flow rate [g/s]	LBE flow rate [kg/s]
18	13,1	222,7
19	12,2	221,4
20	11,7	222,1
21	5,8	169,2
22	8,3	192,8
23	12,2	217,8

Table 3-Average values of gas and liquid flow rates characterizing the steady states obtained within test n3

Test n4		
Steady states	Ar flow rate [g/s]	LBE flow rate [kg/s]
24	2,6	131,5
25	5,2	166,2
26	6,5	179,6
27	2,4	128,7

28	5,4	168,9
29	6,8	184,4
30	9,2	199,9

Table 4-Average values of gas and liquid flow rates characterizing the steady states obtained within test n4

Test n5		
Steady states	Ar flow rate [g/s]	LBE flow rate [kg/s]
31	10,6	209
32	8,1	193,1
33	6,2	177,5
34	3,7	147,3
35	1,9	108,3

Table 5-Average values of gas and liquid flow rates characterizing the steady states obtained within test n5

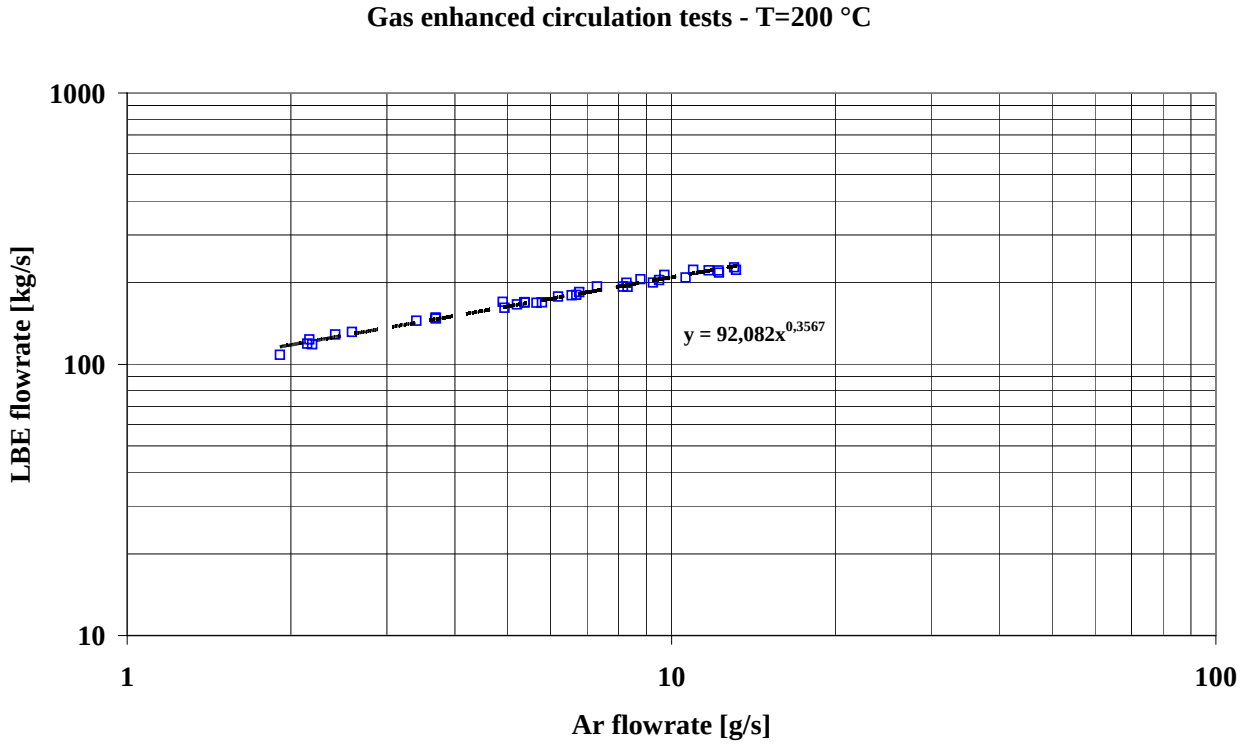

Figure 2-8-LBE flow rate as function of the gas flow rate. The data are best-fitted by a power law

This behaviour can be explained as follow. Since the system is under steady state conditions, the momentum equation, integrated along the flow path, gives:

$$\Delta p_{DF} = \Delta p_{fric} \qquad (3)$$

where Δp_{DF} is the "driving force", while Δp_f represents the total pressure drop along the flow path. The driving force can be also written as:

$$\Delta p_{DF} = H \cdot g \cdot \Delta\rho \qquad (4)$$

where H is the total head upon the injector nozzle and $\Delta\rho$ is the density difference between the liquid in the downcomer and the fluid flowing in the riser.

The density difference can be expressed as:

$$\Delta\rho = \rho_l - \rho_m = \rho_l - \left[\rho_l \cdot (1-\alpha) + \alpha \cdot \rho_g\right] \qquad (5)$$

where ρ_l is the density of the LBE in the downcomer, while ρ_m is the average density of the two phase mixture in the riser, defined by the void fraction α, and ρ_g is the gas density.
The gas density is strongly dependent by pressure, that is function of position along the riser. Then, it will change as the gas rise up in the riser. Moreover, since the gas injection line runs all along inside the riser driving the gas to its bottom part, it is reasonable to assume that the rising gas is in thermal equilibrium with the liquid metal. Under this hypothesis we can express the gas density by the ideal gas law as:

$$\rho_g(z) = \frac{p(z)}{R^* \cdot T} \tag{6}$$

In the former equation z is the curvilinear coordinate along the riser axis (z=0 is the injection point), while R* is the argon gas constant (208.21 J/kgK).

In order to simplify the model is useful to define an average gas density $\bar{\rho}_g$, as the density calculated at the average pressure in the riser, that means the pressure at z=H/2. Since the void fraction is little, the average pressure can be estimated as:

$$\bar{p} = p_0 + \rho_l \cdot g \cdot \frac{H}{2} \tag{7}$$

where p_0 is the cover gas pressure. The equation (5) become

$$\Delta\rho = \rho_l - \bar{\rho}_m = \alpha \cdot (\rho_l - \bar{\rho}_g) \tag{8}$$

and is possible to write:

$$\Delta p_{DF} = \alpha \cdot (\rho_l - \bar{\rho}_g) \cdot g \cdot H \tag{9}$$

Now, introducing the flow quality x and the slip ratio S, defined respectively as:

$$x = \frac{\dot{m}_g}{\dot{m}_g + \dot{m}_l} \qquad S = \frac{u_g}{u_l} = \frac{1-\alpha}{\alpha} \cdot \frac{x}{1-x} \cdot \frac{\rho_l}{\rho_g}$$

the previous equation can be written as:

$$\Delta p_{DF} = \frac{(\rho_l - \bar{\rho}_g) \cdot g \cdot H}{1 + S \cdot \frac{1-x}{x} \cdot \frac{\bar{\rho}_g}{\rho_l}} \tag{10}$$

Let's now to consider the right side of equation (2); Δp_{fric} represents the total pressure drop along the flow path. Since the localized loss of head in the two phase region are negligible, it can be written as:

$$\Delta p_{fric} = \frac{1}{2}\left[\sum f_{l0} \frac{L}{D_e} \rho_l \bar{v}^2 + \sum K \rho_l \bar{v}^2 + \Phi_{l0}^2 \cdot f_{l0} \frac{L_r}{D_{e,r}} \rho_l \cdot \bar{v}^2 \right] \tag{11}$$

where the first term represents the distributed loss of head by friction through the single phase region, the second term the loss localized in singularities and the third represents the loss of head by distributed friction along the two phase region.
The first and the third terms are characterized by an own characteristic length, equivalent diameter, flow pattern and then friction coefficient.
Introducing the liquid flow rate, equation. (12) can be written as:

$$\Delta p_{fric} = \left(\sum f_{l0} \frac{L}{D_e} + \sum K + \Phi_{l0}^2 f_{l0} \frac{L_r}{D_{e,r}} \right) \frac{\dot{m}_l^2}{2\rho_l A_r^2} = K_t \frac{\dot{m}_l^2}{2\rho_l A_r^2} \tag{12}$$

where A_r is the riser cross section.
Since the single phase as well as the two phase distributed pressure losses are negligible in comparison to the singular pressure drops along the path, K_t is not dependent from the flow rate.
Moreover, under the tested condition it can be assumed that:

$$1 + S \cdot \frac{\dot{m}_l}{\dot{m}_g} \cdot \frac{\bar{\rho}_g}{\rho_l} \approx S \cdot \frac{\dot{m}_l}{\dot{m}_g} \cdot \frac{\bar{\rho}_g}{\rho_l} \tag{13}$$

so it is possible to write:

$$\frac{(\rho_l - \bar{\rho}_g)\cdot g \cdot H}{S \cdot \frac{\dot{m}_l}{\dot{m}_g}\cdot\frac{\bar{\rho}_g}{\rho_l}} = K_t \cdot \frac{\dot{m}_l^2}{2\cdot\rho_l \cdot A_r^2} \tag{14}$$

Rearranging the previous equation we have

$$\frac{2\cdot(\rho_l - \bar{\rho}_g)\cdot g \cdot H \cdot \rho_l^2 \cdot A_r^2}{S \cdot K_t \cdot \bar{\rho}_g}\cdot \dot{m}_g = \dot{m}_l^3 \tag{15}$$

and then

$$\dot{m}_l = A \cdot \left(\dot{m}_g\right)^{0.33}$$

where

$$A = \frac{2\cdot(\rho_l - \bar{\rho}_g)\cdot g \cdot H \cdot \rho_l^2 \cdot A_r^2}{S \cdot K_t \cdot \bar{\rho}_g} \tag{16}$$

can be considered as a constant.

Comparison with the pre-test analysis

The experimental results obtained during this first experimental campaign were compared to the results obtained in the pre-test analysis performed by Ansaldo [3]. These were carried out using the Relap5/mod 3.2.2 Beta code in the version developed by Ansaldo to be used with liquid metals.
The LBE flow rate values predicted by the Relap5 [7] code, at several Ar flow rates, have been compared to the values given, for the same input gas flow rates, by the equation obtained as best fit of the experimental data. The result is shown in Figure 2-9; As can be noted, the code is in a rather good agreement with the experimental results, even if it slightly overestimates the data, at least in the investigated range of flow rates.

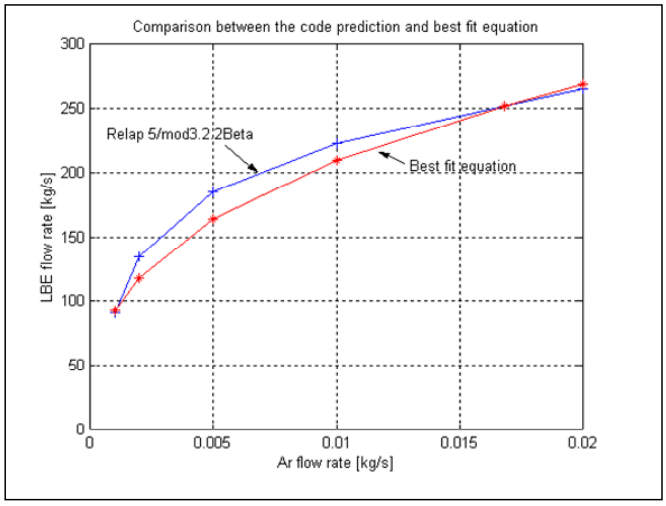

Figure 2-9-Comparison between the LBE flow rate predicted by the Relap5 code and the best-fit curve of the experimental results

Modify Test configuration

The test configuration adopted for this second campaign was identical to the one used during the previous tests. However, the DPMS has been improved, installing several pressure transducers intended to perform pressure loss measurement both in the single phase and in the two phase region of the test section. In particular, five DPT cells (namely from DPT05 to DPT09) have been used to measure the two phase pressure loss along the riser during the experiments, while another DPT cell (the DPT03) was used to measure the single phase pressure drop throughout the drilled disk (hole

size: Φ = 127 mm), mounted downstream the flow meter, simulating the pressure loss through the reference XADS core. A scheme of the test section with the new instrumentation is shown in Figure 2-10.

Before to run with the tests, all the instrumentation was checked under stagnant condition, to control its calibration.

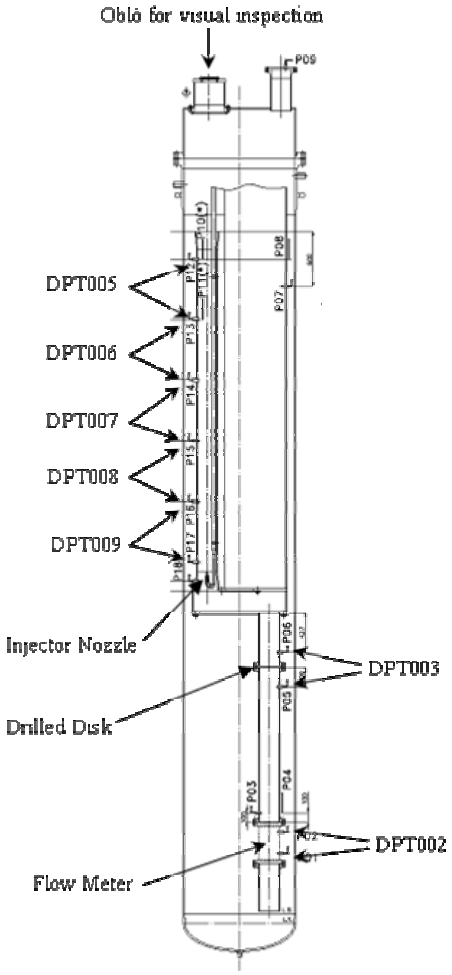

Figure 2-10– Test configuration during the second experimental campaign; the DPMS has been improved by the installation of new DPT cells connected to the bubble tubes as shown in the picture.

Concerning the bubble tubes which supplies DPT03 transducer , the measured value of 364 mm has been adopted as distance between the two bubble tube taps. It should be noted as this initial check was repeated at each temperature, to verify possible derive of the signal due to thermal effects. Anyway, the temperature does not affect very much the performance of the measurement system. For instance, in Figure 2-11 the results obtained in the case of DPT03 are shown.

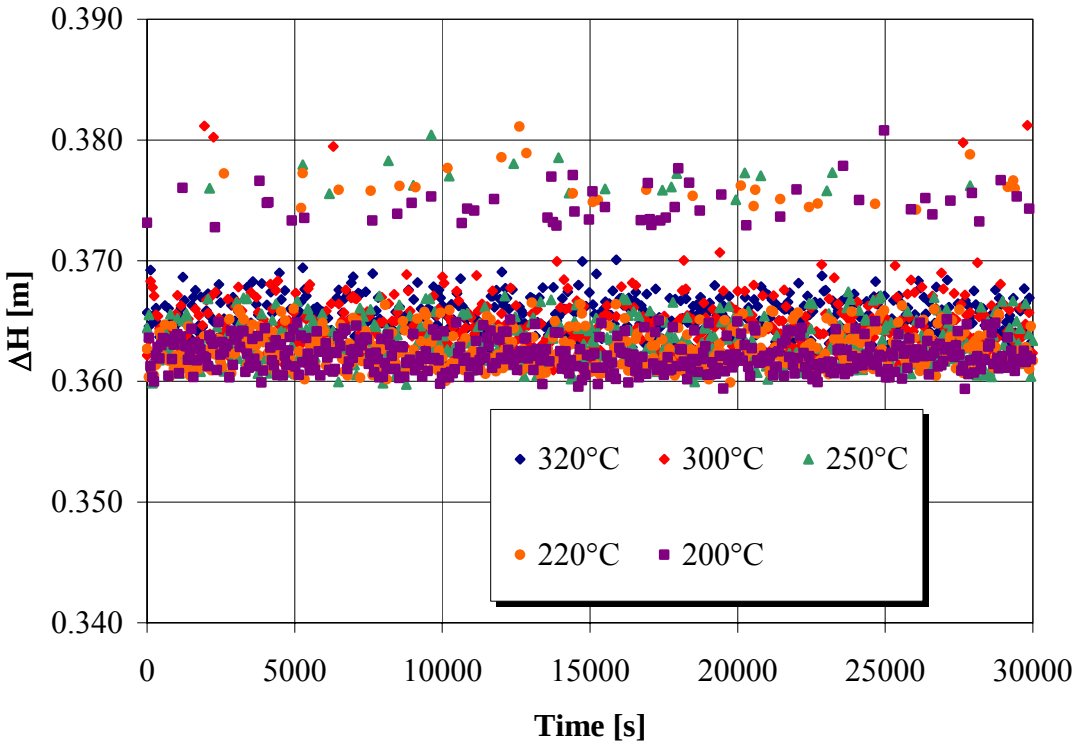

Figure 2-11- Distance between the bubble tube taps which supplies the DPT03, evaluated under stagnant conditions at different temperatures. As expected, the temperature plays an unimportant role on the performance of the measurement system

Results obtained within the second experimental campaign

All the results obtained during the previous campaign were confirmed by the new tests. In fact, several steady-states of liquid metal circulation have been obtained in the pool at all the temperatures investigated. Indeed, as in the previous tests, the occurrence of instability phenomena have been noted at very low gas flow rate.

Flow rates

Figure 2-12 shows the trend of both gas injected and the LBE flow rates, during the test performed at 320°C. Either steady states and transient are clearly recognizable, being the two flow rates roughly constant during the steady states. As can be noted, the transient between two subsequent steady states of the systems is very quick (less then 30 s), indicating a low mechanical inertia of the system. For example, the data concerning the gas and LBE flow rate in table from 6 to 9 are listed, each table reporting the results relevant to each test temperature investigated.

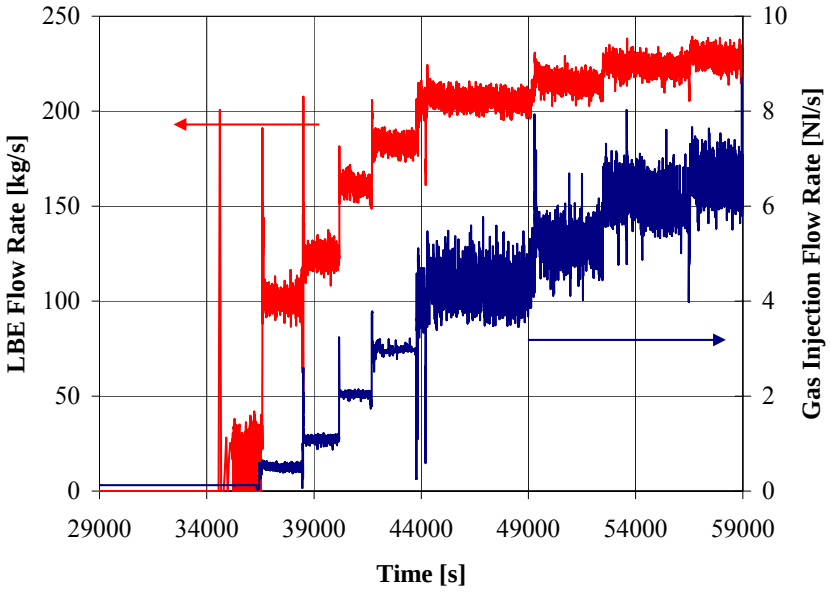

Figure 2-12- Trend of the LBE flow rate as function of the trend of argon flow rate, for gas enhanced circulation tests performed to 320°C

$T_{average}$ [°C]= 200 °C		
$\dot{M}_{Ar}$ [Nl/s]	$\dot{M}_{Ar}$ [kg/s]	$\dot{M}_{LBE}$ [kg/s]
0,52	9,19E-04	79,8
1,08	1,90E-03	110,6
2,05	3,60E-03	148,6
3,17	5,57E-03	173,1
4,16	7,32E-03	193,2
4,96	8,71E-03	201,9
5,83	1,02E-02	224,3
7,16	1,26E-02	221,9

Table 6-Gas and LBE flow rates for the tests performed at 200 °C

$T_{average}$ [°C]= 220 °C		
$\dot{M}_{Ar}$ [Nl/s]	$\dot{M}_{Ar}$ [kg/s]	$\dot{M}_{LBE}$ [kg/s]
1,07	1,88E-03	112,5
2,08	3,65E-03	151,8
2,08	3,65E-03	153,6
2,95	5,19E-03	172,3
3,14	5,53E-03	175,7
4,07	7,16E-03	195,9
3,97	6,98E-03	193,1
5,01	8,80E-03	206,0
4,79	8,42E-03	201,8
6,92	1,22E-02	222,2

Table 7-Gas and LBE flow rates for the tests performed at 220 °C

$T_{average}$ = 250 °C		
$\dot{M}_{Ar}$ [Nl/s]	$\dot{M}_{Ar}$ [kg/s]	$\dot{M}_{LBE}$ [kg/s]
0,59	1,03E-03	87,6
1,05	1,84E-03	111,0
1,07	1,88E-03	114,7
2,06	3,63E-03	152,4
2,01	3,54E-03	151,5
2,96	5,21E-03	176,9
2,98	5,23E-03	171,0
4,05	7,12E-03	198,5
4,88	8,58E-03	207,1
6,31	1,11E-02	221,7

Table 8-Gas and LBE flow rates for the tests performed at 250 °C

$T_{average}$ = 320 °C		
$\dot{M}_{Ar}$ [Nl/s]	$\dot{M}_{Ar}$ [kg/s]	$\dot{M}_{LBE}$ [kg/s]
0,50	8,84E-04	101,1
1,10	1,94E-03	123,4
1,04	1,82E-03	118,6
2,05	3,60E-03	161,4
2,15	3,77E-03	161,7
2,98	5,24E-03	182,9
2,99	5,26E-03	178,5
4,27	7,50E-03	205,8
5,23	9,20E-03	215,1
4,73	8,32E-03	209,5
5,98	1,05E-02	224,2
6,43	1,13E-02	227,9
0,52	9,11E-04	87,5
0,98	1,72E-03	115,5
1,03	1,81E-03	118,8
2,06	3,62E-03	161,4
2,04	3,59E-03	158,6
3,05	5,36E-03	181,9
3,07	5,40E-03	181,4
4,29	7,54E-03	207,2
4,69	8,25E-03	210,0
6,85	1,21E-02	231,6

Table 9-Gas and LBE flow rates for the tests performed at 320 °C

The flow rate data have been plotted in Figure 2-13; as expected, the data follow a progression similar to what already found in the previous tests. Moreover, as can be noted in the picture, the

entrained flow rate increases with the temperature. Actually, as the temperature increases the dynamic viscosity of the LBE decrease and the viscous pressure losses decrease too.

However, as can be noted, the dependence from temperature is rather weak, this behaviour suggesting that the viscous pressure losses are small in comparison to the singular pressure drops, in accordance with the hypothesis made to justify the power law relation found between the two flow rates. In fact, increasing the temperature from 200°C to 320°C, the dynamic viscosity of the LBE undergoes a reduction of about 30%; so, for the same driving force in the systems (that means the same void fraction distribution along the riser) a stronger increment in the flow rate should be expected.

By the way, this increment can be expected to be not so high since the singularities play a key role in the system. Therefore, it seems reasonable to consider that the singular pressure drops along the flow path are predominant compared to the viscous ones. So the LBE flow rate is quite independent from the temperature.

In Figure 2-13 the data obtained during the first experimental campaign on gas enhanced circulation have been plotted too (mark 200_old); It should be noted as the new and the old data are in very good agreement, confirming a good repeatability of the results.

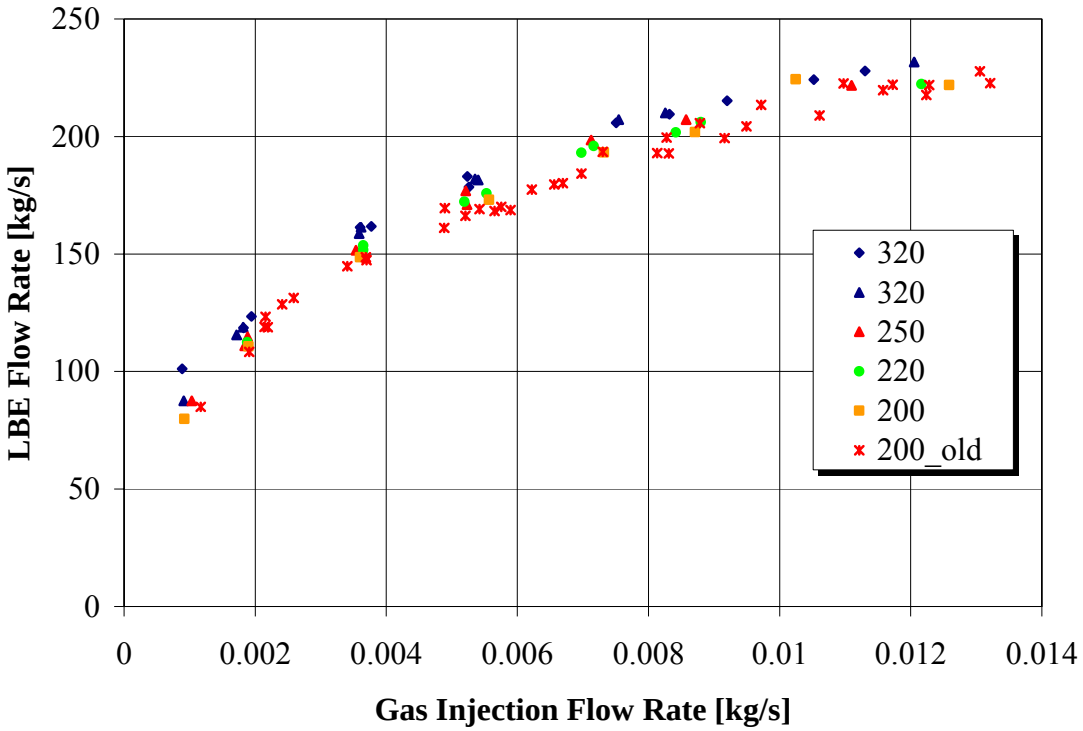

Figure 2-13-LBE flow rate as function of the gas flow rate at different temperatures. Data marked 200_old have been obtained during the first experimental campaign.

Local pressure drop

Let's now to consider the loss of pressure along the path. Differential pressure measurement have been performed during the tests in the single phase as well as in the two phase region. In particular, concerning the single phase region, interest has been paid to the Δp measured through a drilled disk, whose hole have been calibrated to simulate the loss of head representative of the reference core [4].
In the tables from 10 to 13 the average value of the differential pressure measured by the DPMS across the calibrate hole are reported, together with the corresponding liquid flow rate.
Also, the data reported in the first of these tables, relevant to the test temperature of 200 °C, have been displayed in Figure 2-14. As could be expected, the data follows a quite parabolic progression as function of the liquid flow rate: the quantity measured represents the total pressure drop between the two taps used by the DPMS; however, the loss of pressure is practically due to the singularity represented by the orifice. So, it is possible to express the quantity measured in terms of local pressure drop as:

$$\Delta p_{measured} = \Delta p_{loc} = \frac{1}{2} K_{loc} \frac{\dot{M}_{LBE}^2}{\rho_l A^2} \qquad (17)$$

where K_{loc} is the loss coefficient related to the singularity, while A is the cross section of the feeding conduit.
The K_{loc} coefficient is usually considered independent from the flow rate, depending only from the particular kind of singularity, such as contraction, expansion, bend or orifice (like in this case) or some others. Thus, at constant temperature, the ratio between the ΔP and the square of the flow rate should be constant:

$$\frac{\Delta p_{loc}}{\dot{M}^2} = \frac{1}{2} \frac{K_{loc}}{\rho_l A^2} = constant \qquad (18)$$

However, plotting the right side of equation (18) versus the flow rate, it is possible to note as this ratio increases with the flow rate; therefore, K_{loc} is dependent from the flow rate (see Figure 2-15). This is probably due to fact that upstream the orifice the flow, even if turbulent, is not completely developed yet.

$T_{average}$ = 200 °C	
$\dot{M}_{LBE}$ [Kg/s]	Δp_{fric} [Pa]
79,8	4126
110,6	8160
148,6	15182
173,1	20935
193,2	26967
201,9	29828
224,3	33348
221,9	37066

Table 10- Pressure drop measured through the drilled disk, for tests performed to 200°C.

$T_{average}$ = 220 °C	
$\dot{M}_{LBE}$ [Kg/s]	Δp_{fric} [Pa]
112,5	8540
151,8	15781
153,6	16303
172,3	20669
175,7	21558
195,9	27839
193,1	26924
206,0	31262
201,8	29884
222,2	37284

Table 11 - Pressure drop measured through the drilled disk, for tests performed to 220°C.

$T_{average}$ = 250 °C	
$\dot{M}_{LBE}$ [Kg/s]	Δp_{fric} [Pa]
87,6	4868
111,0	8432
114,7	8775
152,4	16093
151,5	15744
176,9	21871
171,0	20465
198,5	28519
207,1	31505
221,7	36978

Table 12- Pressure drop measured through the drilled disk, for tests performed to 250°C.

$T_{average}$ = 320 °C	
$\dot{M}_{LBE}$ [Kg/s]	Δp_{fric} [Pa]
101,1	6295
123,4	10000
118,6	8720
161,4	17655
161,7	17798
182,9	23203
178,5	22323
205,8	30761
215,1	34263
209,5	32368
224,2	37803
227,9	39517
87,5	4710
115,5	8631
118,8	9034
161,4	17569
158,6	17213
181,9	23208
181,4	23092
207,2	31225
210,0	32436
231,6	41063

Table 13- Pressure drop measured through the drilled disk, for tests performed to 320°C.

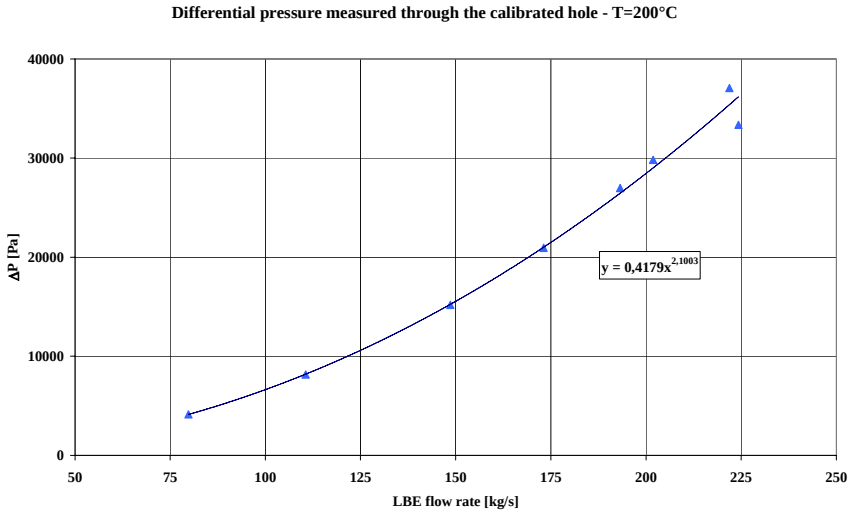

Figure 2-14– Loss of pressure through the drilled disk. The data follow a parabolic trend as function of the liquid flow rate

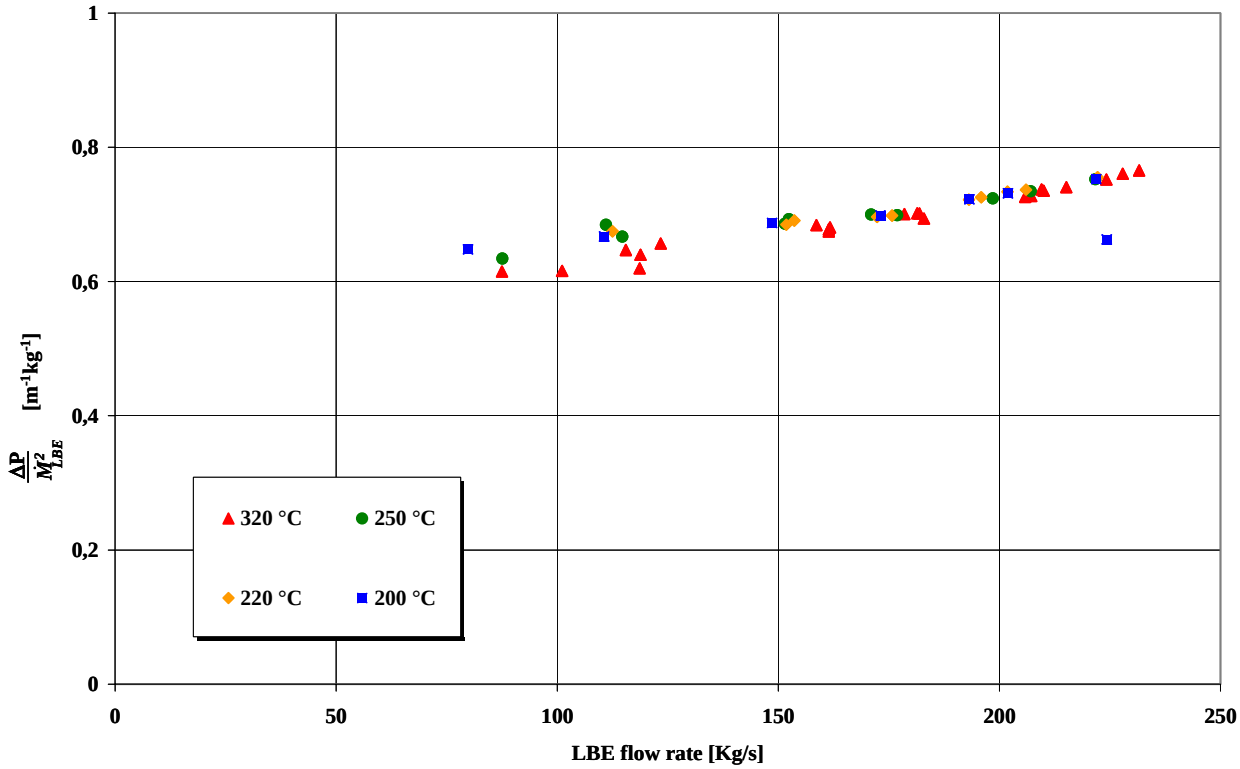

Figure 2-15– Left side of equation (5.2) plotted versus the liquid flow rate. The temperature is not important and the data follow a linear trend.

Pressure drop and void distribution along the riser

Now let's to consider the loss of pressure along the riser. As previously reported, the riser can be considered formed by five consecutive branch, each one related to a DPT cell, as shown in Figure 2-16. Note as the numeration of the branch follows the same numeration adopted for the DPT cells, to avoid confusion.
Under stagnant condition the differential pressure (Δp_m) measured by each DPT cell is given by:

$$\Delta p_m = p_+ - p_- = \rho_{LBE} g h \qquad (19)$$

Where h is the distance between the two bubble tube taps considered. This is a direct consequence of the calibration adopted for the DPT cells.
Under steady circulation, the measured Δp_m can be expressed as:

$$\Delta p_m = p_+ - p_- = \Delta p_{fric} + \Delta p_{acc} + \Delta p_{grav} \qquad (20)$$

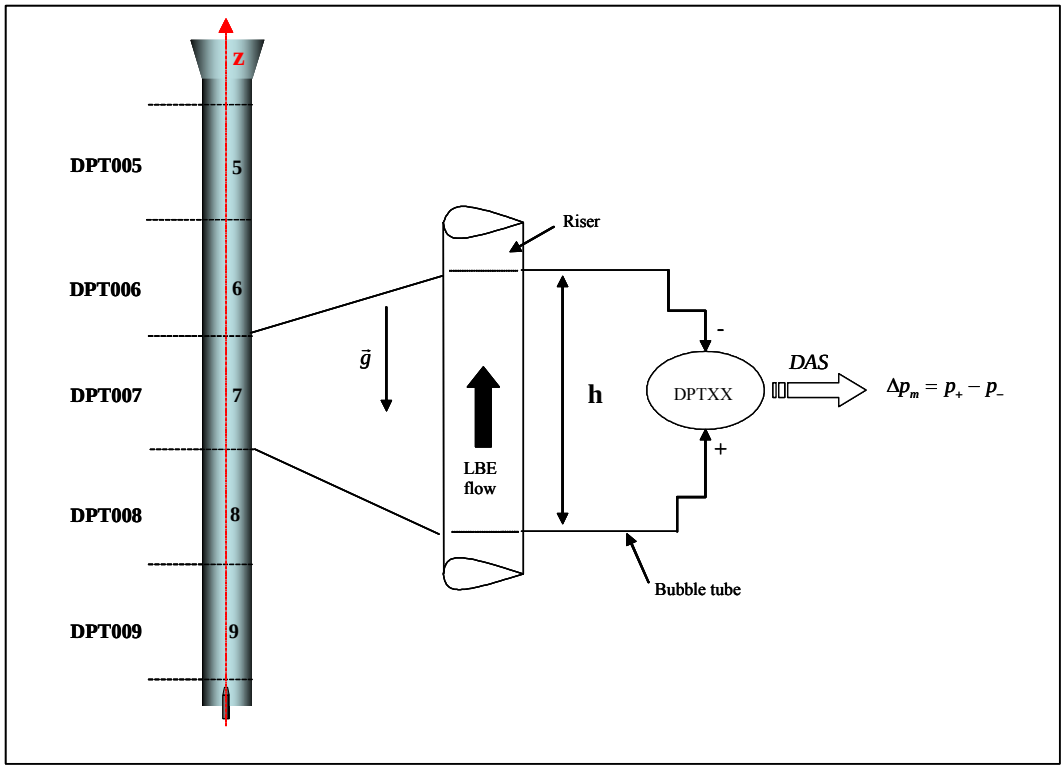

Figure 2-16- Sketch of the five branches that form the riser

In Figure 2-17 the data relevant to the DPT07 are displayed. Again, as can be noted, the temperature doesn't play a dominant role on the behaviour of the system. In Figure 2-18 the data obtained by the tests performed at 250 °C, relevant to the central part of the riser (DPT06, 7 and 8) have been displayed. As shown, the loss of pressure increase as the depth increases.

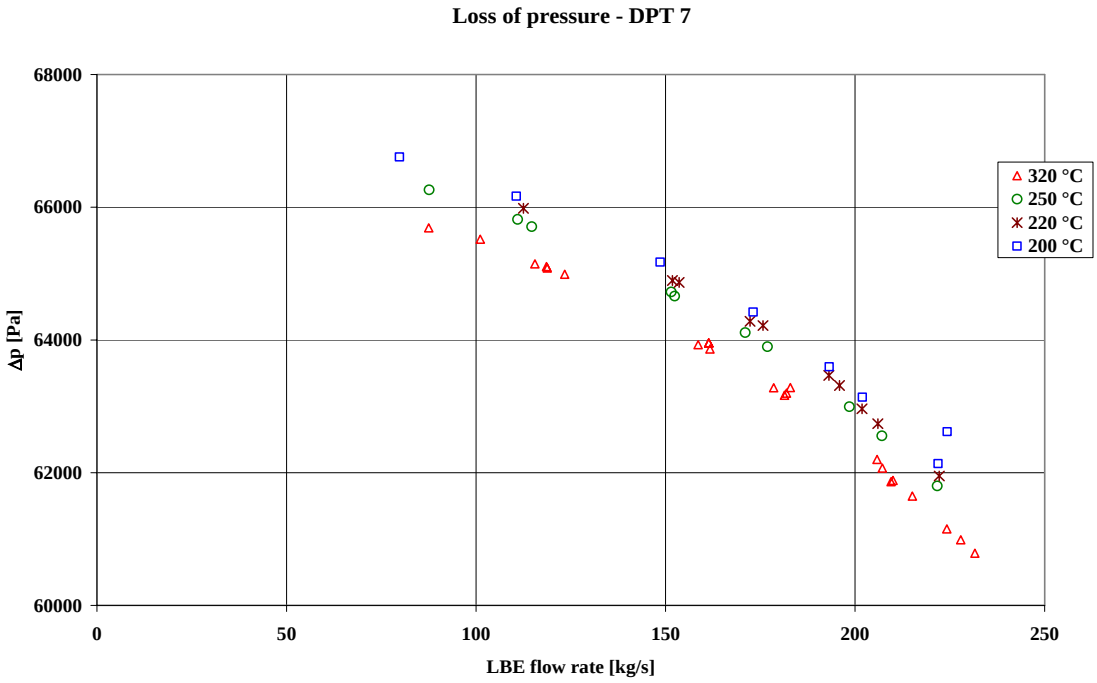

Figure 2-17– Dependence from temperature of the loss of pressure measured across the riser central branch (branch n.7)

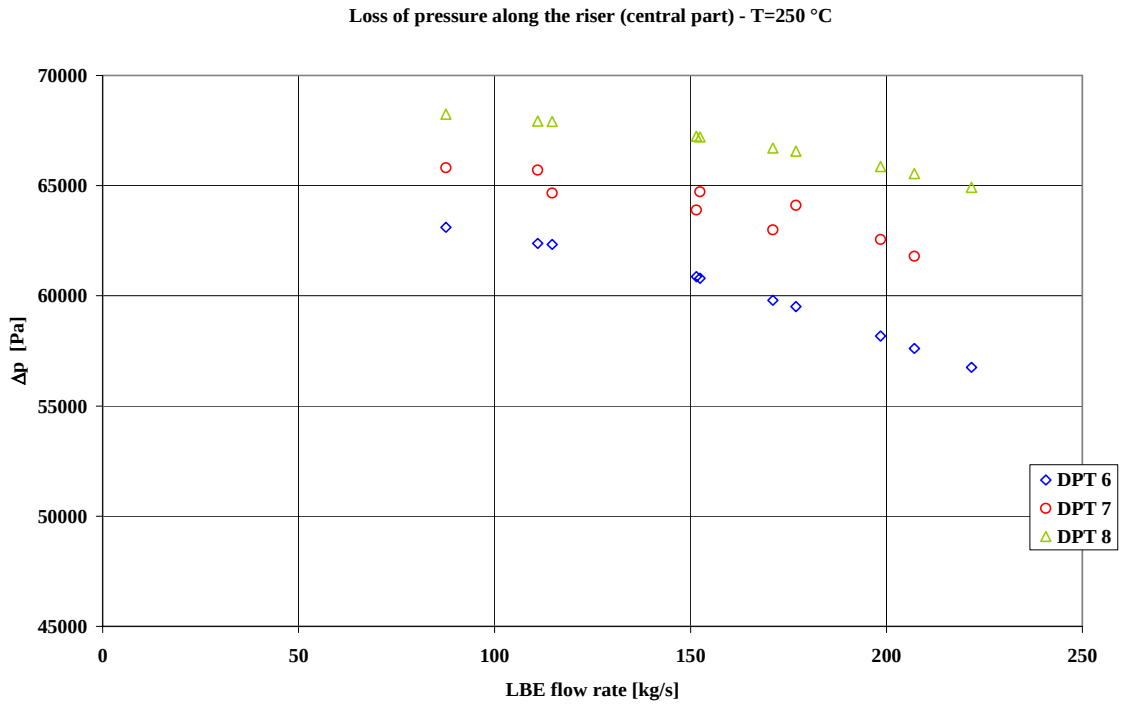

Figure 2-18– Loss of pressure measured across the riser medium branches

Equation (19) expresses the pressure drop in the channel as the sum of three components, due to friction, acceleration and gravity; these three terms can be expressed as:

$$\Delta p_{fric} = \phi_{lo}^2 f_{lo} \frac{h}{D_{ris}} \frac{G_m^2}{2\rho_l} \tag{21}$$

$$\Delta p_{acc} = \left(\frac{G_m^2}{\rho_m^+} \right)_- - \left(\frac{G_m^2}{\rho_m^+} \right)_+ \tag{22}$$

$$\Delta p_{grav} = \bar{\rho}_m g h \tag{23}$$

where the following definition have been assumed:

- $\bar{\rho}_m = \bar{\alpha}\bar{\rho}_g + (1-\bar{\alpha})\rho_l$ is the mixture average density in the considered part of the riser;
- $\bar{\alpha} = \frac{1}{h}\int_h \alpha dz$ is the average void fraction in the considered part of the riser;
- $\bar{\rho}_g = \frac{1}{h}\int_h \rho_g dz$ is the average density of the gas in the considered part of the riser;
- h is the length of the considered part of the riser;
- $G_m = \frac{\dot{M}_m}{A_{ris}} = \frac{\dot{M}_l + \dot{M}_g}{A_{ris}}$ is the mixture mass flux;
- $A_{ris} = \pi \frac{D_{ris}^2}{4}$ is the riser flow area;
- $\frac{1}{\rho_m^+} = \frac{1}{G_m^2}\left[\rho_g \alpha u_g^2 + \rho_l (1-\alpha) u_l^2\right]$ is the area averaged dynamic density;
- u_g is the gas phase velocity;

- u_l is the gas phase velocity;
- ϕ_{lo}^2 is the two phase friction multipliers;
- f_{lo} is the friction coefficient for liquid single phase flow calculated at the same mass flow of the mixture G_m.

The loss of pressure measured along the riser can be used to estimate the void fraction distribution. In fact, the gravimetric term in equation (18) depends from the density of the two phase mixture, that is directly connected to the void fraction.
First of all, let's to calculate the other two terms of equation 18, the Δp_{fric} and the Δp_{acc}.

Concerning the Δp_{fric}, the Lockart-Martinelli method [5] has been used for the evaluation of the two phase friction multipliers and, finally, the friction factor for the single phase flow can be calculated by the Churchill correlation [6] utilizable for laminar and turbulent flows.

To estimate Δp_{acc} a *separate flow model* has been adopted. In general two-fluid cases, both velocities and temperatures of the two phases may be different. However, in the separate flow models, thermodynamic equilibrium is assumed, while the phase velocities are different.
Under the hypothesis of a one-dimensional system, for each cross section along the riser it is possible to write:

$$xG_m = \rho_g \alpha u_g \tag{29}$$

$$(1-x)G_m = \rho_l (1-\alpha) u_l \tag{30}$$

and substituting in the ρ_m^+ definition:

$$\frac{1}{\rho_m^+} = \frac{x^2}{\rho_g \alpha} + \frac{(1-x)^2}{\rho_l (1-\alpha)} \tag{31}$$

So, the acceleration pressure drop in each part of the riser is given by:

$$\Delta p_{acc} = G_m^2 \left[\left(\frac{x^2}{\rho_g \alpha} + \frac{(1-x)^2}{\rho_l (1-\alpha)} \right)_- - \left(\frac{x^2}{\rho_g \alpha} + \frac{(1-x)^2}{\rho_l (1-\alpha)} \right)_+ \right] \tag{32}$$

This equation require the value of the void fraction in the section where the bubble tubes are installed; to overcome this difficulty the value of the void fraction in the lower section (α_-) is substituted with the average value obtained from the preceding branch of riser, while the value in the upper section (α_+) is substituted with the value obtained from the subsequent one. Moreover, the average value of the gas density in the riser will be used. Using this approximations, equation (32) for the nth part of riser can be written as:

$$\Delta p_{acc,n} = G_m^2 \left[\left(\frac{x^2}{\rho_g \alpha} + \frac{(1-x)^2}{\rho_l (1-\alpha)} \right)_{n-1} - \left(\frac{x^2}{\rho_g \alpha} + \frac{(1-x)^2}{\rho_l (1-\alpha)} \right)_{n+1} \right] \tag{33}$$

However, for the first and the last part of the riser is not possible to use this equation, but it is reasonable to assume that the value of Δp_{acc} in these two branches is of the same order of magnitude of the other branches.
As first approximation it is possible to assume that

$$\Delta p_{grav} >> \left(\Delta p_{fric} + \Delta p_{acc} \right) \tag{34}$$

for each branch of the riser, so that:

$$\Delta p_m = p_+ - p_- \Rightarrow \Delta p_{grav} = \bar{\rho}_m g h \qquad (35)$$

Therefore, using the loss of pressure measured it is possible to evaluate an average density for the mixture in each branch of the riser. Then, using the definition of the mixture density, it is possible to estimate the average void fraction in each part of the riser:

$$\bar{\alpha} = \frac{\rho_{LBE} - \bar{\rho}_m}{\rho_{LBE} - \bar{\rho}_g} \qquad (36)$$

Knowing the void fraction in each branch of the riser it is then possible to estimate the acceleration pressure drop by equation (32). The values obtained by the calculations performed are of the same order of magnitude found in the case of the friction term.

It is possible to note as the assumption 16 is reasonable, being the contribution of the friction and the acceleration terms negligible respect to the total pressure drop measured. Moreover, a correction that could take in account these two terms seems to be not useful, since the total contribution of these quantities to the whole loss of pressure is of the same order of the error related to the use of bubble tubes.

The tables from 12 to 15 report the values estimated for the void fraction in the five branch of the riser for some the tests performed.

Figure 2-19 shows the void fraction evaluated in the five branches of the riser during the test at 200 °C, while Figure 2-20 shows the void fraction evaluated for the central branch of the riser in all the tests performed. As already discussed, the test temperature is a parameter which doesn't affect the behaviour of the system. The void fraction data can be considered related to the gas flow rate by a power law.

$T_{average}$ = 250 °C						
$\dot{M}_{LBE}$ [kg/s]	$\dot{M}_{Ar}$ [kg/s]	α 5	α 6	α 7	α 8	α 9
87,6	1,03E-03	0,017	0,012	0,009	0,003	0,002
111,0	1,84E-03	0,031	0,023	0,016	0,008	0,006
114,7	1,88E-03	0,033	0,024	0,018	0,008	0,004
152,4	3,63E-03	0,061	0,048	0,033	0,018	0,010
151,5	3,54E-03	0,061	0,047	0,032	0,018	0,008
176,9	5,21E-03	0,083	0,068	0,045	0,028	0,014
171,0	5,23E-03	0,077	0,064	0,042	0,026	0,011
198,5	7,12E-03	0,106	0,089	0,058	0,038	0,018
207,1	8,58E-03	0,114	0,098	0,065	0,043	0,019
221,7	1,11E-02	0,132	0,112	0,076	0,052	0,022

Table 14– Values of the void fraction estimated in the five branches of the riser for tests performed at 320°C.

$T_{average}$ = 320 °C						
$\dot{M}_{LBE}$ [kg/s]	$\dot{M}_{Ar}$ [kg/s]	α 5	α 6	α 7	α 8	α 9
101,1	8,84E-04	0,022	0,016	0,011	0,004	0,002
123,4	1,94E-03	0,037	0,027	0,019	0,008	0,004
118,6	1,82E-03	0,032	0,024	0,017	0,008	0,003
161,4	3,60E-03	0,067	0,052	0,035	0,019	0,007
161,7	3,77E-03	0,067	0,053	0,036	0,021	0,008
182,9	5,24E-03	0,087	0,072	0,045	0,029	0,011
178,5	5,26E-03	0,082	0,070	0,044	0,029	0,011
205,8	7,50E-03	0,112	0,095	0,061	0,043	0,017
215,1	9,20E-03	0,122	0,104	0,069	0,049	0,019
209,5	8,32E-03	0,115	0,098	0,066	0,046	0,018
224,2	1,05E-02	0,132	0,114	0,077	0,054	0,019
227,9	1,13E-02	0,137	0,117	0,079	0,057	0,019
87,5	9,11E-04	0,015	0,011	0,008	0,002	0,001
115,5	1,72E-03	0,031	0,023	0,016	0,007	0,003
118,8	1,81E-03	0,034	0,024	0,017	0,007	0,003
161,4	3,62E-03	0,066	0,053	0,034	0,020	0,008
158,6	3,59E-03	0,065	0,051	0,034	0,019	0,008
181,9	5,36E-03	0,086	0,072	0,045	0,029	0,012
181,4	5,40E-03	0,084	0,073	0,046	0,029	0,012
207,2	7,54E-03	0,112	0,096	0,063	0,043	0,018
210,0	8,25E-03	0,116	0,099	0,065	0,046	0,018
231,6	1,21E-02	0,142	0,121	0,082	0,061	0,019

Table 15– Values of the void fraction estimated in the five branches of the riser for tests performed at 320°C.

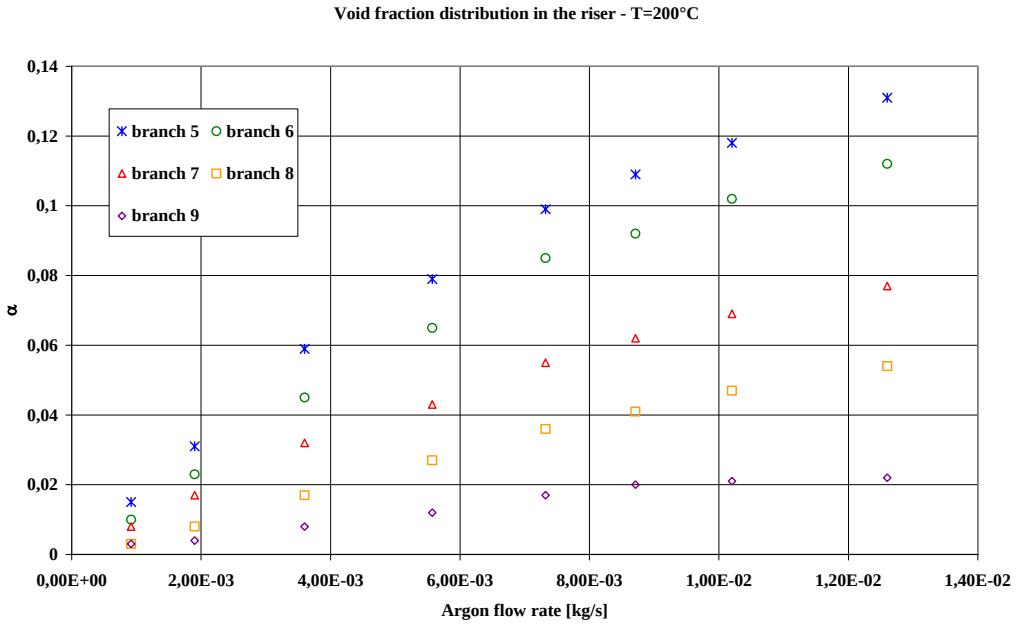

Figure 2-19– Void fraction distribution along the riser for the tests performed at 200 °C. A strong dependence from depth is evident

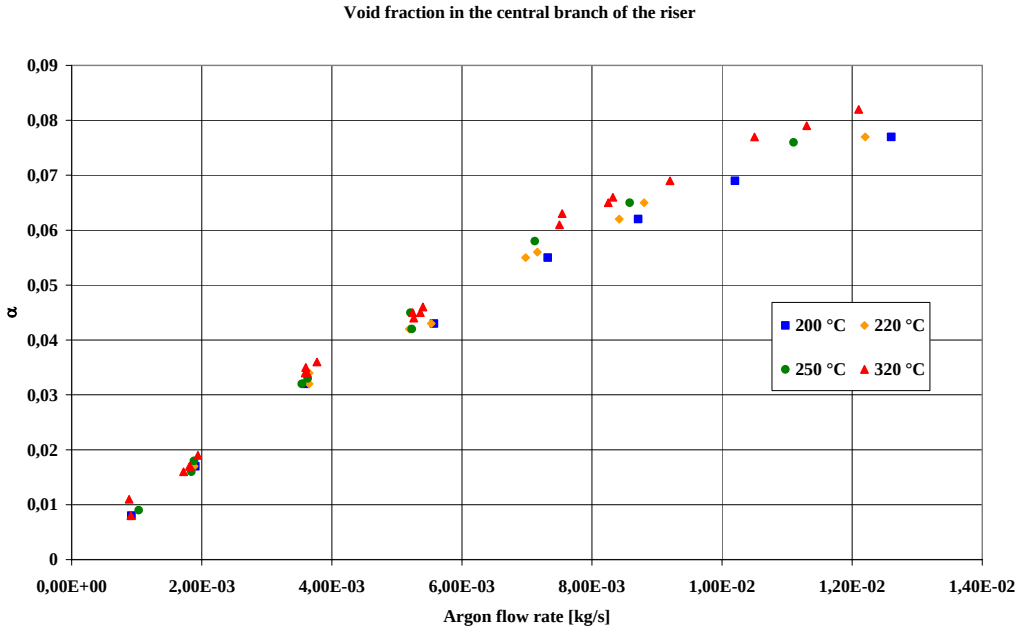

Figure 2-20– Void fraction in the branch 7 of the riser, for all the investigated temperature. A very weak dependence from temperature can be noted.

Conclusion

The possibility to enhance the LBE circulation by gas injection has been confirmed in the CIRCE facility, that is representative of the reference ADS plant.
The results obtained show that for Ar flow rates higher than 1 Nl/s is possible to entrain a steady flow of LBE trough the test section adopted. A relation between the entrained liquid metal flow rate and the injected one has been carried out by best fit of experimental data.
This relation follows a power law and a theoretical justification of the result has been carried out too.
Comparing the results of the experiment with the pre test analysis performed by means of the Relap5/mod 3.2.2 Beta code in the version developed by Ansaldo, a satisfactory agreement between the data have been verified, even if the code slightly underestimates the experimental results, at least in the investigated range of flow rates.
The second experimental campaign on the gas enhanced circulation has been successfully accomplished on the CIRCE facility. All the results obtained during the first campaign, in particular the possibility to establish a steady liquid metal flow rate higher than 200 kg/s, have been confirmed. However, at gas flow rate lower than 1Nl/s, the occurrence of instability phenomena has been confirmed too.
The role of temperature has been investigated: as already found, the two flow rates are related by a power low, but the liquid flow rate is slightly dependent from the temperature, so a curve not dependent from temperature has been considered to describe the liquid flow rate as function of the gas one only.
Differential pressure measurement allowed to obtain data on the localised loss of pressure as well as the distributed one. In particular, the results indicate that the loss coefficient related to a calibrated orifice located in the single phase region to simulate the loss of head of the reference core is not constant and depends from the liquid flow rate.

The loss of pressure measurements performed along the riser allowed to say that the pressure drop in the two phase region is essentially due to the gravimetric head, being the acceleration term negligible. Moreover, these measurement allowed to estimate the void fraction in the riser.

Bibliography

[1] Report ANSALDO CIRCE1SREX004, Rev.2, "TEST SPECIFICATIONS – Enhanced Circulation test" (in Italian)

[2] Report ANSALDO CIRCE5DMMX051010, Rev.1 (in Italian)

[3] Rapporto ANSALDO CIRCE 1 TRLX 0013, "Nota di calcolo: Pre-test prova di circolazione assistita", 10 luglio 2000.

[4] Report Ansaldo TRASCO 11 TNLX C016, "*Dimensionamento degli orifizi che simulano le perdite di carico nelle prove di circolazione assistita in CIRCE*", October 2003 (*in Italian*);

[5] R. W. Lockart, R. C. Martinelli, "*Proposed correlation of data for isothermal two-phase two-component flow in pipes*", Chem. Eng. Prog. 45:no. 39, 1949;

[6] N. E. Todreas, M. S. Kazimi, "*Nuclear System I, Thermal Hydraulic Fundamentals*" Taylor&Francis, New York, 1989;

[7] W. Ambrosiani, G. Benamati, S. Carnevali, C. Foletti, N. Forgione, F. Oriolo, G. Scaddozzo, M.tarantino – *"Experiments on gas injection enhanced circulation in a pool-type liquid metal apparatus"* – XXIV Congresso Nazionale UIT sulla Trasmissione del Calore, - Napoli 21-23 Giugno 2006

3. Lift-pump qualification

Abstract

The results obtained by the two experimental campaigns performed on CIRCE have been used to characterise the lift-pump.
Several two phase models use the volumetric fluxes (or superficial velocities); therefore, the results already described in the previous chapters have been described in terms of these quantities. In this way, for example, has been possible to try an indirect determination of the flow regime that interested the experiments, making use of the flow maps available in literature (in fact, many of these make use of the volumetric fluxes as coordinates).
Moreover, the analysis performed shows that the temperature is not an important parameter in the description of the system behaviour. For this reason the most important variables that characterise the flow have been correlated paying few attention to the temperature, looking for temperature independent best fit curves.
Finally, a first analysis on the performance of this pumping technique has been carried out too. The results point out as the lift-pump is characterised by an efficiency with a quite parabolic trend, with the highest values in correspondence to a well defined range of gas flow rate.

Characteristic circulation curves

As explained in the previous chapters, the most important objectives that aimed the two experimental campaigns performed on CIRCE were to demonstrate the feasibility of the lift-pump technique applied to the pool configuration and to collect data useful to its characterization.
Since the system the system shows a very slight dependence from the temperature, at least in the investigated range. This behaviour suggests to look for best fit curve of the experimental data that allow to predict the liquid flow rate ignoring the temperature of the system.
In Figure 3-1 the flow rate data are reported with the curve carried out using a minimum square best fit technique; the best fit equation is:

$$\dot{M}_{LBE_{bestfit}} = 93{,}191 \cdot \dot{M}_{Ar}^{\,0{,}3748} \qquad \mathbf{1}$$

where the argon flow rate is expressed in g/s
The standard uncertainty relevant to the use of equation (1), is ±7%. In Figure 3-2 the percentage residue relevant to the use of equation (1) is displayed: the points represent the relative distance between the flow rate measured and the prediction obtained by equation (1). As can be noted, quite all the data are comprise in a 10% band.

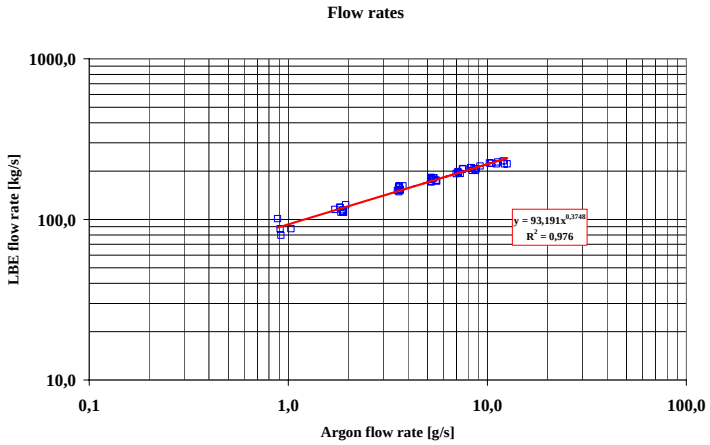

Figure 3-1– Liquid metal flow rate as function of the injected gas flow rate.

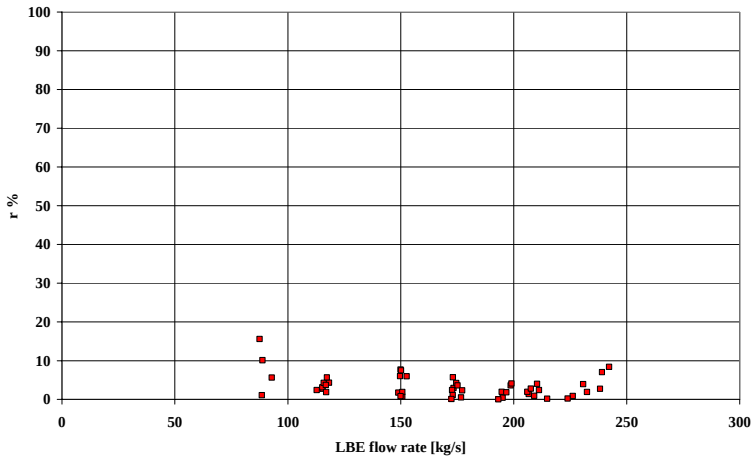

Figure 3-2– Percentage residual related to the use of equation 6.1; the points represent the distance between the experimental data and the values predicted by equation 6.1

Volumetric fluxes

To characterise the gas the system it can be useful to introduce the following quantity:

$$j_g = \frac{\dot{Q}_g}{A_{ris}} \qquad \text{volumetric flux of the gas phase;} \qquad (2)$$

$$j_l = \frac{\dot{Q}_l}{A_{ris}} \qquad \text{volumetric flux of the liquid phase.} \qquad (3)$$

where $\dot{Q}_g$ and $\dot{Q}_l$ are the volumetric flow rates of the two phases. These quantities are also called superficial velocities by many authors [1][2] Here in the following both the names will be used indifferently.

In Figure 3-3 the volumetric fluxes obtained during the experiments are displayed. As already seen in the case of the flow rates, the two quantities follow a power law progression and the dependence from temperature is very weak.

Another parameter that can be useful to describe the behaviour of the two phase system is the mixture superficial velocity, defined as:

$$J = j_g + j_l \qquad (4)$$

In Figure 3-4 j_g is displayed as function of J, while in figure 6.5 the ratio $\frac{j_g}{J}$, that represents the volumetric title of the mixture, is reported as function of J. As can be seen by Figure 3-4 the data seem to follow once again a power law. The best fit equation is close to be parabolic, but the exponent is some more than 2; the curve can be in fact expressed as:

$$j_g = J(aJ^{1.3}) \qquad (5)$$

where a = 1.87 $(s/m)^{-1.3}$

As result, the volumetric title follows a more than linear progression with the mixture superficial velocity, as shown in Figure 3-5

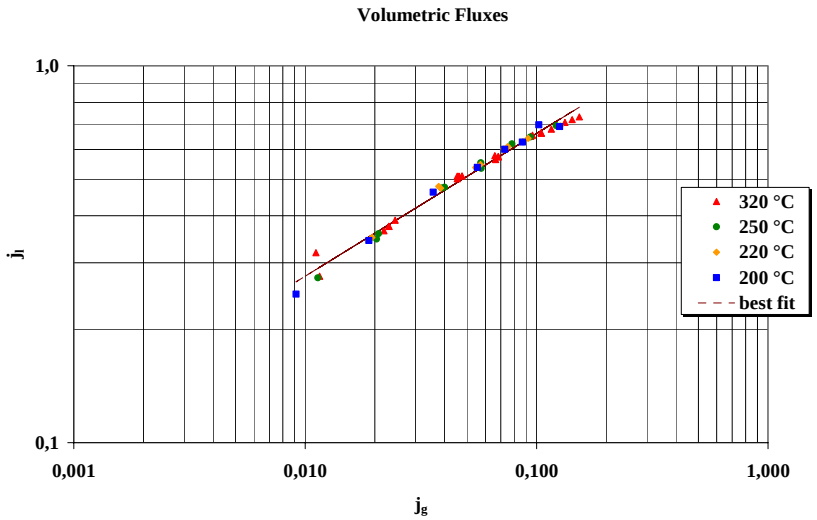

Figure 3-3 – Volumetric flux of the liquid phase as function of the gas injected. As expected, the temperature plays a negligible role. The data are best-fitted by the following temperature independent equation: $j_l = 1.5819\, j_g^{\,0.3787}$. The correlation factor for the least square best fit is $R^2 = 0.986$.

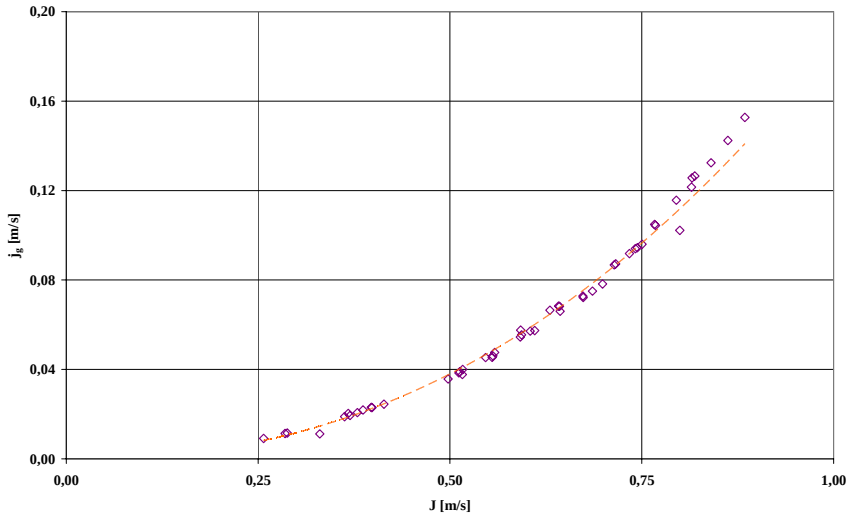

Figure 3-4 – j_g as function of the mixture superficial velocity

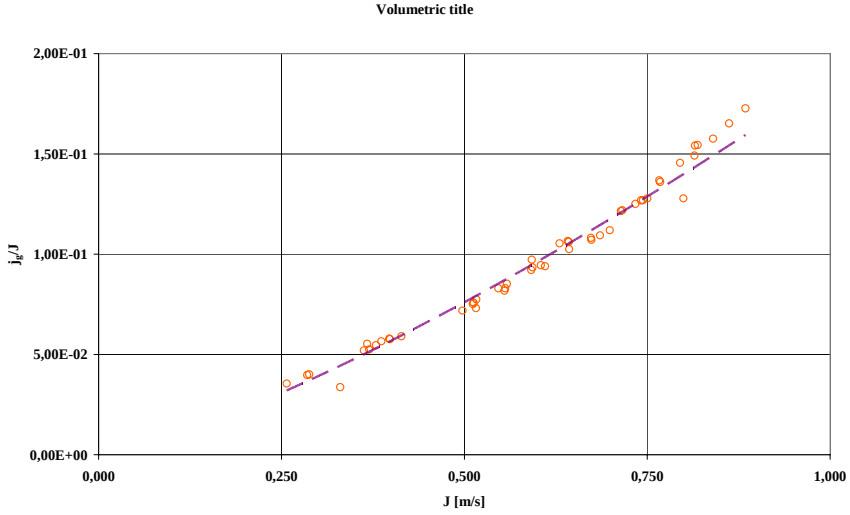

Figure 3-5 – Volumetric title of the mixture as function of the mixture superficial velocity; the data are best-fitted by a power law: $\frac{j_g}{J} = 0.187 J^{1.3}$; the correlation factor is 0.979.

Flow quality

Let's now to consider the flow quality of the two phase mixture:

$$x = \frac{\dot{M}_g}{\dot{M}_l + \dot{M}_g} \qquad (6)$$

Note that for the system under investigation is $x = \frac{\dot{M}_{Ar}}{\dot{M}_{LBE}}$.

The flow quality increases as the gas flow rate increases, while shows a slight decrement when the temperature increases. This because the liquid flow rate is slightly dependent from temperature, as already discussed in the previous chapter. Nevertheless, also in this case a temperature independent relation able to give good predictions for the flow quality can be obtained:

$$x = 1.643 \cdot 10^{-6} \, j_g^{\,0.645} \qquad (7)$$

The best-fit equation as well as the experimental data are shown in Figure 3-6.

If equation (1) is used to estimate the liquid flow rate, known a range of gas flow rate to be injected, the flow quality can be directly calculated by the definition (6).

The result of this calculation has been reported in Figure 3-7together with the experimental data and equation 7. As can be noted, the so evaluated curve slightly overestimate the data, but it is still in agreement with the experimental results.

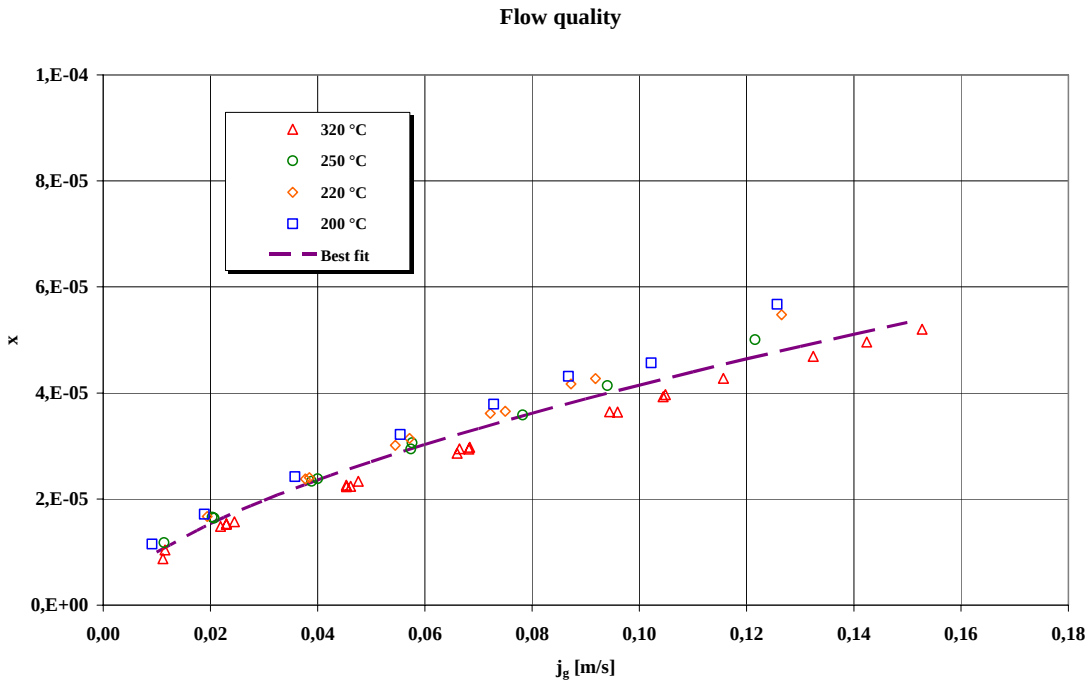

Figure 3-6 – Flow quality as function of the superficial velocity of the gas phase.

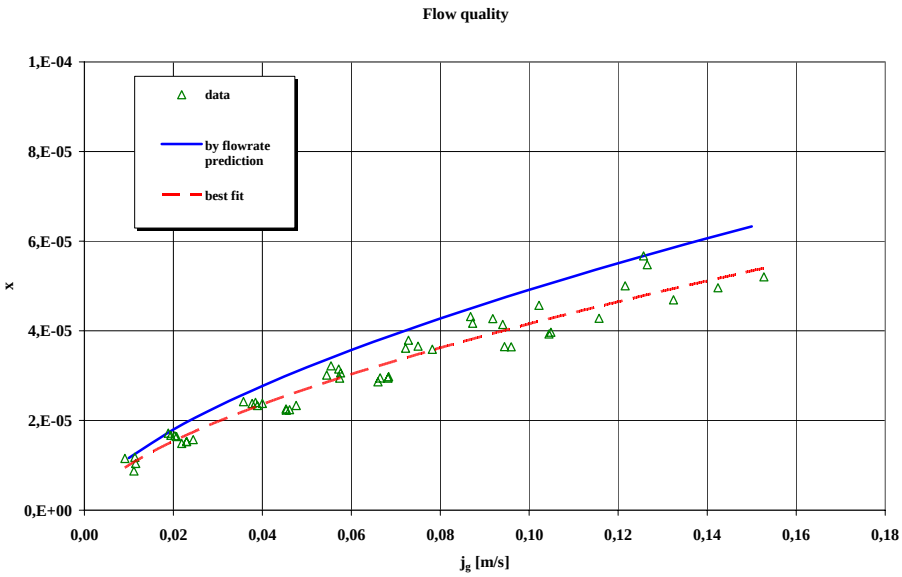

Figure 3-7– Comparison between the best fit curve and the flow quality calculated using equation 6.1 to predict the liquid flow rate.

Void fraction

As already discussed in the previous chapter, the void fraction has been estimated by differential pressure measurements along the two phase region. To each one of the five branches that form the riser it is possible to estimate the corresponding void fraction, starting from the differential pressure measurements. In Figure 3-8 the void fraction evaluated for different branches of the riser is displayed as function of the gas volumetric flux. Except in the case of the first branch, the trend of the data is practically the same in each part of the riser. As can be noted, the data relevant to the first branch suffer of a high dispersion, and suggest a saturation at high values of j_g .This behaviour is probably related to the proximity of the injector.

Also in the case of the void fraction it is possible to note a weak dependence from the temperature. On the contrary, the position in the riser play a more important role. In Figure 3-9 the void fraction along the riser is depicted for two gas flow rate: 1 Nl/s and 7 Nl/s. A clear influence of the axial position can be noted. In fact, due to the gradient of pressure that exists in the riser, the gas phase undergoes to an important expansion while it rises toward the two phase region, approaching the free level of the liquid metal. The trend can be assumed linear with the z coordinate, whose origin has been placed on the injection point.

It can be useful to consider an average void fraction $\bar{\alpha}$ able to describe the behaviour of the system. This can be assumed as the void fraction relevant to the central part of the two phase region. According to the linear trend shown in Figure 3-9, for each steady state the average void fraction has been calculated as the linear interpolation of the data.

In Figure 3-10 $\bar{\alpha}$ has been displayed as function of the gas volumetric flux, while in Figure 3-11 it has been represented as function of the flow quality. Concerning the dependence from j_g , the data follow a parabolic progression. The relation between $\bar{\alpha}$ and the flow quality can be instead considered as linear.

Finally, $\bar{\alpha}$ has been compared with the void fraction waited in the case of homogeneous and annular flow. To calculate the void fraction in these two case the following relation has been adopted:

$$\alpha = \frac{1}{1 + S\left(\frac{\rho_g}{\rho_l}\right)\left(\frac{1-x}{x}\right)} \tag{8}$$

where the slip ratio S is equal to 1 in the case of homogeneous flow, while it has been assumed equal to 35 in the case of annular flow.

The results obtained are displayed in Figure 3-12. As shown in the picture, $\bar{\alpha}$ is comprises between the two other cases. This confirms that the use of a separate flow model is an appropriate choice.

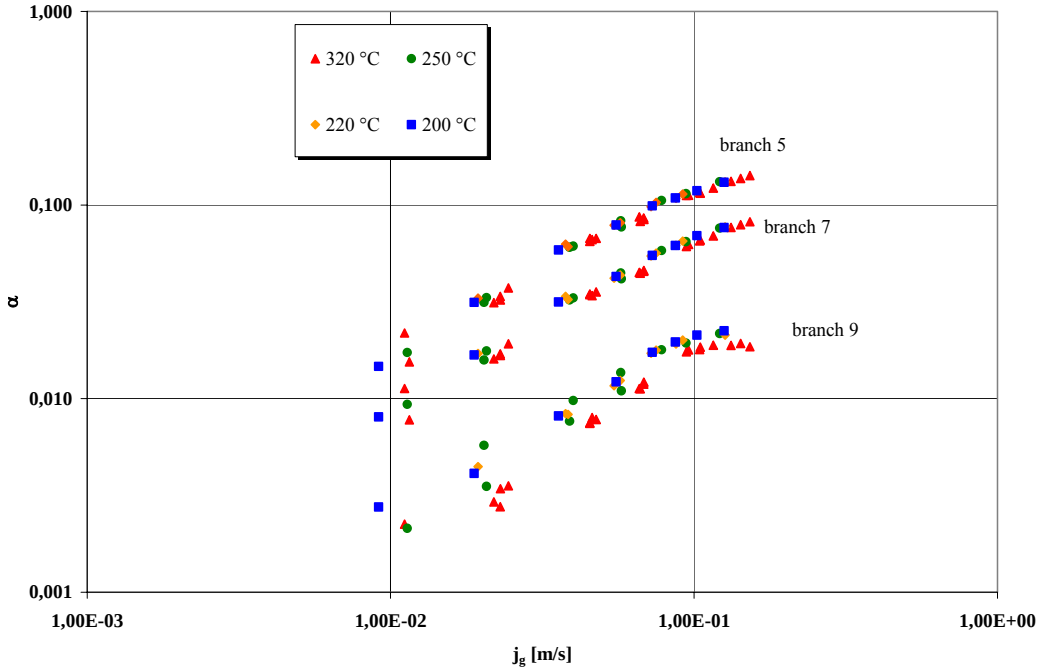

Figure 3-8– Void fraction estimated in different branches of the riser at different temperatures; also in this case the temperature doesn't play an important role.

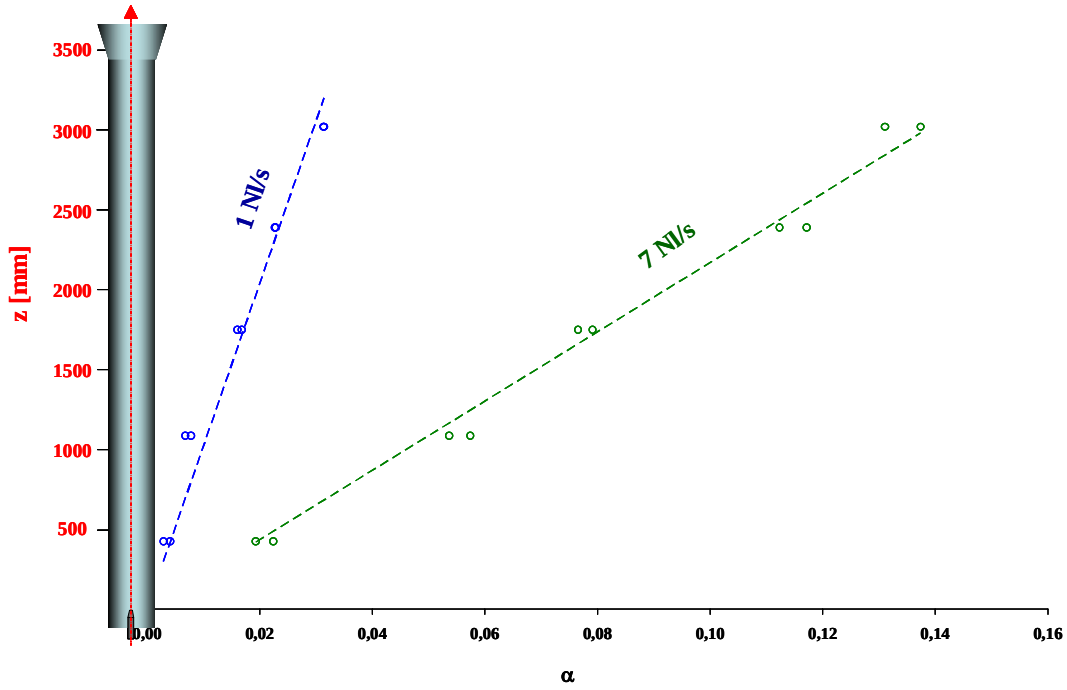

Figure 3-9– Void fraction along the riser. The dependence from the position can be assumed as linear

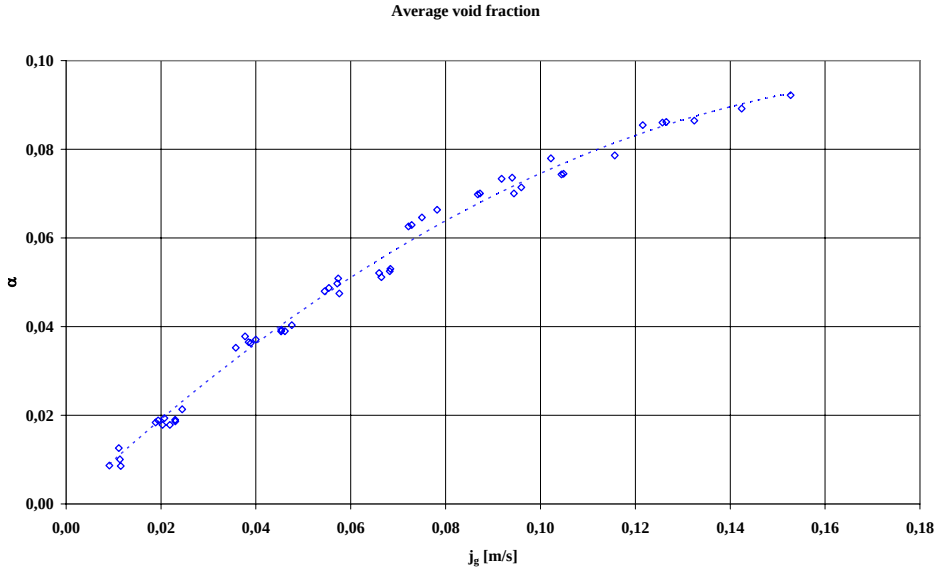

Figure 3-10 – Average void fraction in the two phase region; the data follow a parabolic progression.

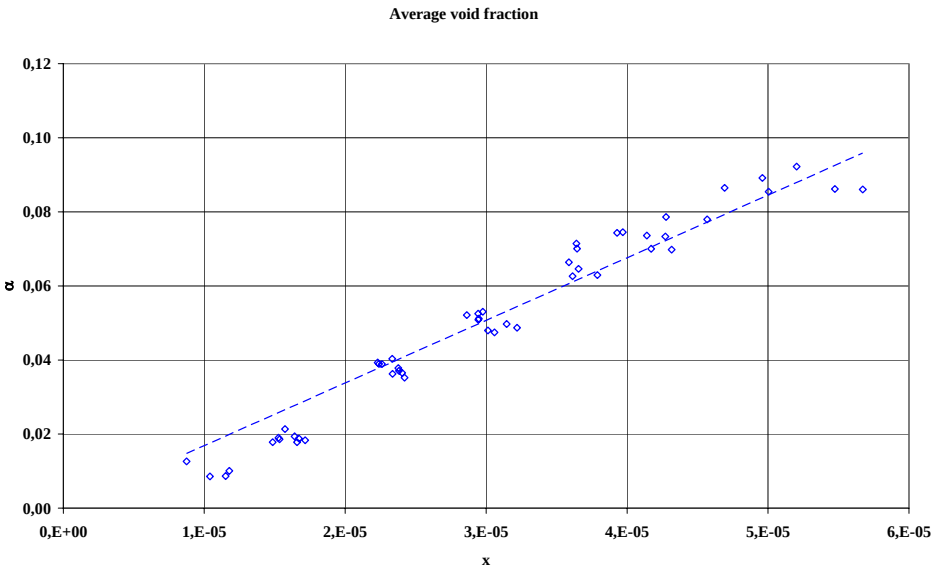

Figure 3-11 – Average void fraction as function of the flow quality; the trend can be assumed as linear.

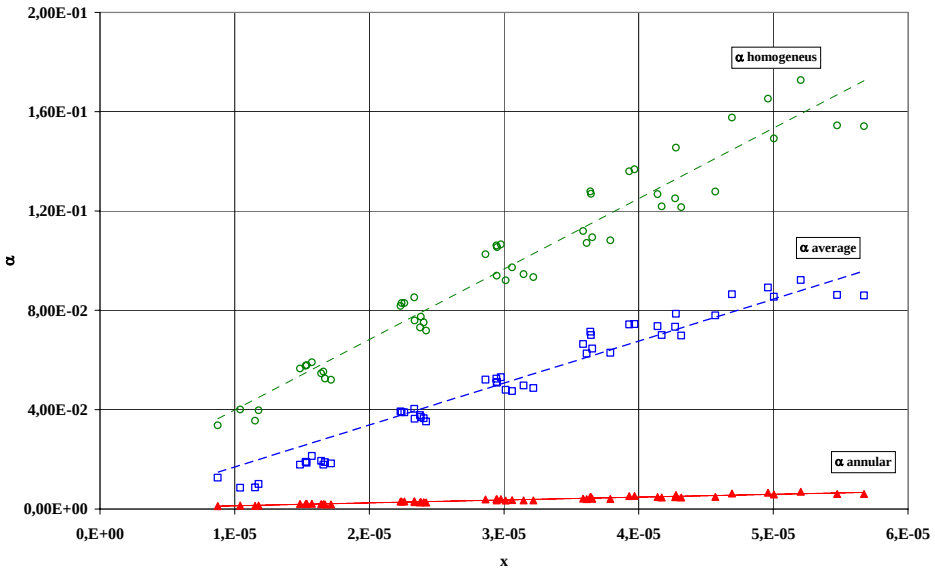

Figure 3-12 – Comparison between the average void fraction and the void fraction in the case of homogeneous and annular flow.

Slip fraction

Using equation (8) it is possible to evaluate the slip ratio in the different parts of the riser, known the void fraction. The result is reported in Figure 3-13. The slip ratio shows its highest values at low superficial velocity of the gas phase, decreasing very quickly as the j_g increases.

At superficial velocities of the gas phase higher than 0.05 m/s, the slip ratio became practically constant and the influence of the axial coordinate seems to be less important than at lower values of j_g. In fact, except in the case of the first branch of the riser, S is comprises in the range between 2 and 4.

Concerning the first branch, it is characterised by higher values of S even if the general trend can be assumed the same found in the other branches. These result is probably related to the proximity of the injector and suggests the presence of a disturbance effect in the region close to the injector.

These results confirm that doesn't exist a mechanical equilibrium between the phases, so the choice to use the separate flow model results in a good hypothesis to characterize the two phase flow in the riser during the performed tests.

Finally, since $\bar{\alpha}$ is used in equation (8), a corresponding $\bar{S}$ can be evaluated. In Figure 3-14 $\bar{S}$ has been displayed and compared to the slip ratio obtained using the Chisolm correlation [2]. According to this the slip ratio is given by:

$$S = \left[1 + x\left(\frac{\rho_l}{\rho_g} - 1\right)\right]^{-0.5} \qquad (9)$$

As can be noted, the Chisolm correlation underestimate the experimental data. Moreover, the trend found at values of j_g lower than 0.05 m/s is completely ignored by relation (9).

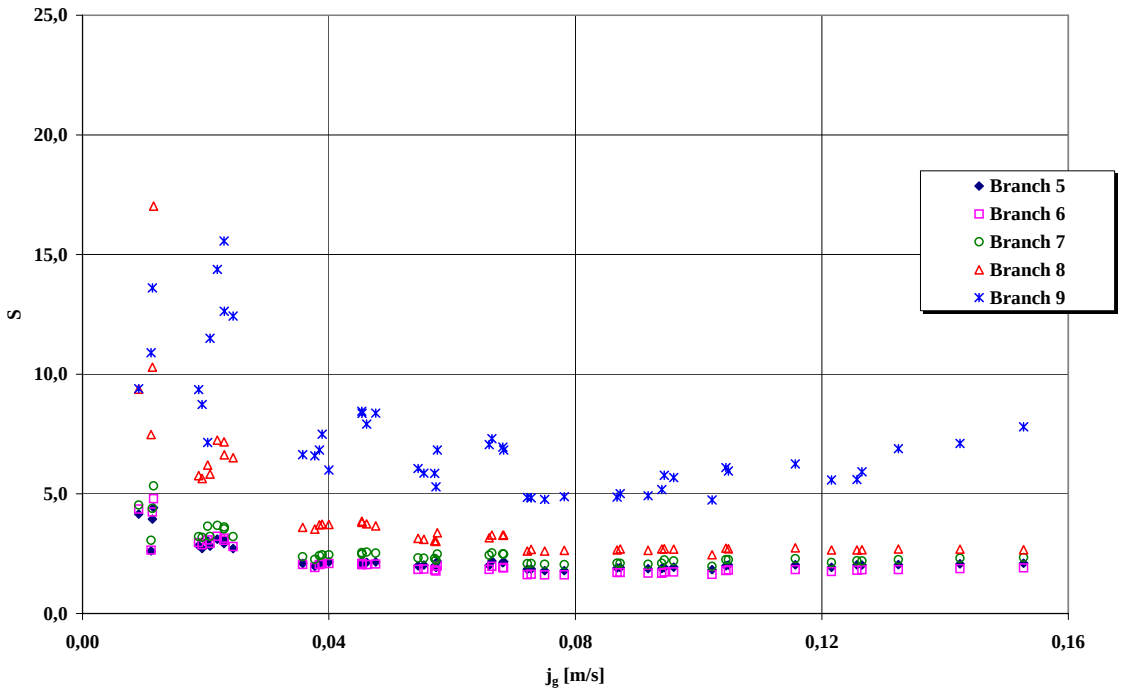

Figure 3-13 – Slip ratio in the different branches of the riser as function of the gas volumetric flux.

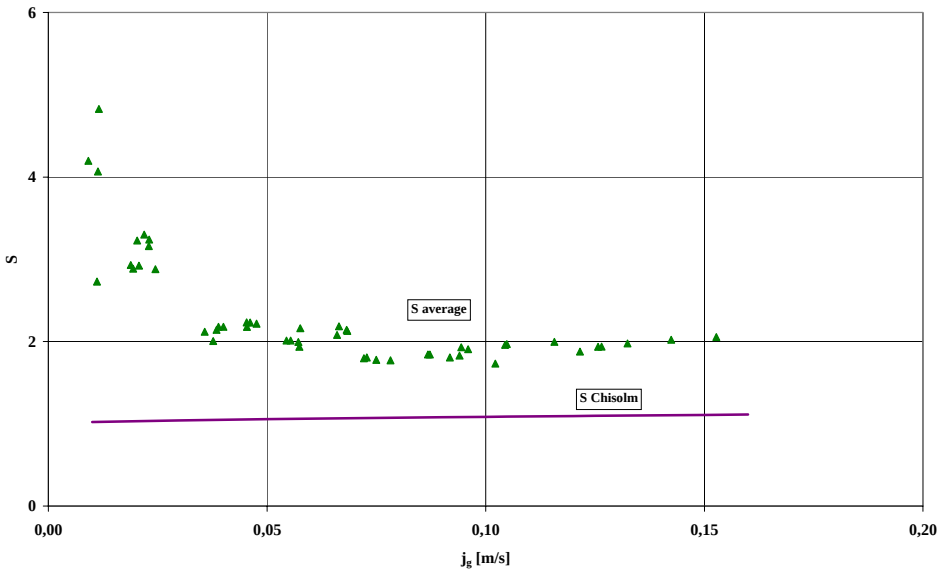

Figure 3-14 – Comparison between $\overline{S}$ and the slip ratio given by the Chisolm correlation.

Flow patern

For the determination of the flow regime in the two phase region only an indirect analysis has been performed, based on the flow maps available in literature. In fact, the plant is not supplied by the instrumentation able to recognise the two phase structures that take place during the tests. Among the possible choice for vertical flow, trhee maps proposed by different authors have been considered:

- the map proposed by Hewitt and Roberts for vertical flow;
- the map proposed by Ohnuky and Akimoto;
- the map proposed by Taitle, Dukler and Barnea.

The Hewitt and Roberts map is usually used for air-water or steam-water systems. Unfortunately, it is not useful in the case of the experiments under discussion, because the experimental data are out of the range covered by the map (left low corner of the map); moreover, it has been carried out for vertical flow in small diameter pipes (31.2mm) and this condition is not respected in the case of CIRCE.

Ohnuky and Akimoto [4] studied the air-water system in vertical flow and with different pipe diameter sizes. Here we refers to the results that they obtained with a ratio $\frac{L}{D}=10$, that is the closest to the experimental configuration adopted in CIRCE, where the ratio is ~17. In Figure 3-10 the transition curves deduced by the work of Ohnuky and Akimoto are reported together with the experimental results obtained during the tests. According to the picture, the flow regime should be a bubbly flow and only at the highest gas superficial velocities a transition towards a churn-bubbly could occur.

Figure 3-11 reproduces the map proposed by Taitle, Dukler and Barnea [5]; once again the experimental data have been reported on the map and also in this case a bubbly flow is predicted as flow pattern.

The bubbly flow regime seems to be compatible also with the low void fraction that characterises the system. In fact, the transition from bubbly to slug flow usually occurs when the void fraction reach the value of 0.3 [2].

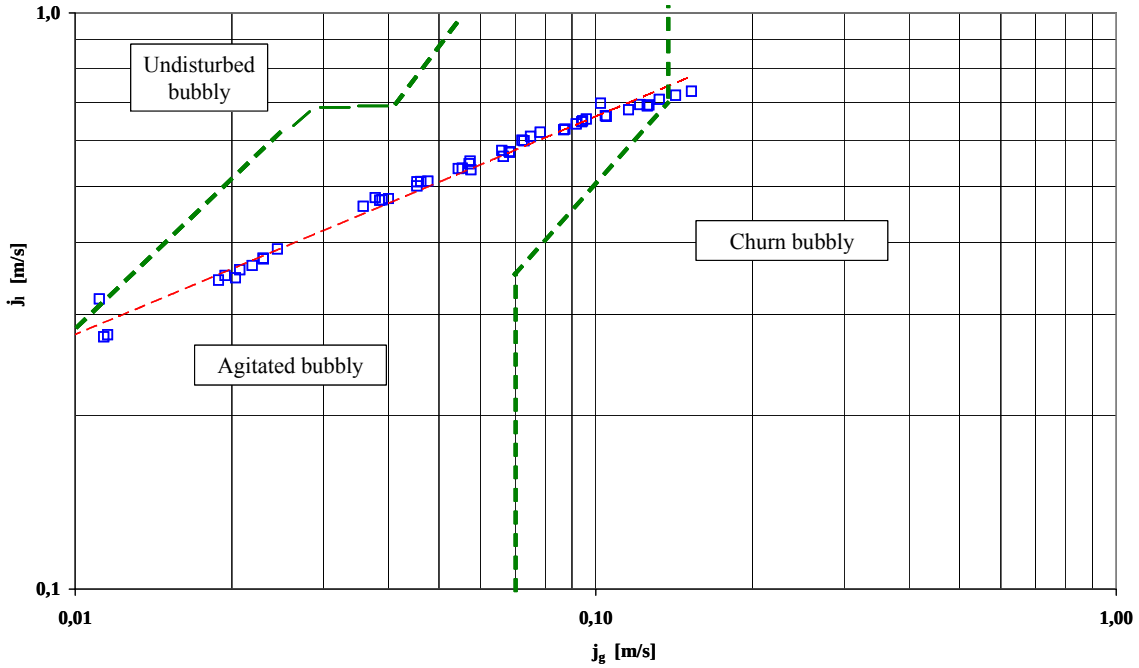

Figure 3-15– Transition curves deduced from the work by Ohnuki and Akimoto. According to the picture the flow regime in the performed experiments is a bubbly flow

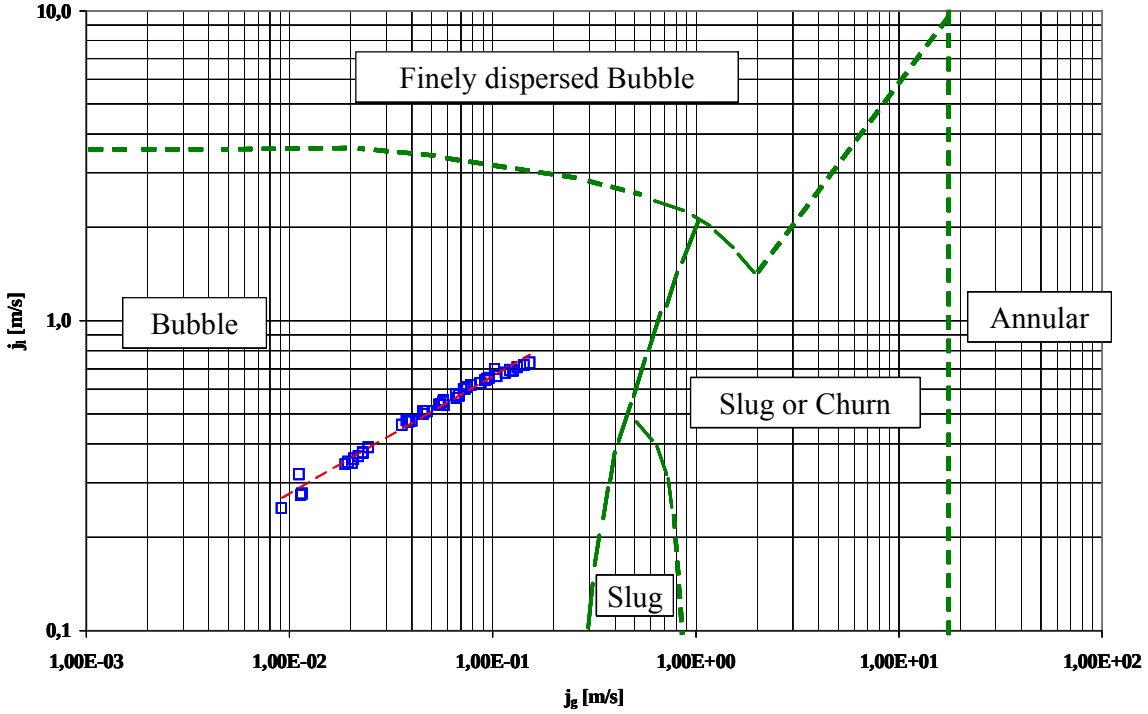

Figure 3-16– Taitle, Dukler and Barnea map for vertical flow. Also this flow map predicts a bubbly flow for the experiments performed in CIRCE .

Lift-pump performances

The data collected can be used to carry out a first analysis on the performances of the lift pump. To carry out this analysis, it is important to know the curves that characterise the system, such as the flow rate characteristic as well as the driving force that allow the circulation of the liquid phase, or equivalently the resistant characteristic curve of the system. For simplicity, the analysis has been based on the use of the average void fraction as defined in the previous sections.
Moreover, as already seen in the previous parts, the effect of the temperature on the global behaviour of the system is weak enough to suggest the use of temperature independent curves. For this reason, only few graphics reported in the following parts are depicted taking in account the test temperature, while the most report the experimental data with no reference to the test temperature. In these cases, the physical properties have been evaluated at 260 °C, when required, that is the average temperature in the considered range.

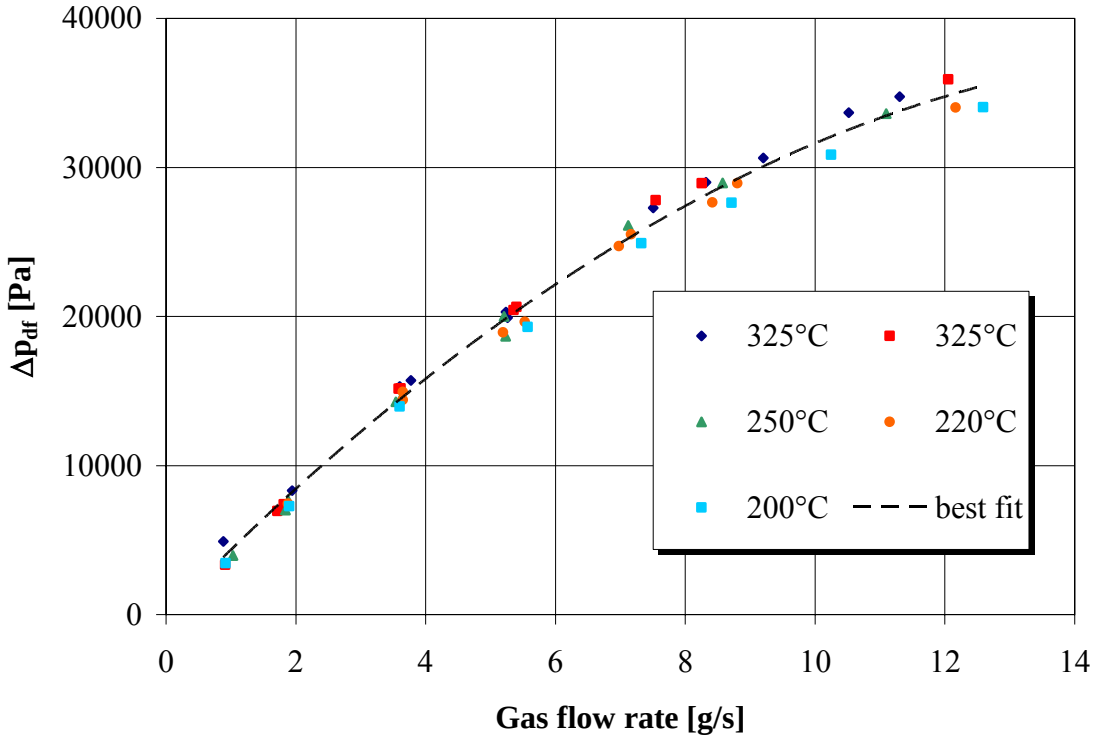

Figure 3-17- Driving force gas injection flow rate and the average temperature of the system. The data are best fitted by the equation $\Delta p_{df} = -132.39\dot{M}_{gas}^2 + 4485.5\dot{M}_{gas}$, where the gas flow rate is in g/s and the driving force is obtained in Pa. The correlation factor is R^2 =0.99

Pumping Power

One of the performance parameters that can be considered is the pumping power relevant to the lift-pump. It is intended as the minimum power required to allow the liquid metal circulation. This is related to the flow of the liquid phase only and can be expressed as the product of the LBE volumetric flow rate and the circulation promoter, as follow:

$$P_p = \Delta p_{DF} \frac{\dot{M}_{LBE}}{\rho_{LBE}} \qquad (10)$$

Note that this expression is formally analogous to the one usually used in the case of uncompressible fluids. This relation point out as both the flow rate characteristic curve and the promoter term are required to estimate the pumping power. Alternatively, because of under steady state conditions the circulation promoter is equal to the total loss of pressure along the path, the system resistant characteristic can be used in eq. (10).

The driving force that allow to enhance the circulation of the liquid metal can be estimated on the base of $\bar{\alpha}$ and of the average gas density in the riser, using the following expression:

$$\Delta p_{DF} = (\rho_l - \bar{\rho}_m) g H_{ris} = \bar{\alpha}_{ris} g H_{ris} (\rho_l - \bar{\rho}_g) \quad (11)$$

As shown in Figure 3-17 the driving force increases as the gas flow rate increases, following a parabolic progression.

Under steady state conditions, the driving force is equal to the total pressure drop along the path; so, displaying the same quantity as function of the liquid flow rate we obtain the resistant characteristic of the system (Figure 3-18). As expected, it is increasing with the LBE flow rate and the effect of the temperature is negligible. Also in this case the data follow a parabolic progression and it is possible to look for a temperature independent best fit equation.

Finally, it is possible to estimate the pumping power. The result is displayed in Figure 3-19. The data follow a progression close to a cubic law. In **Errore. L'origine riferimento non è stata trovata.**the pumping power has been instead displayed as function of the injected gas flow rate; its dependence from the gas flow rate is quite linear. This results confirm what was already noted in the case of air-water systems [6][7].

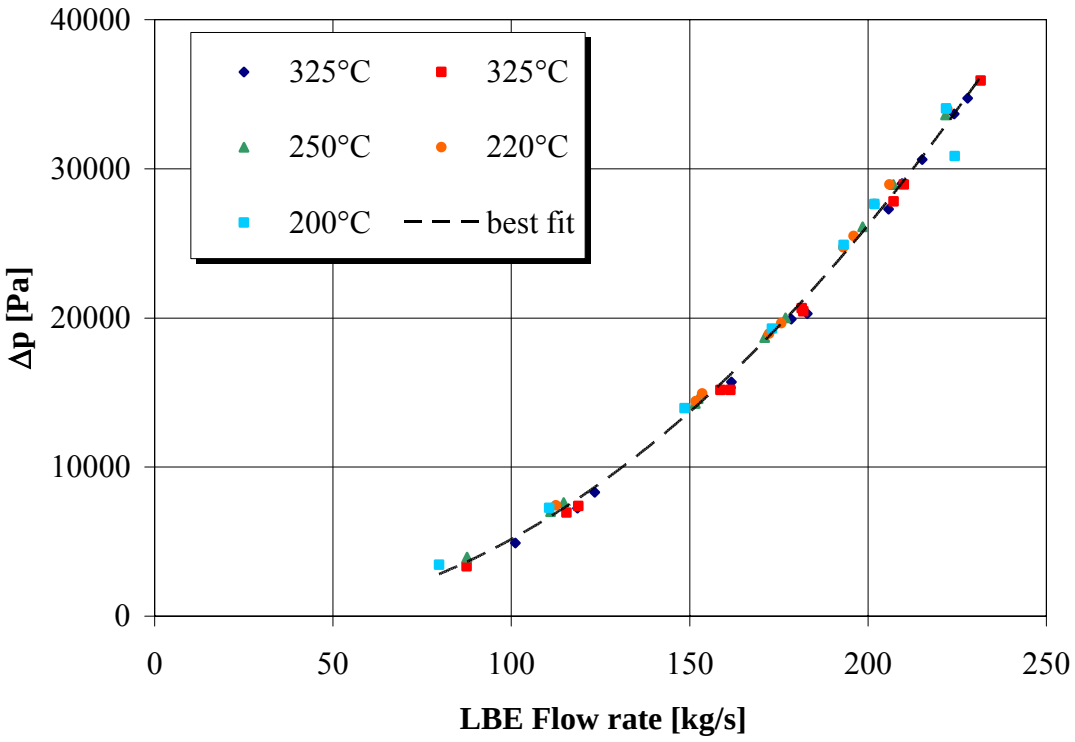

Figure 3-18- Resistant characteristic of the system The data follow a parabolic progression.

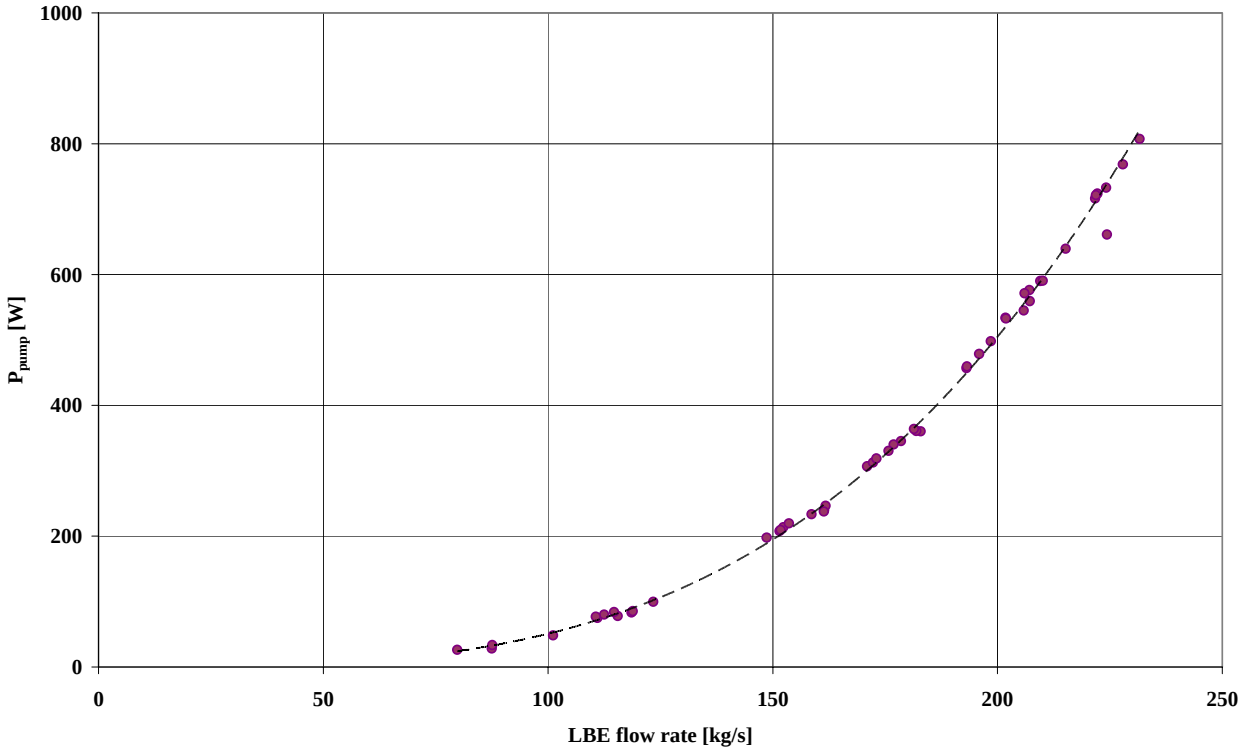

Figure 3-19– Pumping power as function of the LBE flow rate. The data follow a quite cubic progression.

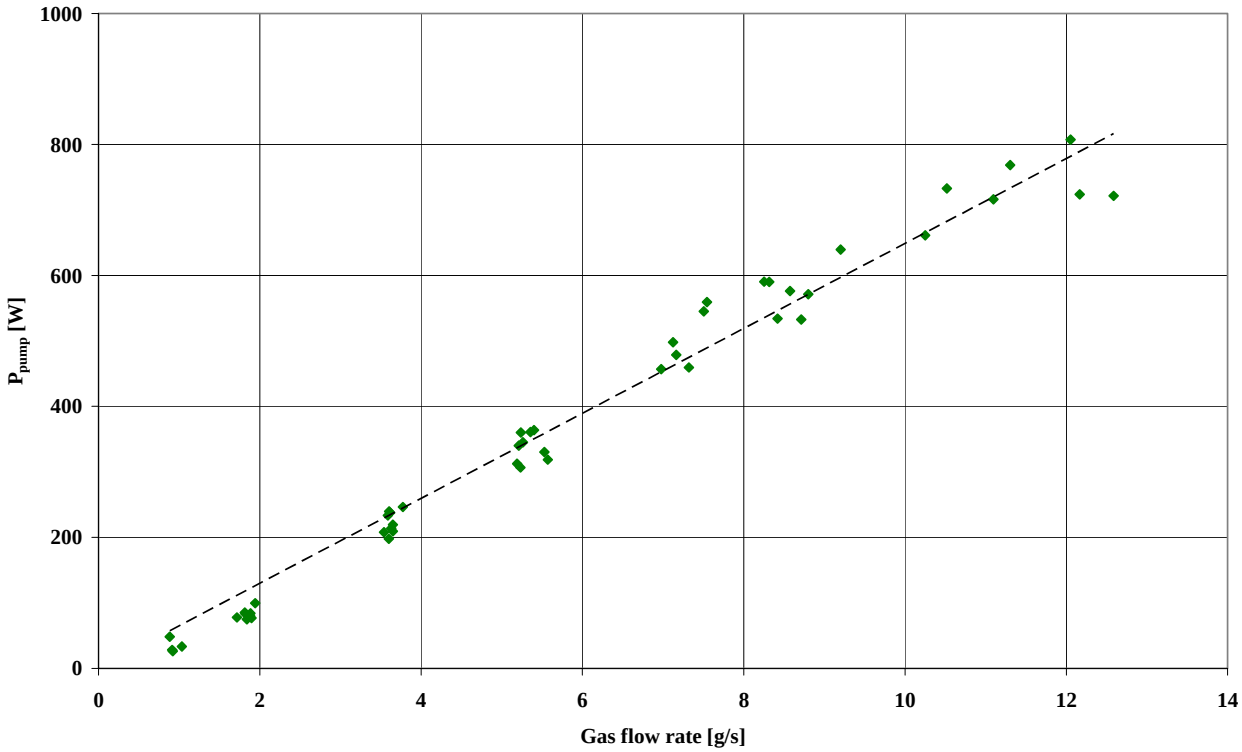

Figure 3-20 – Pumping power as function of the gas flow rate. The trend can be considered as linear.

Efficiency

Another interesting performance parameter that can characterise the lift pump is its efficiency. As first approximation, it is possible to define an ideal efficiency for the lift-pump, as the ratio between the pumping and compression power:

$$\eta = \frac{P_{pump}}{P_{comp}} \tag{12}$$

The compression power is the power required to pressurise the gas; the gas is injected at the bottom of the riser with a pressure of about 5 bar, then it flow upward decreasing its pressure and reach the cover gas, where the pressure is about 1.1 bar. From the cover gas, it is kept by the ARS and pressurised once again by means of the positive displacement blowers. The system can be considered closed.
Under the hypothesis of an adiabatic isentropic compression, the specific work required to pressurize the gas can be calculated as:

$$l_{ad} = \frac{k}{k-1} R^* T_{cg} \left[\beta^{\frac{k-1}{k}} - 1 \right] \tag{13}$$

where:

- $k = \frac{c_p}{c_v} = 1.67$;
- R^* is the argon constant, its value equal to $208.21 \ \frac{\text{J}}{\text{kg K}}$;
- T_{cg} is the cover gas temperature;
- $\beta = \frac{p_{inj}}{p_{cg}}$ is the compression ratio, with P_{cg} and P_{inj} the pressure in the cover gas and in the injection point respectively.

The power required to pressurise the gas can be then calculated by the following equation:

$$P_{comp} = \dot{M}_g l_{ad} \tag{14}$$

Figure 3-21 shows the results given by equation (14), displayed as function of the obtained liquid flow rate; the data follow a trend that is some more than parabolic, being the exponent of the power law that best-fit the data equal to 2.6.

Finally, it is possible to estimate the efficiency of the lift pump. The result is reported in Figure 3-22. As can be noted, the efficiency shows a maximum around a gas flow rate of 8 g/s, corresponding to a liquid flow rate of about 200 kg/s (see i.e. Figure 3-1).
At higher gas flow rates the efficiency decreases. This behaviour seems in agreement with the possible occurrence of a transition in the flow regime at high values of the gas flow rate, as predicted by the Ohnuki and Akimoto flow map (see Figure 3-15).

However, even under the best conditions the efficiency is lower than 0.6. Anyway, it should be noted as the injector used during the test is the worse possible choice from the point of view of the two phase mixing. An improvement of the performance can be expected in the case of more sophisticate devices, such as diffusers or porous media, able to generate and well distribute small sized bubbles. On the other hand, the solution adopted is the simplest device to be used to perform the task.

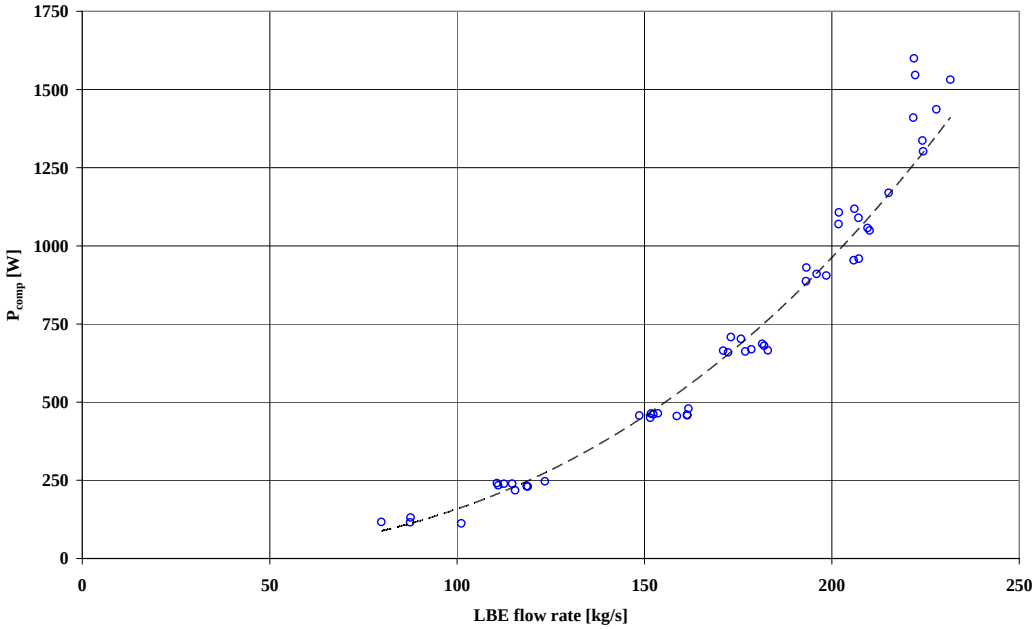

Figure 3-21– Power required to pressurise the injected gas as function of the obtained liquid flow rate. The trend is some more than parabolic.

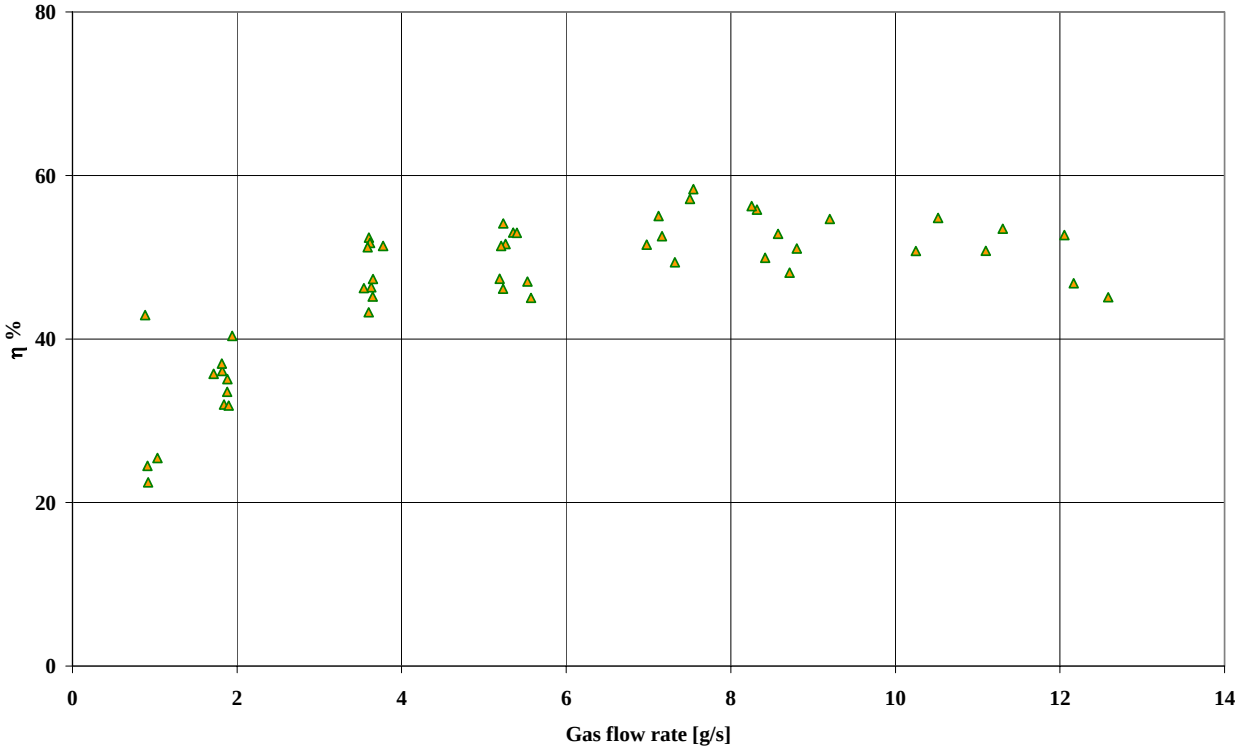

Figure 3-22– Efficiency of the lift pump as function of the gas flow rate. The maximum is obtained around 8 g/s, with a corresponding liquid flow rate of about 200 kg/s.

Conclusions

The analysis performed allowed to characterise the two phase flow that is responsible for the liquid circulation in the system.

The temperature of the liquid metal can be considered as a variable of secondary importance, being its influence on the circulation parameters very weak. For this reason, the characteristic curves obtained by best-fit of the experimental data are temperature independent.

The enhanced circulation has been described in terms of flow rate and volumetric flux curves and relations able to predict the response of the liquid phase to a defined injection of gas have been obtained. Many of the results obtained in previous experiments performed on air-water systems have been confirmed. For example, the evolution of the flow rates follow the same trend related to a power law.

Even if a direct observation of the flow pattern during the tests has not been possible, the results obtained give indirect information that suggest a kind of bubbly flow regime. Moreover, it seems consistent with the results the possibility of a flow pattern transition toward a churn-bubbly flow at gas flow rates higher than 8 g/s.

The information obtained on the void fraction as far as on the slip ratio confirm that the use of a separate flow model to describe the behaviour of the system is a good choice.

Finally, the analysis performed on this pumping technique highlighted the trend of the main important performance parameters, pointing out as the pumping power developed is close to a cubic function of the liquid flow rate and as the efficiency of the lift pump assumes its highest values in correspondence of a well defined range of the gas flow rate.

Bibliography

[1] N. E. Todreas, M. S. Kazimi, "*Nuclear System I, Thermal Hydraulic Fundamentals*" Taylor&Francis, New York, 1989;

[2] P.B.Whalley - Boiling, Condensation, and Gas-Liquid Flow – Clarendon Press, Oxford - 1987

[3] A. Bergles, J. Collier, J. Delhaye, G. Hewitt, F. Mayinger, Two phase flow and heat transfer in the power and process industries, Hemisphere publishing corporation – 1981.

[4] Ohnuki H., Akimoto H., Experimental study on transition of flow pattern and phase distribution in upward air-water two phase flow along a large vertical pipe, Int. J. Multiphase Flow, 26, 376-386, 2000

[5] Y. Taitel, D. Barnea, A. E. Dukler, "*Modelling flow pattern transitions for steady upward gas-liquid flow in vertical tubes*", AIChE J. 26:345, 1980;

[6] B. Panella, Caratterizzazione fluidodinamica della circolazione bifase assistita con iniezioni di gas, IV Scuola Estiva di Termofluidodinamica: Termofluidodinamica Sperimentale e Tecniche di Misura, Certosa di Pontignano – Siena, 2003

[7] M.Desalve, M.Malandrone, B. Panella, Gas driver circulation in a adiabatic air-water loop with reference to accelerator driver systems, ICONE 10 – 22,54,6 – track 7 – April 14-18, Arlington, WA USA, 2002.

4. Lead Bismuth aerosols

Abstract

During the test campaign carried out in the three big facilities operating in Lead Bismuth, a black, fine powder was found in the gas lines.

Since a very low amount of information was available on this phenomena it was decided to start an experimental campaign, together with a literature review, in order to understand the formation mechanism of this powder.

Two different apparatus were design and built and test carried out.

Intoduction

Two mechanisms of heavy metal release into gas steam are identified that could take place at the interface gas/liquid, both in the free surface region and in two phase flow gas/liquid.

These two phenomena can work in parallel and are:

1. Evaporation of Lead-Bismuth
2. Lead-Bismuth oxides particles entrainment in gas.

The outcome from the mix of the two phenomena is the transfer of fine particles from the liquid metal to the gas phase. The gas moving on the free surface of the melt alloy or in it, acts as a caring element. In his way the powder could move from the LBE into the Ar, and subsequently deposit in other part of the plant and damage them to failure.
So, the comprehension whether one of these two is predominant or not, is design relevant.

State of the art

Description of the phenomena

Three big facilities (LECOR, CHEOPE & CIRCE) have been working, since 2001 at the CR ENEA Brasimone, in the frame of the research programmes on ADS development, with Lead Bismuth as working fluid.
In these facilities, in order to maintain a fixed O_2 concentration, le liquid metal is kept under an inert Ar atmosphere.
In such a way it is possible to add or to remove O_2 due to experimental necessities, avoiding the environmental air to enter the facility.

Figure 4-1 – Black dust in the CIRCE gas circuit

Already in the very fist years of test campaigns, a particular kind of fine dust was found in the gas lines and wherever the melt metal is in contact with the cover gas.
This dust, black-grey coloured, is composed by very small particles, characterized by different granulometry (from 50μm to 5μm or even less).
It tents to float in the cover gas until an obstacle or a variation in the gas velocity let it deposit.

This phenomena is very dangerous for the plant components such as valves, compressors, filters and so on. The powder, as a matter of fact, can lead to a decrease of the efficiency of the component even to its failure.
In order to limit this problem some mechanical filters were realized for the gas phase. Moreover in order to understand the mechanism which enhanced the formation of he dust a literary review and some experimental campaigns were performed

Literary review

In the literature a very limited amount of information is available about the gases and aerosols developed at the interface between Lead and its alloy and the cover gas or even the vacuum.
In [2] it is stated that "because of the extremely low vapour pressure of the Lead-Bismuth coolant", the vapour pressure of the LBE "is not very important". It is estimated [1] that only few grams of Lead-Bismuth are transported out of a pool reactor (at 312°C) due to this mechanism over 40 years of operation.
In order to add some data to this statement in 2002 a dedicated device was built in order to measure the amount of LBE leaving the melt due to vaporization in vacuum [3]. The experiment demonstrated that, actually the effect of the vapour pressure is not really relevant for the phenomena.
Taking in account the mass transfer form the free surface, the powder birth process results in formation, transfer and lodging of coolant aerosol particles on the surface of the reactor components, pipelines and measuring instruments of gas system. From tests realized in Russia **Errore. L'origine riferimento non è stata trovata.** it is clear that also pure lead shows this kind of behaviour.

Experimental campaigns

The objective of he two test campaigns set up at the CR ENEA Brasimone, were :

1. To verify the negligible effect of the PbBi vapour pressure on the powder formation mechanism;
2. To quantify the hourly powder production due to O_2 concentration.

In order to achieve these two goals, two different small devices, Powder Investigation Facility (PIF I & PIF II), have been designed and built up.
The first task if verified, demonstrates that the black dust is generated in the metal on its surface, as Lead oxide and stripped form there by the cover gas.
The second goal, if achieved, should allow to establish a quantitative relationship between the total amount of the powder produced and the working time at a known gas flow rate.
This will help to design a suitable filters system both for ENEA plants and for the future ADS systems.

First campaign

The first device

The first experimental device was assembled in order to investigate if the vapour pressure of the "pure" LBE took part to the dust formation mechanism. Another task of the PIF I was to understand whether the temperature and the geometry variations affected someway the deposition of the powder.

Figure 4-2 – The PIF I device

The PIF I is composed by two little tanks (S1 & S2) jointed by a pipe equipped by portlights, which allowed visual inspections.
S1 is used both as a storage tank as a test section.
As a matter of fact, once melt the PbBi ingots and performed the purification of the alloy, it was used to simulate a pool configuration (CIRCE) system.
A gas injector was placed 20cm under the melt free surface so to bubble gas and to perturbate the liquid metal mass.
The gas coming from the feeding Ar bottle is injected in S1, it enters the observation pipe and follows it. At the end of the pipe is set S2 which works as a deposition vessel. As a matter of fact the section of the observation pipe is widely smaller than the S2 one. Such a change of crossing section leads to a decrease in the Ar velocity and consequentially to a variation of the buoyancy forces of the powder.
A mechanical pump keeps the gas moving in through the loop.
Both the observation pipe and the deposition tank are equipped with portlights which allow the investigator to observe whether some dust have been deposit on the pipe surface during the test.
S1, the observation pipe and S2 are hated separately thanks to electrical heaters (Thermocoax). In this way it possible to vary the temperature independently in the three part of the loop so to study the influence oh this parameter on the deposition behaviour.
Temperature are measured through k-thermocouples set in S1, on the observation pipe and on S2.

The test matrix

In the first test campaign a stoichiometric quantity of a solid getter was melt in the liquid alloy, in order to reach the lowest O_2 concentration possible.
This to confirm that the vapour tension of the LBE is negligible in the formation of the black dust.
During the campaign three tests have been realized. The first one aimed to understood whether the vapour pressure of the LBE was really negligible then the oxides transport phenomena from the melt to the Ar.
The second and the third ones aimed to investigate whether the temperature and the different geometry of the cross section affect the dust deposition mechanism.

Here below it is possible to see the three test matrixes stated for the tests performed in the first characterization campaign.
The first one refers to a PIF configuration in which the Ar outlet was dispersed in the atmosphere.

	S1	*ObservationPipe*	*S2*
Teperature	300°C	300°C	Room temp
Ar flow rate	8l/h		
Duration of the test	360		

Table 16 – Test matrix of the first experiment: outgas in atmosphere

Table 17 and Table 18 show the experimental start up for the second and third tests. During these test instead of release the outgas in the atmosphere, it was ricirculated by the mean of a pump. This in order to increase the quantity of powder produced

	S1	*ObservationPipe*	*S2*
Teperature	400°C	400C	Room temp
Ar flow rate	8l/h		
Duration of the test	288h	288h	288h

Table 17 – Test matrix of the second experiment: gas recirculation in the loop

	S1	*ObservationPipe*	*S2*
Teperature	400°C	Room temp	400°C.
Ar flow rate	8l/h		
Duration of the test	552h	552h	552h

Table 18 – Test matrix of the second experiment: gas recirculation in the loop

In all the tests performed, during the first campaign, the gas flow rate was 8l/h. It was bubbled 20cm under the free surface, in order to perturbate the surface and enhance the transfer of the lead oxides from the liquid phase to the gas one.

Second campaign

The second device

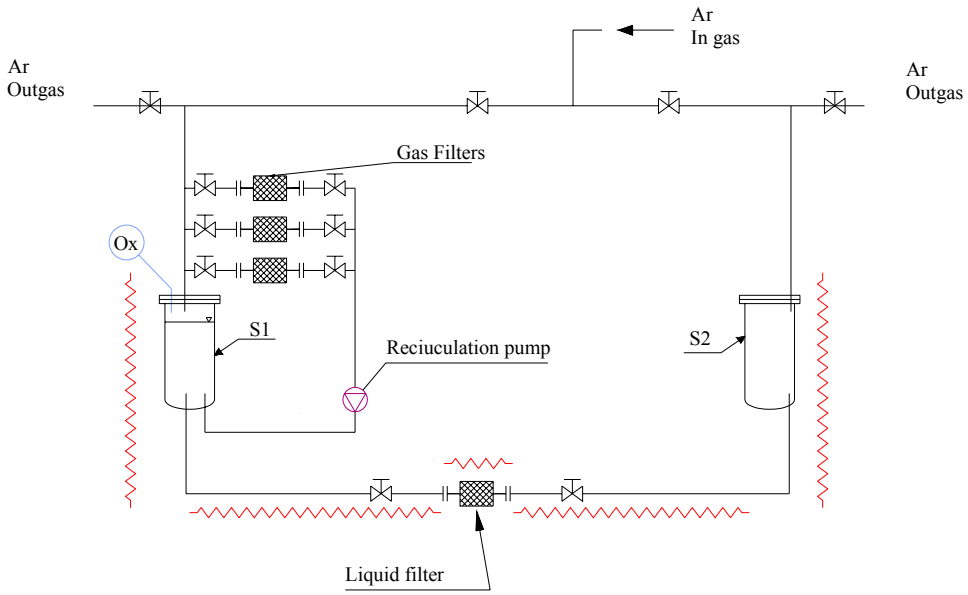

Figure 4-3 – PIF II lay-out

The PIF II loop is composed by two little tanks (S1 & S2) jointed by for the transfer of the LBE.

S1 is tank as a test section while S2 is the storage and the conditioning tank.
As a matter of fact, the PbBi ingots are melt in S2, where, once in he liquid phase, O_2 or H_2 are added due to the O_2 concentration foreseen for the test. Once reached the O_2 concentration desired, the liquid metal is transferred in S1. It pass trough a poral filter so to be freed from the lead oxides slags eventually presented.
S1 is the test section, aiming to reproduce the CIRCE conditions (T max, Ar max flow rate).
A gas injector is placed 20cm under the melt free surface so to bubble gas and to perturbate the liquid metal mass. In order to break the lead oxide crust eventually present on the metal surface, a mixer has been installed.
Once the test starts, the gas ricirculated from the pump is injected in S1. It bubbles in the melt alloy and pass through three gas filters (poral ϕ 5μm) set in parallel. After that the pump reinjects it in S1.
S1 and S2 are hated separately thanks to electrical heaters (Thermocoax). While the gas filters are at room temperature.
Temperature are measured through k-thermocouples set in S1, in the melt metal and on its experlal surface.
Moreover, an Oxygen sensor, $Bi|Bi_2O_3$ (ref cahp 2) is placed in S1 in order to monitor the O_2 concentration.

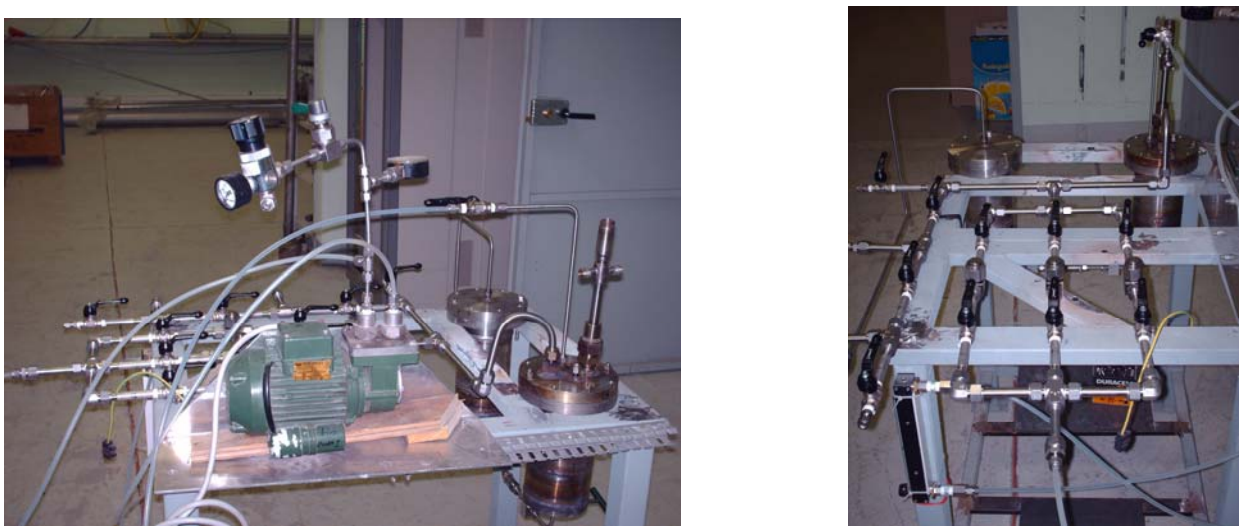

Figure 4-4 – The PIF II: Image of the a whole of the facility and particular of the filters set in parallel

The test matrix

The test campaign lasted for seventeen days. Since the three filters are in parallel, the flow rate through them can be assumed the same, and exactly one third of the total flow rate (10 l/h)

Test conditions	
Temperature	400°C (Tmax ICE)
Total flow rate	10 Nl/h
C_{O_2}	Saturazione a 400°C

Table 19 – Test parameters

In Table 19 are listed the test parameters used to perform the first run of the second qualification campaign. Some working conditions are similar to those of the scheduled test for the 6th European Framework Programme.

The total duration of the test has been divided in different temporal unit so to identify a formation rate (hourly/daily), which is set in Table 20.

1st Filter	*2nd Filter*	*3rd Filter*
5 Days	*17* Days	*11* Days
9 Days		*1* Day
3 Days		*5* Days

Table 20 – Test matrix

After each period the filter was insulated (thanks to the valves on the ingas and outgas) and removed. It was cleaned and the powder found in it and in the filter body weighted with a very sensitive balance (± 0,00001g).

Results

After each test the device was stopped and the post analysis performed. The powder was collected by the mean of a dedicated instrument so to be immediately ready for the SEM analysis.
The SEM at the Brasimone centre is able to realized not only high resolution photos but also the analysis of the composition (wt% & At%) of the compounds under investigation.

The first capmaign

The powder was collected by the mean of a dedicated instrument so to be immediately ready for the SEM analysis.
The SEM at the Brasimone centre is able to realized not only high resolution photos but also the analysis of the composition (wt% & At%) of the compounds under investigation.

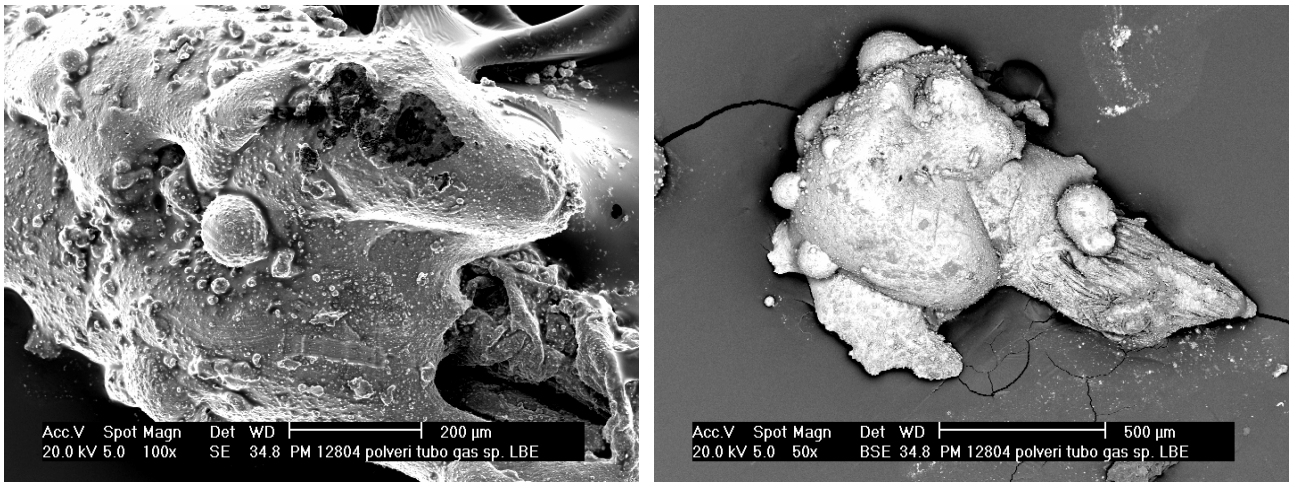

Figure 4-5 – SEM immane of the particles collected in the outgas line of the PIF I

At the end of the first test, the PIF I was stopped and inspected. Both in the observation pipe and in S2 any powder was found.
Only in the outgas line (Figure 4-5) a very few amount of particle were detected.
These particles were composed by Lead and Bismuth, in a percentage of 72,89 wt% and 22,61% respectively (Figure 4-6).
The total powder amount was so few that it was not possible to weight it, even with a very sensitive (± 0,00001g) balance.

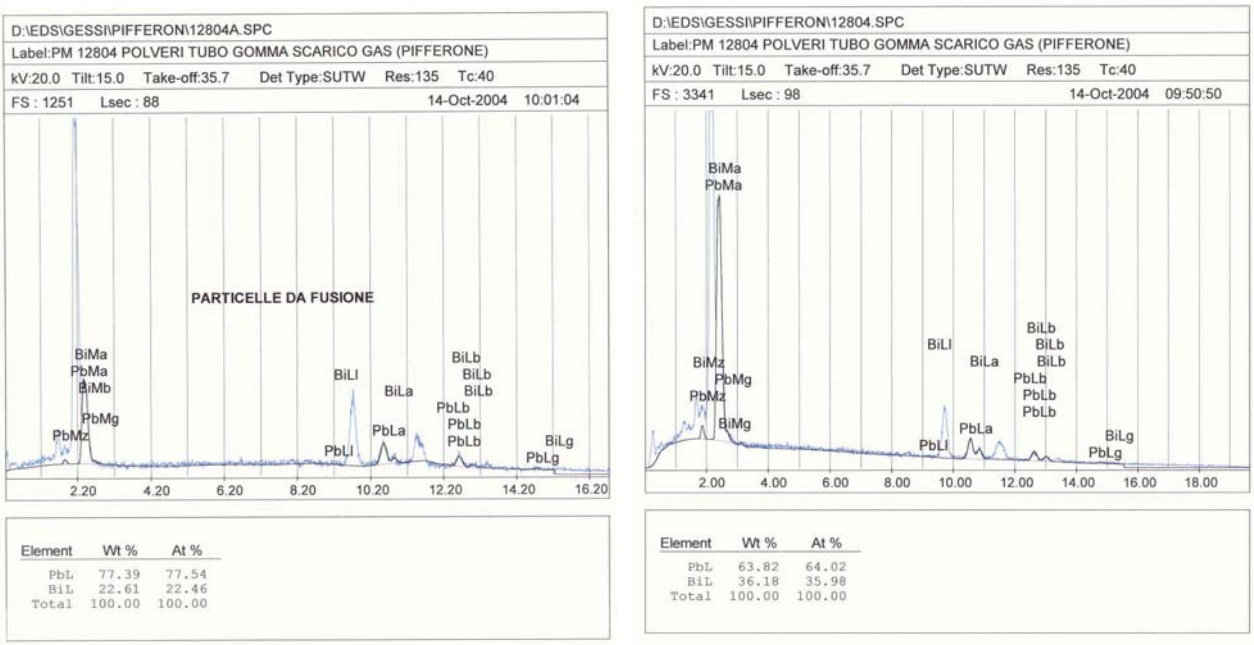

Figure 4-6 – SEM quantitative analysis of the powder in the outgas line

After the first test the PIF I was modify, adding a pump. This was done in order to increase the exposure of the alloy with the cover gas.
The low powder quantity found in the first test suggest that the contact duration between the gas and the liquid phase could be too short to allow the diffusion of the oxides from the LBE to the Ar.
So the gas circuit was closed, in order to force the gas to cycle its pass through the alloy.

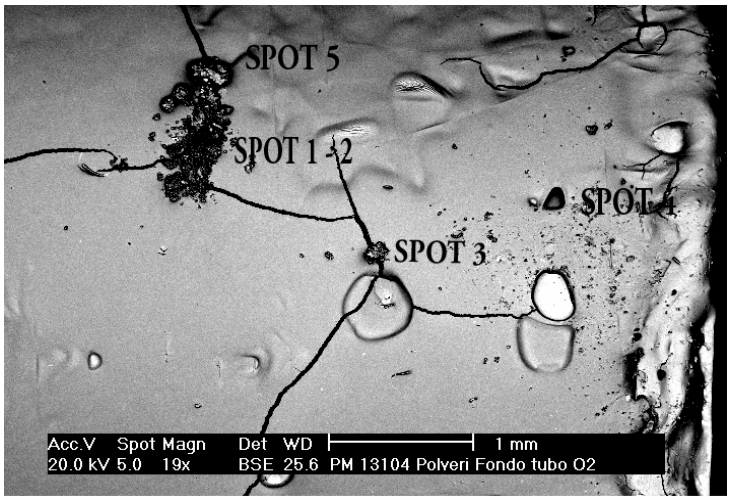

Figure 4-7 – O2 port light powder detected

After the second test ended, the PIF I was stopped and inspected. In S2 any powder was found, while in the observation pipe (O2 lightport) some dust was found (Figure 4-7).
Since the SEM does not perform the stoichiometric analysis, it not possible to know exactly which elements are present. Anyway it is possible to hypothesize the presence of Mg oxides due to the reduction of the LBE and Pb oxides.

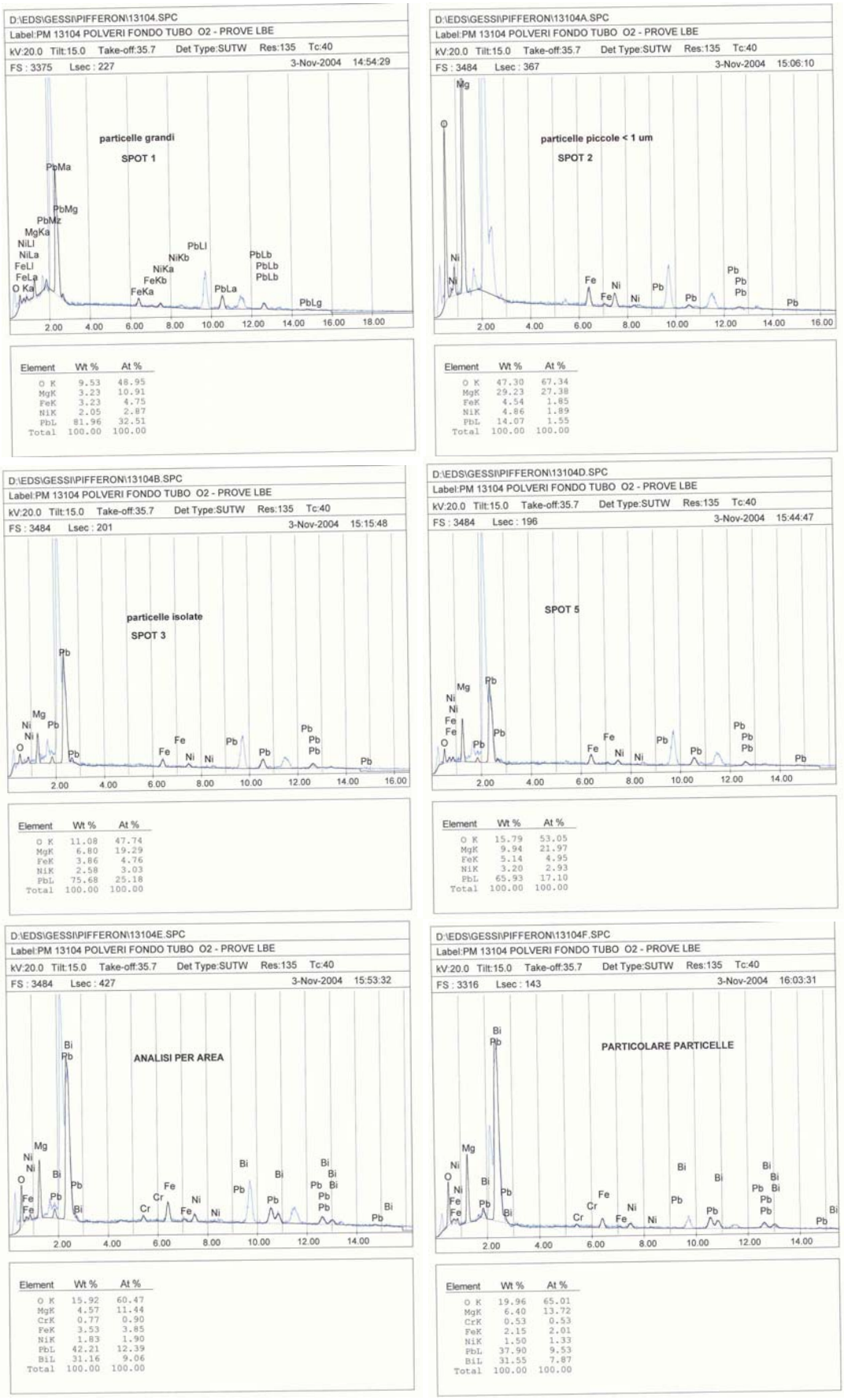

Figure 4-8 – SEM quantitative analysis of the powder in the O2 port light

As a matter of fact the SPOT1 (Figure 4-8) is composed of large and small particles (>1μm the first and < 1μm the second). The small particles are composed of Oxygen, Magnesium and Lead (48,9%, 10,91% & 32,51%), while the fine ones are mostly oxygen and Magnesium.
SPOT2 and 3 are lead oxides while SPOT 5 is made by both of Lead and Magnesium oxides.
An area analysis shows that the predominant species are Oxygen, Magnesium Lead and Bismuth (this last one in a negligible percentage if compared to the other three).

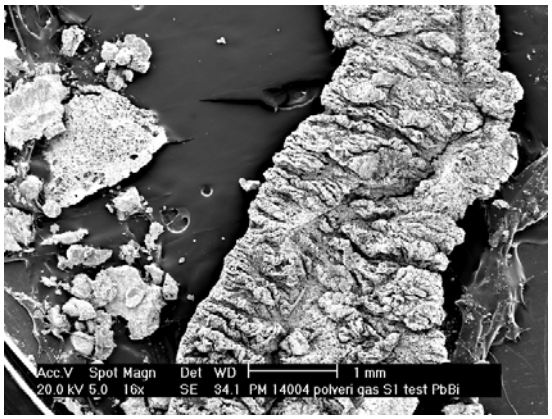

Figure 4-9 – Third experiment collected material

After the conclusion of the third test, the PIF I was stopped and inspected. In both the observation pipe and S2 any powder was found, while it was collected from the pipe connecting S1 with the observation pipe (Adduction pipe) (Figure 4-7).

When the flange of S1 was open to remove the powder a large oxides crust was found. On its surface some grams (~8g) of powder was detected . this could mean that the stripping effect of the gas decrease due to the thickness of the floating oxides. While the quantity of powder found in the adduction pipe was barely enough to be weighted, actually, only few particles were found

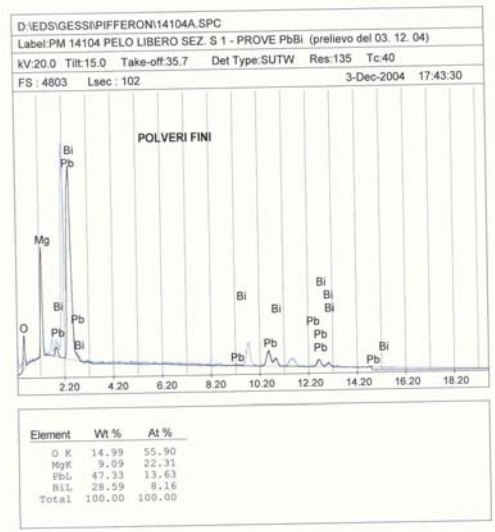

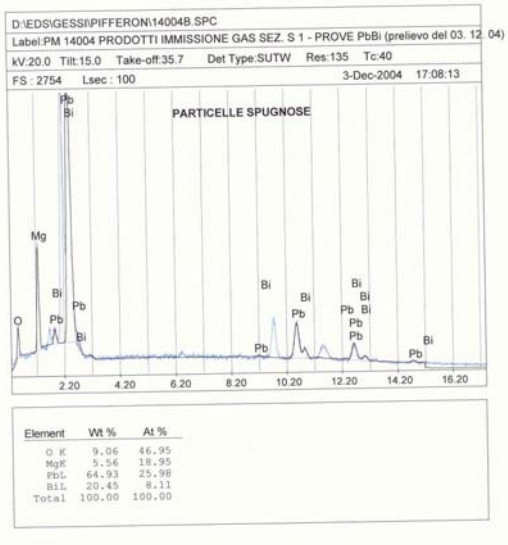

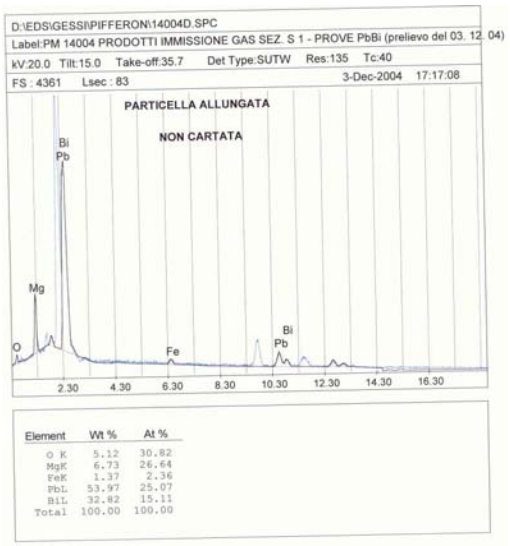

Figure 4-10 - SEM quantitative analysis of the powder in S2

All the analysis preformed show that the predominant species are Oxygen, Magnesium Lead and Bismuth (this last one in a negligible percentage if compared to the other three), also in this case (**Errore. L'origine riferimento non è stata trovata.**).

The second capmaign

After the conclusion of the first run of the PIF II the post test analysis was performed. First of all a SEM analysis of the powder was dome and the outcome confirmed the presence of lead oxides in the highest quantity then all the other compounds.

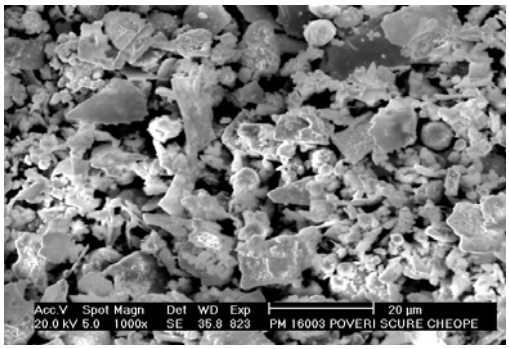

Figure 4-11 – SEM immane of the dust of the 1st filter of the PIF II

The photo shows the typical lead oxides shape, detected also in the big facilities working with LBE.

Filter	Days	Grams
1st Filter	3	9,20
	5	16,58
	9	28,43
2nd Filter	17	53,72
3rd Filter	1	2,05
	5	14,78
	11	33,41

Table 21 – Powder generated during the test campaign Grams Vs Time

After the weight process, whose result can be seen in Table 21, the data were plotted in order to find out if a proportion between time and powder production do exist..
The results are shown in Figure 4-12, while Figure 4-13 show the data best fit. From this last graph il it possible to state the existence of a linear relationship between the production rate and the time of work.

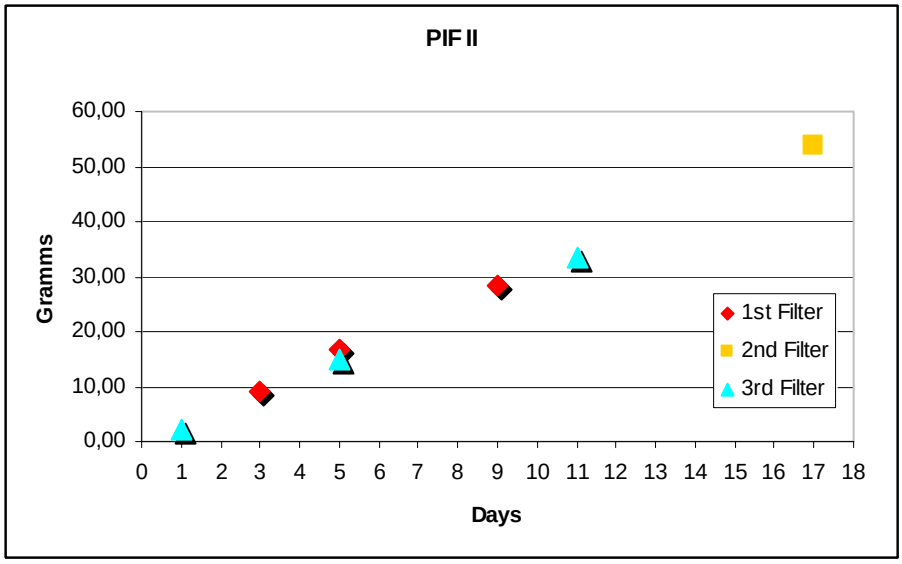

Figure 4-12 – Graph of the powder quantity produced vs. the days

Discussion

The two different campaigns performed allow to confirm some literature informations and to add something new to the knowledge of the phenomena.
In the first test with PIF I, the lead Bismuth has been reduced by the mean of a solid oxygen getter such as the Magnesium is.
When the test was stopped a negligible amount of dust was, actually, found. This confirms that the LBE vapour pressure contributes marginally to the formation of the power.
When the facility was stopped and inspected to extract the dust, it was opened and the melt alloy got in contact with the air. It is evisageble that some oxygen dissolved in the alloy. This is partially confirmed by the second test and, more strongly, by the third one. As a matter of fact in those tests some lead oxides particles were found.
Any way the total amount of powder was so few that it was not possible to weight it.
The SEM analysis showed that the few quantity of powder detected was composed mainly by Lead and Magnesium oxides.
From the third test, it is possible to suppose that the presence of floating oxides on the free surface of the liquid metal obstacles the transfer of the oxides from the liquid to the gas.
As a matter of fact the crust acts as a barrier for the mass transfer mechanism obstaculating the gas stripping effect. Even with a continuous Ar bubbling the crust was thick enough to block the phenomena.
This lead to the realization of the PIF II, equipped with a mixer in order to fight the crust formation and to simulate the real liquid turbulence in a pump tank or in a pool configuration facility.

Three runs were scheduled for the PIF II, and up to now only the first is finished.

Any way, from this first run some very interesting data were collected and it was possible to find a correlation between the powder production rate vs the time, at fixed temperature and O_2 concentration (ref Figure 4-13)

$$r = 3{,}129 gr / d$$

Where r represents the daily black powder production.

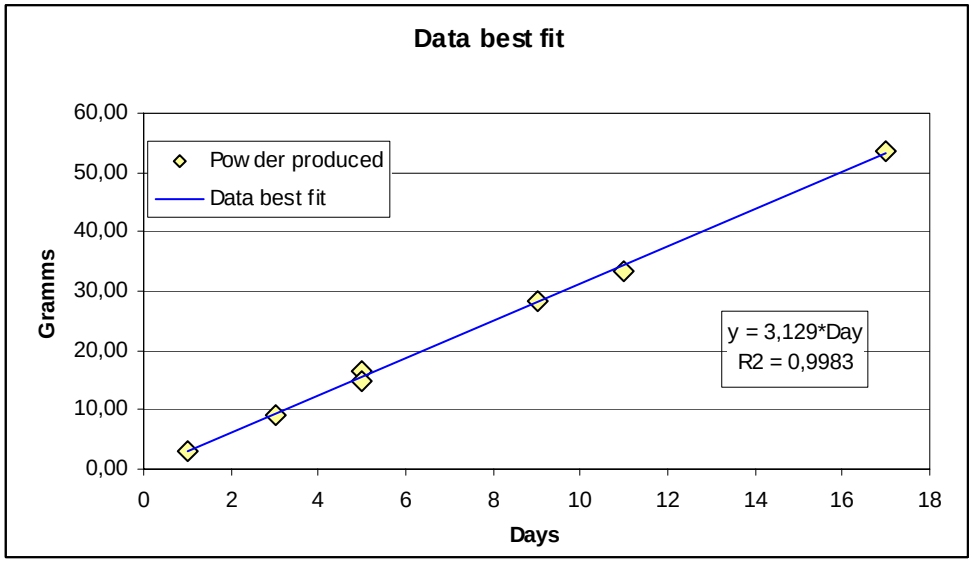

Figure 4-13 – Data best fit of the data

In the future, new test are foreseen in order to confirm the first run outcome. It is programmed to repeat this first test in order to verify the reliability of the data obtained. Then the temperature and the O2 concentration will be modified in order to individuate whether a dependence among these data do exist.

Bibliografy

[1] J Buongiorno, N.E. Todreas, M.S. Kazimi, *Heavy metal aerosol transport in a LbBi coolled fast reactor with in vessel direct contact steam generation,* Nuclear technologu, 2004

[2] MIT-ANP, INEEL, *Design of an Actinide Burning, Lead or Lead Bismuth cooled reactor that produces low cost electricity,* Annual Project Status Report, July 2002

[3] P. Michelato, E. Bari, L. Monaco, D. Sertore, A. Bonucci, R. Gainnantonio, M. Urbano, L.Vitali, P. Turroni, L. Cinotti, *Theoretical and experimanetal evaluation of the windowless interface for the TRASCO-ADS project,* Journal of vacuum and technology, 2004

[4] R.A. Kushnaryov, P.N. Martynov, V.P. Mel'nikov, A.K. Papovyants, A.M. Posazhennikov, I.V. Yagodlin, *Studies on the process of formation of heavy coolant aerosol and its characteristics,* Comunication between IPPE Obnisk and ENEA

5. Oxygen measurement and system purification

Abstract

Impurities detections in liquid metals is on of the most important tasks in the developing of ADS systems technologies. Dissolved oxygen and metal oxides are the most dangerous impurities that could affect a Pb-55.5Li cooling/target system, especially for system plugging problems.
The accurate measurement of the oxygen concentration in the liquid lead-bismuth eutectic, as well as in the pure lead alloys for use as coolant in nuclear systems or as liquid spallation target for high neutrons source or accelerator driven system is a critical issue for defining the active oxygen control that will first of all prevent the contamination of the liquid system by lead and bismuth oxides, as well as, possibly, to ensure an efficient corrosion protection of the iron based alloys structures if the self-healing oxide layer method is chosen.
The monitoring of dissolved oxygen is also a fundamental tool in the field of metal structures protection. Keeping oxygen in a controlled range of concentration, i.e. in this specific case $C_{O\,(MgO)} < C_O < C_{O\,(PbO)}$, induces the formation of oxides layers over the surfaces of the containing steels, protecting them against corrosion phenomena. Due to this twofold aspect of dissolved oxygen, its concentration monitoring becomes of primary importance.
This chapter will focus on the on-line oxygen monitoring system development and more particularly on the description of the test to define the reliability of the electrochemical sensors. And how they were improved.

Intoduction

The development of the heavy liquid metal chemistry control and monitoring is one of the issues that is critical for nuclear systems using lead alloys either as a spallation target or as a coolant. Indeed, the chemistry interacts with at least three operating specifications of any nuclear system:

1. The contamination control, to ensure stable hydrodynamics and heat transfer during service-life time that means to avoid lead oxide clogging or even corrosion products plugging due to mass transfer in a non isothermal system, to avoid deposits that eventually reduce the heat transfer capacity, etc.;
2. The corrosion control, to ensure sufficient resistance of the structural materials during the expected service life-time, which includes the self-healing oxide protection layers for iron-based alloys that requires oxygen control, etc.;
3. The radio-activation control, to ensure a safe management of the operations and maintenance phases;
4.

These three requirements refer all to the chemistry control in lead alloys systems as regards the oxygen and others relevant impurities such as the corrosion products, spallation and activation products: control processes in relation with monitoring systems have to be developed and/or qualified for the application to a demo ADS system for both the coolant loop, refereeing to the primary circuit, as well as for the spallation target loop.
The principal scopes of development or validation concern at first the two following issues:

- The development of on-line monitoring systems for dissolved oxygen, as well as of the processes required to adjust the oxygen activity to a specified value;
- The characterisation of impurities and definition of purification process and monitoring method by liquid metal sampler and analytical techniques;

State of the art

The use of the ionic conduction properties of some solid electrolyte, and in particular the zirconia based ceramic, allow to make electrochemical cell assembly that allows the measurement of dissolved oxygen in liquid metal system. This is known as the electromotive force measurement in open circuit or as the galvanic cell method.
This technique presents several well known advantages such as :

- Specific to the dissolved oxygen, but the bounded oxygen, such as in oxide, is not taken into account;
- Rapid and continuous sensor, that is able to be implemented directly on the system, provided the leak tightness of the seal in between the liquid metal and the ceramic;
- Wide concentration range covered by one single sensor as well as it potential operating temperature range;
- No relation with the size and contact area of the electrodes.

In addition, the sensor makes hardly any disturbance on the measured system, and is in principle versatile, as it can be used on a number of applications.

However, its well-known limitation was its use at required operating temperature higher than 500-600°C, because of the high cell resistance that increases with decreasing temperature, as well as the irreversibility of the cell. In addition, the poor thermal shock resistance requires special care to prevent thermal cracking of the solid electrolyte. A specific protection from rapid temperature fluctuation shall be provided. Another solution is to design sensor as a consumable item. The service life is always reported as being in the range of the tens to hundreds of hours only.
Although the principle and the application are well known since the 50ies, especially at the laboratory scale for the measurement of basics thermodynamic data, its real application as industrial oxygen sensors began in the late 80ies where its applications covered lots of applications, from the automotive industries (Lambda sensors) to the gloves box gas control. However, some particular and earlier application such as the sensor for the steel making industry, which is used to measure C/CO ratio, as well as the sensor for the liquid sodium to be used as nuclear coolant, could be noticed [1] . In addition, the Russian institutes developed a specific application for the oxygen control in Lead-bismuth eutectic to be used as coolant in nuclear submarines in the late 70ies-80ies [17] [18] [25], whose teams paved the ways for this very specific instrumentation in heavy liquid metal coolant with the use of very specific multi layers pellet type sensor. Since the mid-nineties, development and testing of new sensor design based on yttria stabilised zirconia or magnesia stabilized zirconia were conducted worldwide, including in Russia [2][3][5][6][7][8][11][15][16][19][20][22][23][27][28] .
The main requirements for an on-line oxygen sensor are as follows: accurate in such a low oxygen concentration range, reliable, predictable and safe for long-term nuclear operation. For instance, one of the main constraint as regards the safety for such system is related to the ceramic breakdown: any leaks of radioactive liquid metal outside the system must be prevented, as well as any ceramic pieces running in the nuclear loop. However, some limitations appeared on some sensors [12], such as the ceramic relative fragility, as well as the time drift that is often observed that will delay for a while their direct implementation on nuclear system. However, the Russian sensor design [28] was already used in the nuclear loop of the BOR-60 lead channel [21], which operated for about 100 days.

Principle

Sensors are based on the electromotive force (EMF.) measurement method at null current for a galvanic cell.
This cell is built with a solid electrolyte: zirconia doped with either magnesia or yttria as this doping element stabilizes the ceramic into the tetragonal form, which allows oxygen ions to cross the electrode and to conduct (temperature and oxygen concentration fixed). Although the Russian feedback indicated the achievement of such sensors for the low operating conditions expected of the lead alloys [20][21], their assembly was not straightforward at first as it was considered that such electrodes and cells would not work for low temperature (<600°C), because of the irreversibility of the electrode, and because of the too high cell resistance.
In **Errore. L'origine riferimento non è stata trovata.** he working principle of the galvanic cell is described: (1) is the reference electrode, with a constant Oxygen concentration (C_{O2}), while (2) shows the eorking electrode). This is, as a matter of fact, the liquid metal phase where the unknown C_{O2} is.

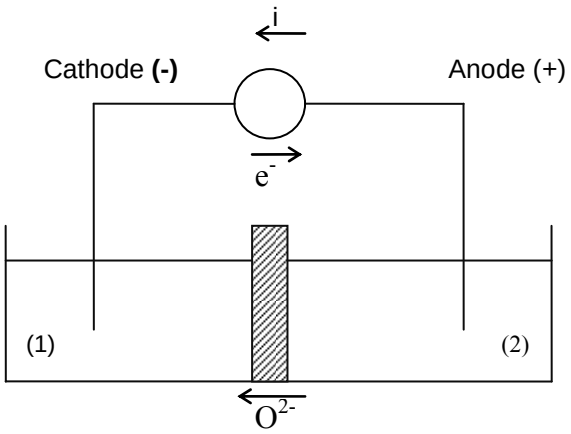

Figure 5-1: **Galvanic cell principle**.

Sensors assembly is made within the laboratory and is now considered as a routine procedure.
Suppliers can be found worldwide [22] which provide yttria doped zirconia, FzY grade, 8.1% in yttria and ceramic magnesia and yttria stabilized zirconia [10][19][6].
On-purpose ceramic can be synthesised and fired with the required characteristics and shape [2].
Assembly is done in the open air. Ingots of pure metal and oxides powder are mixed to get a liquid metal internal reference at the operating temperature with only a slight excess of its oxide. 10% to 50% of oxide is reported as satisfactorily [9].
The air in excess is consumed during the first use, corresponding to the activation, due to the oxidation of the reference metal. The activation of the sensor is done during the calibration procedure or during its first use, the first step of which is the immersion of the sensor in a LBE melt followed by a temperature increase. Once the sensor is giving a stable EMF output, the reference is considered at the thermodynamic equilibrium, and the sensor is said activated. This is done in a matter of minutes at 450°C – 500°C.
The choice of the reference system depends widely on various parameters, such as for instance the gas or liquid phase, liquid metal are known to provide a better contact with the solid electrolyte, and then a lower cell resistance at comparatively lower temperature. The use of low melting point metal allows favour the use of the sensor in a higher temperature range. In addition, the contact lead wire must be compatible with the liquid metal melt of the reference. For instance, molybdenum presents a low solubility in bismuth, which is favourable. To the opposite, platinum or iridium metal, which are the typical lead wired for such electrochemical cell, dissolve in liquid bismuth, forbidding their use. The chemical compatibility with the solid electrolyte must be correct as well. These considerations explain why the choice for the reference systems focused firstly on the bismuth and indium systems.
The reference systems are:

- Bi/Bi_2O_3 (mp. 271°C), Mo lead wire ;
- In/In_20_3 (mp.157°C), Mo lead wire;
- Air, Pt lead wire;

Of whom Bi/Bi_2O_3 and In/In_20_3 were tested.

Theory

This analysis is done for pure lead as well as for the lead-bismuth (55% in weight) eutectic.

The method of the electromotive force (EMF.) measurement with null current can be applied to the measurement of the dissolved oxygen in liquid lead-bismuth alloys. A typical electrochemical galvanic cell that will be subsequently referred to as EC sensor, is as follows:

Mo, Metal + metal oxide (reference) // $ZrO_2 + Y_2O_3$ // Pb + PbO (lead alloys solution), steel (1)

where the yttria stabilized zirconia (YSZ) ceramic, which conducts specifically oxygen ions, separates 2 medias showing different oxygen activities : an electromotive force is then formed across the solid electrolyte. If one of the media is defined to act as a reference, so as to maintain constant the oxygen partial pressure to a defined value, then the EMF. is a function of the oxygen activity in the other medium.

Assuming pure ionic conduction in the solid electrolyte, and assuming that all transfers at the various interfaces developed in the electrochemical cell are reversible, the Nernst relation giving the theoretical EMF. can be written :

$$E_{th} = \frac{RT}{4F} \cdot \ln \frac{P_{O2(reference)}}{P_{O2}} \quad (2)$$

With:
E_{th} in Volts,
R the perfect gas constant (8.31441 J/mol/K),
F the Faraday constant (96484.6 C/mol), T the temperature (Kelvin),
P_{O2} the oxygen partial pressure in the media.

The oxygen partial pressure of the reference, is defined by the following reaction, in case of a metal (M)/metal oxide (M_xO_y) reference, where x and y are respectively the stoichiometric coefficients for the metal and the oxygen.

$$\frac{2x}{y} M_{(liquid)} + O_2 \Leftrightarrow \frac{2}{y} M_x O_{y(solid)} \quad (3)$$

All reactions are written so that it corresponds to the consumption of one mole of oxygen. The units of the free enthalpies of formation are then expressed in J/mol of oxygen O2.

As the reference is built so as to present a constant oxygen partial pressure, both the metal and its oxide are present in excess to ensure the thermodynamic equilibrium of the reaction. In addition, the liquid solution corresponds to the pure metal, so that the activities of both the reference and its oxide are equals to one. The activities products of the oxide reaction of formation in lead alloys is then as follows:

$$\ln P_{O2\ reference} = \frac{\Delta_r G^0_{reference}}{RT} \quad (4)$$

The oxygen partial pressure in the lead alloy melt, is given by the thermodynamic equilibrium of lead monoxide, considering that it is the most stable oxide in lead bismuth eutectic.

$$2Pb_{(liquid)} + O_{2(gas)} \Leftrightarrow 2PbO_{(dissolved)} \quad (5)$$

The activities products of the lead oxide reaction of formation in lead alloys is then as follows using the oxygen activity defined in Eq. 7

$$\Delta_r G^0_{PbO} = -RT \cdot \ln \frac{a^2_{PbO}}{a^2_{Pb} \cdot P_{O2}} \qquad \text{and then} \quad \ln P_{O2} = \frac{\Delta_r G^o{}_{PbO}}{RT} + 2 \cdot \ln \frac{a_O}{a_{Pb}} \tag{6}$$

The saturated oxygen concentration for lead and LBE are derived from Eq. 12 and Eq. 13:

Lead: $$\ln C^*_{o(wgt\%)} = A - \frac{B}{T_{(K)}} \qquad \text{with A = 7.3683 and B = 11512.925} \tag{7}$$

LBE: $$\ln C^*_{o(wgt\%)} = A' - \frac{B'}{T_{(K)}} \qquad \text{with A' = 2.7631 and B' = 7828.789} \tag{8}$$

Lead activity is equal to unity in pure lead solution, and is given by the following Russian relation in LBE solution reported in [Courouau, 2002b]:

LBE: $$\ln a_{Pb} = -0.8598 - \frac{135.21}{T_{(K)}} \qquad \text{or} \qquad \ln a_{Pb} = -\alpha - \frac{\beta}{T_{(K)}} \tag{9}$$

The free enthalpies of formation for the various oxides are expressed by the following relations, assuming that all relations are given for the consumption of one mole of O_2 :

$$\Delta G^o_{(J/mol)} = \Delta H^o - \Delta S^o \cdot T_{(K)} \tag{10}$$

Calculations are made with the help of the HSC database software (version 4.1), which represents a compilation of some of the latest thermodynamic data available. The free energies of formation are linearly regressed on a limited temperature range, 400-1000K, so as to determine the standards enthalpy and entropy by the least mean squares method. The latter data, standard enthalpy and entropy, are constant over the temperature range.

$\Delta G^o_{(J/mol)} = \Delta H^o - \Delta S^o \cdot T_{(K)}$	ΔH^o (400-1000K) J/mol	ΔS^o (400-1000K) J/mol/K
4/3 Bi +	-389140	-192.6
2 Pb	-437608	-199.1
4/3 In +	-618674	-216.8

Table 22: Main oxides free enthalpies coefficients for the 400-1000 Kelvin temperature range per mole of oxygen O_2 consumed.

The general relationship for a metal-metal oxide reference could then be derived from the Nernst relation, assuming a pure ionic conduction in the solid electrolyte:

$$E_{th} = \frac{\Delta G^o_{reference} - \Delta G^o_{PbO}}{4F} - \frac{RT}{2F} \ln \frac{a_O}{a_{Pb}} \tag{11}$$

By using the following constants:

$$a = \frac{\Delta H^o_{reference} - \Delta H^o_{PbO}}{4F} \tag{12}$$

$$b = -\frac{\left(\Delta S^{o}_{reference} - \Delta S^{o}_{PbO}\right)}{4F} \tag{13}$$

$$c = -\frac{R}{2F} \tag{14}$$

These constants allow to writing down simplified relations:

(Lead) $$E_{th\,(V)} = a + b \cdot T_{(K)} + c \cdot T_{(K)} \cdot \ln a_o \tag{15}$$

(LBE) $$E_{th\,(V)} = \left(a + c\beta\right) + \left(b + c\alpha\right) \cdot T_{(K)} + c \cdot T_{(K)} \cdot \ln a_o \tag{16}$$

Hence for saturated oxygen solution, the previous relations are only depending on the temperature:

(Lead) $$E^{SAT}{}_{th\,(V)} = a + b \cdot T_{(K)} \tag{17}$$

(LBE) $$E^{SAT}{}_{th\,(V)} = \left(a + c\beta\right) + \left(b + c\alpha\right) \cdot T_{(K)} \tag{18}$$

Finally, these general relations could be simplified by using the (a,b,c) constants and the concentration expressed in weight percent :

(Lead) $$E_{th\,(V)} = \left(a + cB\right) + \left(b - cA\right) \cdot T_{(K)} + c \cdot T_{(K)} \cdot \ln C_{o\,(wgt\%)} \tag{19}$$

(LBE) $$E_{th\,(V)} = \left(a + c\beta + cB'\right) + \left(b + c\alpha - cA'\right) \cdot T_{(K)} + c \cdot T_{(K)} \cdot \ln C_{o\,(wgt\%)} \tag{20}$$

The free energies are in good agreement with the respective energies computed with the use of other databases: JANAF, BARIN 1989; or even the Oxide Handbook, 1982. The slight inaccuracy of these data will affect the theoretical electromotive force calculation by a few millivolts that are assumed as reasonable. Another source of scattering is due to the data coming from the lead activity relation in LBE, which affect only slightly the EMF. by a maximum of 10 mV, as well as from the oxygen solubility relation, which can affects, on the contrary, the EMF to a much greater extent. This is why it is essential to know with a relatively high accuracy the oxygen solubility data. However, there is only one available relation for LBE, known as the Orlov relation, whose accuracy and measurement method are not very well known.

The constants of the Nernst relations can then be calculated, and are reported in the next table for Bi/Bi_2O_3 and In/In_2O_3 reference electrodes for a cell immersed into a lead alloy melt according to the following emf. (E) vs. temperature (T) and oxygen concentration (Co) relationships:

$$E_{(mV)} = K_1 + K_2 \cdot T_{(K)} + K_3 \cdot T_{(K)} \cdot \ln C_{o\,(ppm\,weight)} \qquad \text{for E > Esat} \tag{21}$$

$$E^{SAT}{}_{(mV)} = K + K' \cdot T_{(K)} \qquad \text{for E = Esat} \tag{22}$$

These relations enables to plot the E vs. T (Co as parameter) diagram, which are most useful for reading sensor output as well as for calibration of sensor [19][17].

Apart from the data used for the theoretical assessment, there may be other causes for the sensor not to behave according to the theoretical relations: the electrolyte conduction properties (slight electronic conduction, impurities in the ceramic, etc.), the influence of the reaction at the electrode/electrolyte interface (liquid metal/zirconia reaction, or even traces of impurities depositing on the interface), the cell irreversibility (equilibrium not reached due to an oxygen transfer rate limitation especially at very low oxygen partial pressure), as

well as the instrumental uncertainties. This is why calibration methods are often required [26][9].

The following table synthesises the most useful relations for In and Bi reference sensor in LBE melts.

LBE	Bi/Bi_2O_3 reference (melting point 271 °C)	In/In_2O_3 reference (melting point 157 °C)
$E_{sat}(T)$	$E^{SAT}_{(mV)} = 119.8 - 0.0539 \cdot T$	$E^{SAT}_{(mV)} = -475 + 0.0088 \cdot T$
E (T, a_o), $E > E_{sat}$	$E_{(mV)} = 119.8 - 0.0539 \cdot T - 0.0431 \cdot T \cdot \ln a_o$	$E_{(mV)} = -475 + 0.0088 \cdot T - 0.0431 \cdot T \cdot \ln a_o$
E (T, C_o), $E > E_{sat}$	$E_{(mV)} = -218 + 0.0652 \cdot T - 0.0431 \cdot T \cdot \ln C_{o(wgt\%)}$ $E_{(mV)} = -218 + 0.462 \cdot T - 0.0431 \cdot T \cdot \ln C_{o(ppm)}$	$E_{(mV)} = -812 + 0.1279 \cdot T - 0.0431T \cdot \ln C_{o(wgt}$ $E_{(mV)} = -812 + 0.525 \cdot T - 0.0431T \cdot \ln C_{o(ppm)}$
Ln a_o (T,E) $E > E_{sat}$	$\ln a_o = -23209 \cdot \frac{E_{(mV)}}{T} + \frac{2780}{T} - 1.251$	$\ln a_o = -23.209 \cdot \frac{E_{(mV)}}{T} - \frac{11024}{T} + 0.205$
Ln C_o(T,E) $E > E_{sat}$	$\ln C_{o(wgt\%)} = -23.21 \cdot \frac{E_{(mV)}}{T} - \frac{5049}{T} + 1.512$ $\ln C_{o(ppm)} = -23.21 \cdot \frac{E_{(mV)}}{T} - \frac{5049}{T} + 10.723$	$\ln C_{o(wgt\%)} = -23.21 \cdot \frac{E_{(mV)}}{T} - \frac{18853}{T} + 2.968$ $\ln C_{o(ppm)} = -23.21 \cdot \frac{E_{(mV)}}{T} - \frac{18853}{T} + 12.178$
Ln P_{sat} (T), $E = E_{sat}$	$\ln P^{SAT}_{O2} = -\frac{52362}{T} + 25.67$	
Ln P (T,E) $E = E_{sat}$	$\ln P_{O2} = -\frac{46803}{T} - 46.418\frac{E}{T} + 23.16$	$\ln P_{O2} = -\frac{74413}{T} - 46.418\frac{E}{T} + 26.075$

Oxygen sensors calibration

The corrosion test facilities

The CHEOPE III and LECOR facilities described below are running corrosion tests over different kind of reference structural steels for advanced reactors, in different oxygen concentrations. The online oxygen monitoring is thus of extreme importance.

The Lecor & Cheope III corrosion loops

The corrosion tests in a low O_2 concentration were performed in the LECOR loop. As shown in **Errore. L'origine riferimento non è stata trovata.**, the plant has a "figure-of-eight" configuration, typical for a corrosion loop, with a high temperature branch running from the economiser to the test sections, set at 450°C, and a low temperature branch including the delivery and return pipes between the tank and the economiser, including the by-pass line. The vessel contains a mechanical pump, with submerged impeller, sized to provide the loop with a maximum liquid metal flow-rate of 1 m/s [14]

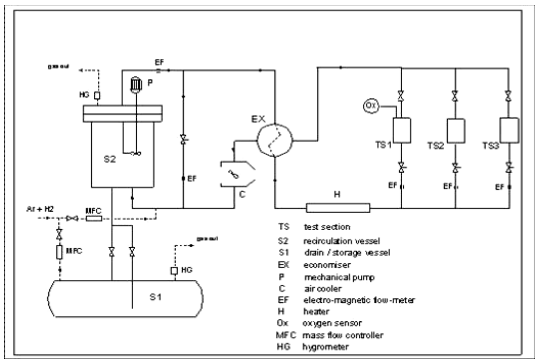

Fig.1: the LECOR loop lay out and photo.

The three test sections TS1/2/3, containing the specimens to be investigated, are placed downstream of the electrical heater and can contain up to 12 specimens each. Test sections 1 and 2 contain the corrosion specimens; test section 3 contains the solid Mg getter[1]. In the steady state, the thermal power provided by the heater is equal to the power extracted by the forced air heat exchanger. This configuration enables a continuous transport of corrosion products from the hot region, where the test sections are located, to the cold region where they are partially released, simulating the actual behaviour of coolant fluid in a thermal production plant. The structural materials of the loop are as follows: the cold part is fabricated in austenitic steel, while the hot region is in ferritic steel representing a good compromise between the requirements of acceptable ductility and corrosion resistance in a liquid Lead alloys.
During normal plant operations the total liquid metal flow-rate available to the test sections is adjusted through the by-pass line, while the liquid metal flow-rate in each test section is automatically controlled by electro-pneumatic regulation valves using feedback signals from electromagnetic flow-meters.

Maximum temperature in the test section (˚C)	**550**
Maximum Pb-Bi flow rate in the pump delivery line (m^3/h)	**4**
Total installed electrical power (kW)	**150**
Maximum heating power of heater H (kW)	**82**
Maximum heat exchange power in EX (kW)	**240**
Inventory of Pb-Bi (dm^3)	**600**
Design pressure (bar)	**4**

Table 23:Main parameters of the LECOR loop

The CHEOPE loop (CHEmistry and OPErations) is installed in the ENEA Brasimone Centre too. It has been used for the in situ passivation experiments in flowing Pb. CHEOPE III, is a part of a multipurpose facility, which has been and is, actually, being used to perform passivation tests in a controlled oxygen environment (with high oxygen activity when compared to the one in the LECOR loop). The structure of this loop consists of a storage tank filled with 40l of Pb, a test section, capable to host up to 18 specimens, and an oxygen sensor, directly put on the top of the Test Section. The flow chart scheme of this facility is

shown in Fig.2. the temperature of the test section was set at 500°C and the flow rate at 1 m/s, like the LECOR loop.

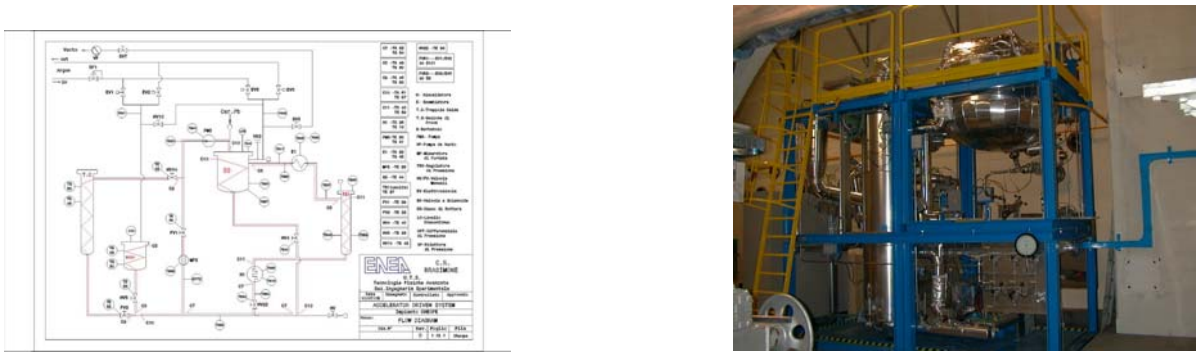

Figure 5-2 : the CHEOPE III loop: lay-out and photo.

The use of Pb has been a great challenge for the operation of the facility. The monitoring of the temperature acquired a critical role, as well as the management of the temperatures in the gas phases. The pump vessel, which is the largest component of the cold leg, was kept at 420°C, using a forced air flow cooler. The mechanical pump itself is inserted into a fully sealed chamber, without any rotating seal. The temperature of 420°C is the maximum one whitstandable by the mechanical pump motor, placed inside the sealing chamber. During the first 2000 hours, no mechanical problem was encountered.
The oxygen concentration in LBE were maintained in the range of 10^{-8}~10^{-10}wt.%., by means of solid stoichiometric Mg addiction directly inside the test section 2 and mixture of Ar/H_2 gas bubbling. The Oxygen concentration was measured by an electrochemical sensor (Russian made at IPPE, Obnisk), placed in the TS1, winch gave a constant current output of 670-630 mV ca., corresponding to the above defined concentration range[2], [3],[4]. The correct amount of Mg was determined by checking the dissolved Oxygen concentration using the electrochemical sensor. The Oxygen concentration in the CHEOPE III is being kept between 10^{-6} and 10^{-4} wt% by means of gas bubbling. Again, the concentration is monitored by an electrochemical Oxygen sensor, calibrated for Pb, wich gave a constant output of 300-350 mV, corresponding to the required concentration.

Maximum temperature in the test section (˚C)	**450**
Maximum Pb-Bi flow rate in the pump delivery line (m^3/h)	**3.6**
Total installed electrical power (kW)	**180**
Inventory of Pb-Bi (dm^3)	**50**
Design pressure (bar)	**6**

Table 24: Main parameters of the CHEOPE III loop

Oxygen control methods

The electrochemical oxygen control devices described below are used as an on line monitoring device for both LECOR and CHEOPE III plants located in the ENEA c.r. Brasimone.
In order to perform an active OCS (Oxygen Contol System), a gas injection technique is used: separate addition of H_2 and O_2 to the melt [14] . The reducing conditions required for the LECOR loop need an alloy conditioning before starting the test. A preliminary bubbling of $Ar+H_2$ (3%) is performed in the LBE storage tank. The direct online bubbling is used during the test time in order to maintain the required environment.

Metallic Mg has been added to the LBE in the LECOR loop before the first experimental campaign, as "oxygen getter". A second addition was performed during the test activities. Being the Gibbs free energy of the Mg oxide the lowest for all the possible metal oxides that could form in the liquid alloy, this addition gave the formation of MgO, that could be separated easily from the alloy itself. The MgO is transported by the LBE flux into the cold part of the loop itself. No filtration has been performed. This physico/chemical technique could lower the oxygen concentration down to the required level (10^{-8}-10^{-10} wt%)
In the CHEOPE III loop, an oxidizing condition is required: 10^{-5}-10^{-6} wt% of O_2 in the LBE. Only an on line bubbling of H_2 or O_2 was performed, without the addition of any getter, in order to maintain this conditions.

The oxygen sensor probes

The oxygen sensors are made of a porous ceramic SETTO joint with a metallic case.
The ceramic electrolyte, which should be in contact with le melt alloy, is of a cylindrical shape. Its bottom is semi spherical.
The reference electrode and the metallic wire are hosted inside the electrolyte . The metallic wire is joint to the voltmeter.
It is possible to use different kind of reference electrode:

- Bi/Bi_2O_3 (mp. 271°C), Mo lead wire ;
- In/In_20_3 (mp.157°C), Mo lead wire;
- Air, Pt lead wire;

Some tests performed in FZK **Errore. L'origine riferimento non è stata trovata.** demonstrated that even if the Air/Pt sensor is cheaper than the other, it is more complex to be assembled and its output signal for the temperature of interest is very low.
Due to signal amplification problems, the research programme was focused on the calibration of a Bi/Bi_2O_3 sensors supplied from IPPE, Obnisk (Ru) and the design and calibration of a In/In_20_3 sensor.

$Bi|Bi_2O_3$ & $In|In_2O_3$

Both the sensors work in a temperature range from 350°C to 600°C.; difference between them is due to the output signal. As a matter of fact the Bi|Bi2O3 (Figure 5-3) has a positive voltage output signal while the $In|In_2O_3$ (Figure 5-4) outcome varies due to the temperature form a negative to a positive signal.
Another difference concerns the thermal expansion of the two solid electrodes. While the $Bi|Bi_2O_3$ tents to enlarge with the temperature. This affect seriously the ceramic electrolyte and can cause a break. The ceramic electrolyte is surrounded by a metallic clad, when the filling elements melts and increase its volume, it generates a pressure on the glove. This leads to an expansion of the ceramic, which is constrained in the metallic clad. Since the ceramic is fragile, it can break easily.
The $In|In_2O_3$ electrode behaves in a different way and temperature does not affects its volume.
In the Table 25 all the characteristic of the two different oxygen sensor configurations are listed, it is possible to compare the pros and cons of both.

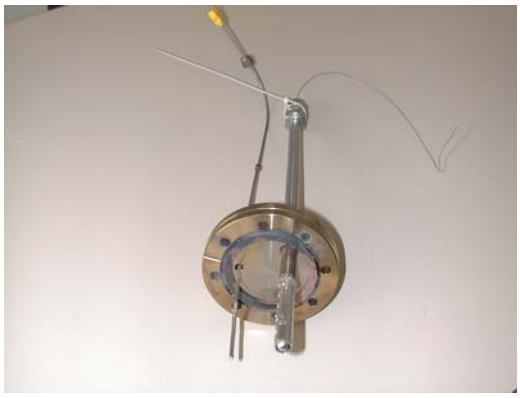

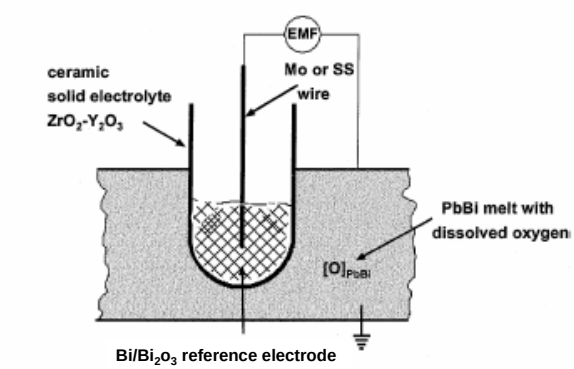

Figure 5-3 - Russian sensors ($Bi|Bi_2O_3$), produced at IPPE, Obnisk.

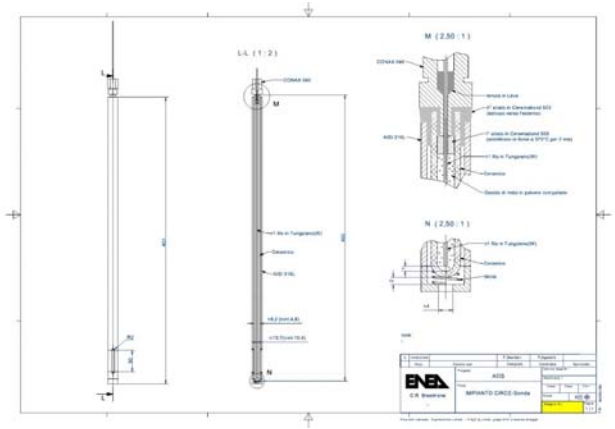

Figure 5-4 – $In|In_2O_3$ sensor design drawing

	$Bi\|Bi_2O_3$	$In\|In_2O_3$
Working temperature	350°C – 600°C	350°C – 600°C
OUTPUT SIGNAL (mV)	Positive	From Negative to Positive
CHEOPE III	200 – 400 mV	-200 – 0 mV
LECOR	500 - 700	150 – 200 mV
Cons	Volume increase with temp.	Very expensive

Table 25 – Comparison between the two filling electrodes in PbBi

During the calibration campaign in Lead, it has been noted that the outcome signal does not vary too much then the one in LBE. Usually it is, at least,10 – 20nV less then the previous one for the same testing temperature.

Calibration experimental procedure

Oxygen Fine Measure experimental device

The OFM (Oxygen Fine Measure) calibration facility is a device built in order to test and improve electrochemical oxygen sensors for liquid metals in stagnant conditions. It consists of a cylindrical vessel, a heating system, an inert atmosphere gas bubbling system and an electronic multimeter. It is schematically described in Figure 5-5.

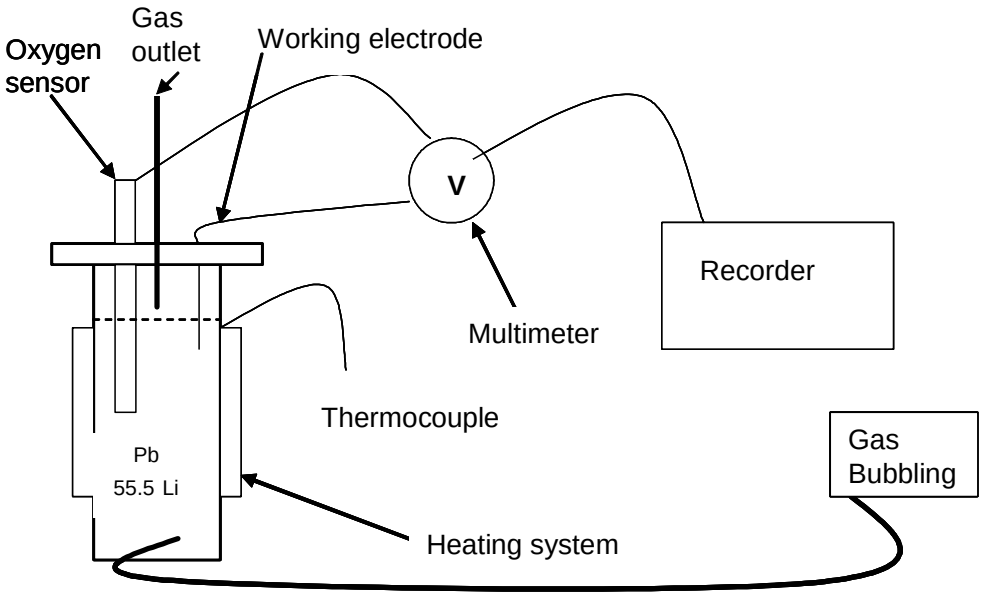

Figure 5-5: Scheme of the OFM calibration device.

The recorder registers the temperature of the vessel, the sensor signal and the gas pressure. The bubbling is performed with Ar coming from a pressured tank. The vessel has an interchangeable top with a swagelock sealing for the gas pipes and the sensor itself.
There are two kinds of vessel tops: a simple one for measures in reducing conditions and a more complex one for oxidizing conditions tests.

Test parameters

Two Bi/Bi_2O_3 reference oxygen sensors, as described above, made by IPPE [2], Obnisk, RU, were calibrated in the OFM facility, recording the EMF signal and their behaviour in different temperatures.
For simulating the CHEOPE III loop oxidizing conditions, i.e. an oxygen concentration of 10^{-5}-10^{-6} wt %, solid Fe was added to the liquid Pb-55.5 Bi eutectic; for simulating the reducing LECOR environment, solid Mg was added and an oxygen concentration of 10^{-8}-10^{-10} wt % was reached. The atmosphere was kept inert via an Ar bubbling inside the vessel.
The calibration process followed the scheme summarized in ***Table 26***.

Step	***Value***
Temperature gradient	**673K – 813K**
Temperature step	**20K**
Gas inlet	**Ar+H_2(3%)**
Number of temperature tests	**2**
Total LBE volume	**0.5 l**
Vessel material	**AISI 316L**

Table 26: summary of experimental procedures.

Two temperature loops were performed in order to check the reputability of the electrode signals.
The acquisition system for the CHEOPE III sensor was a digital one, while the one for the LECOR sensor signal was an analogical data recorder. This is why the EMF graphics are different and the calculation of a tendency line for the analogical graphics was necessary.

Calibration experimental results

After the calibration campaign, the data collected were plotted in order to compare the behaviour of the sensors in different environmental conditions.
Figure 5-6describe the signal, in mV, of the CHEOPE III sensor, while ***Figure 5-7*** the ones of the LECOR electrode.
The graphics displayed from now on are temperature settings in °C vs. EFM signals in mV. They show a quite linear behaviour of the two sensors, in stagnant condition.

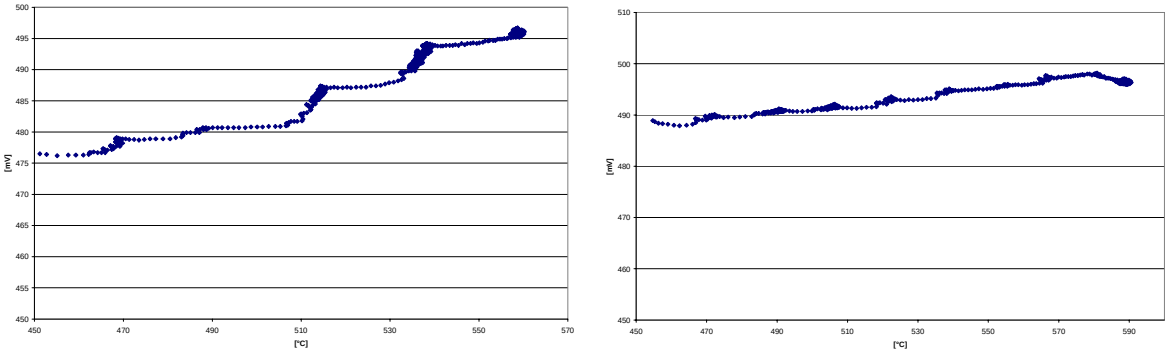

Figure 5-6: first and second temperature test of the CHEOPE III sensor.

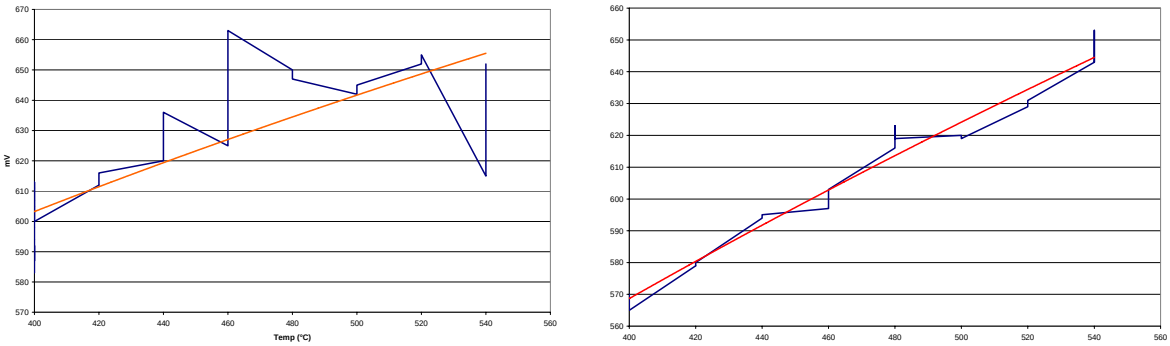

Figure 5-7: first and second temperature test of the LECOR sensor

Figure 5-8 summarizes the experimental results, comparing them with the calculated theoretical curves of FEM at fixed oxygen concentration. The iron oxide curve and the magnesium oxide one are emphasized.

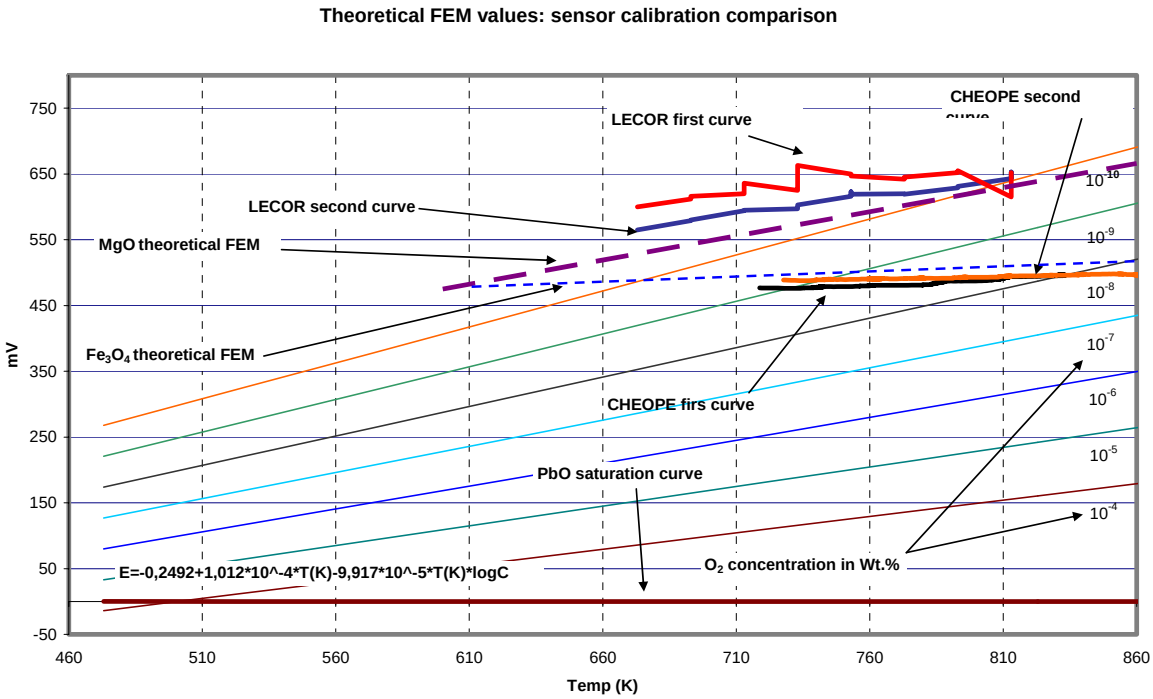

Figure* 5-8*: summary of experimental data and comparison with theoretical oxygen concentration/EMF curves.

It is possible to underline the good behaviour of both the sensors at different temperature plotting the output EFM signal parallel to the temperature variations.
Figure 5-9 and ***Figure 5-10*** show the sensor signal of the LECOR and the CHEOPE III loops.

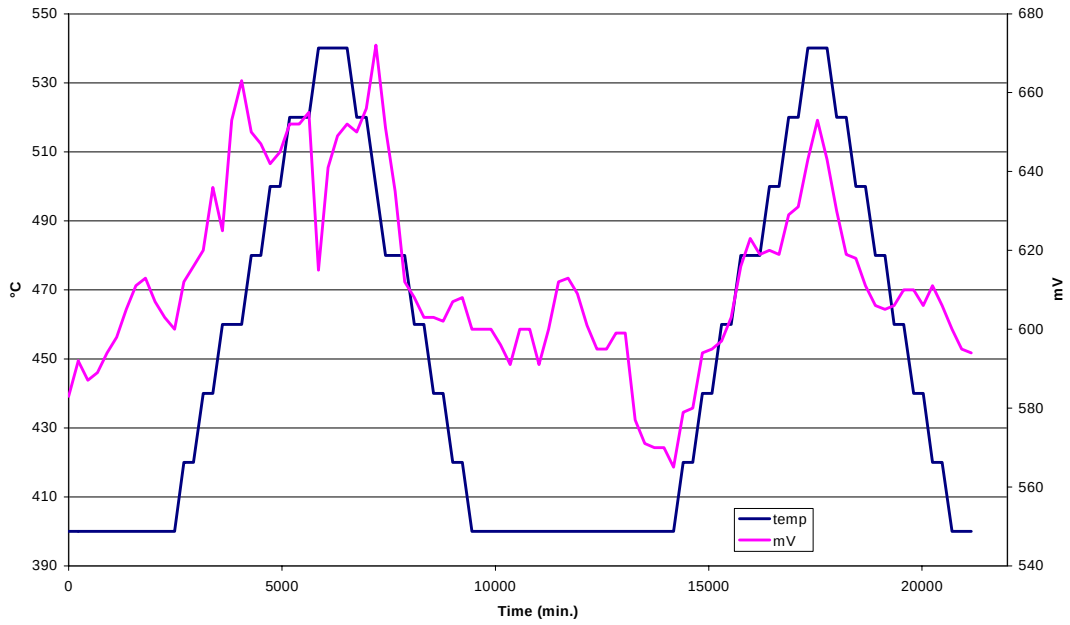

Figure 5-9: FEM signal of the LECOR sensor and temperature variations.

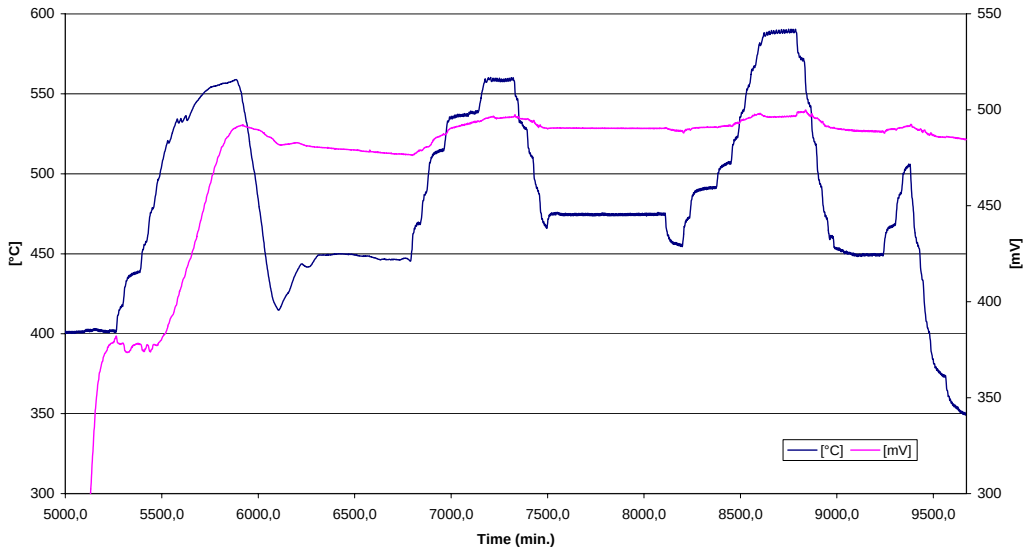

Figure 5-10: FEM signal of the CHEOPE III sensor and temperature variations

Calibration conclusions

Both $Bi|Bi_2O_3$ sensors gave good accordance between expected and experimental data, in stagnant conditions. The EMF measured values were consistent with the predicted calculated ones giving an accurate behaviour, with an excellent agreement with the calibration standard for further work.

Experimental Data

LECOR loop data

$Bi|Bi_2O_3$

The historical reconstruction of the oxygen sensor signal during the four experimental runs (T= 673 K, constant) is shown in ***Figure 5-11***.
In ***Figure 5-11***, , ***Figure 5-13***, the four experimental runs are plotted seperately. In the first run, before starting exposure tests, 130.8 g of Mg were added in 400 l ca. of LBE in order to guarantee the reducing conditions. In the second run, after the conditioning in the storage tank with $Ar+H_2(3\%)$. the oxygen signal stands near 500±100 mV. In the third run, shows an oscillatory path near 500±30 mV, even thought there had been a plant stop. In the fourth run the oxygen concentration grew up consistently; for lowering this, a gas bubbling was performed, without success, and then Mg was added again.

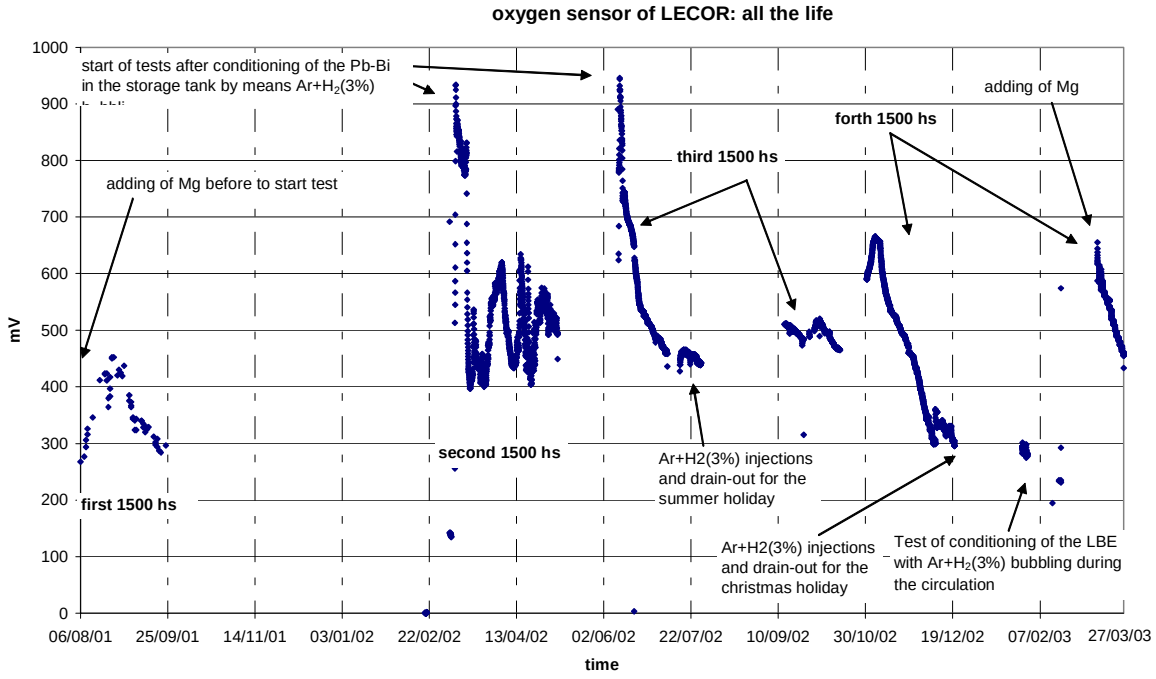

Figure 5-11: reconstruction of whole activity of LECOR sensor

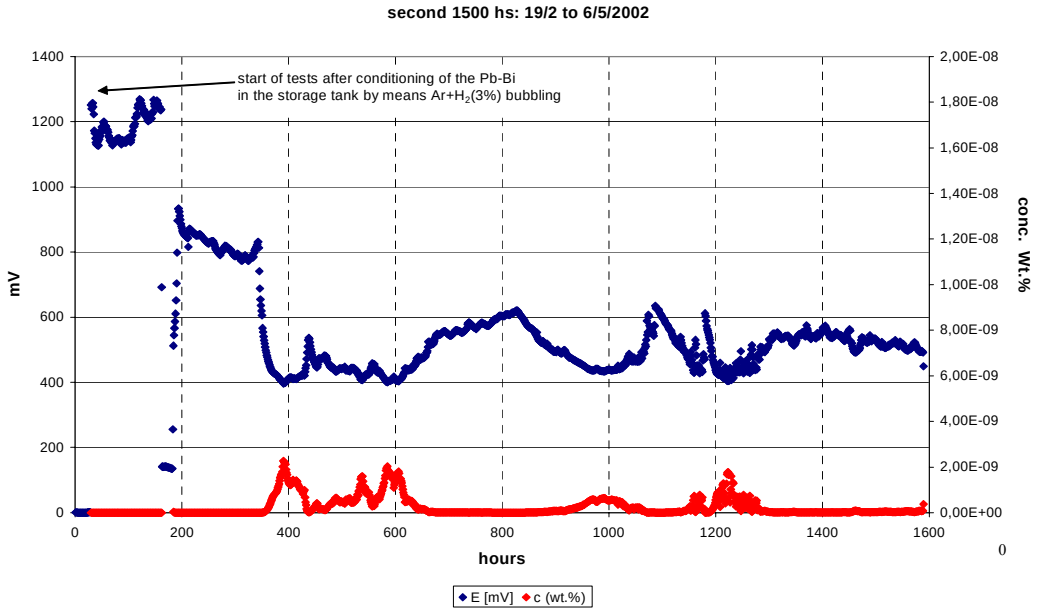

Figure 5-12: signal of LECOR sensor during the second 1500 hs of test.

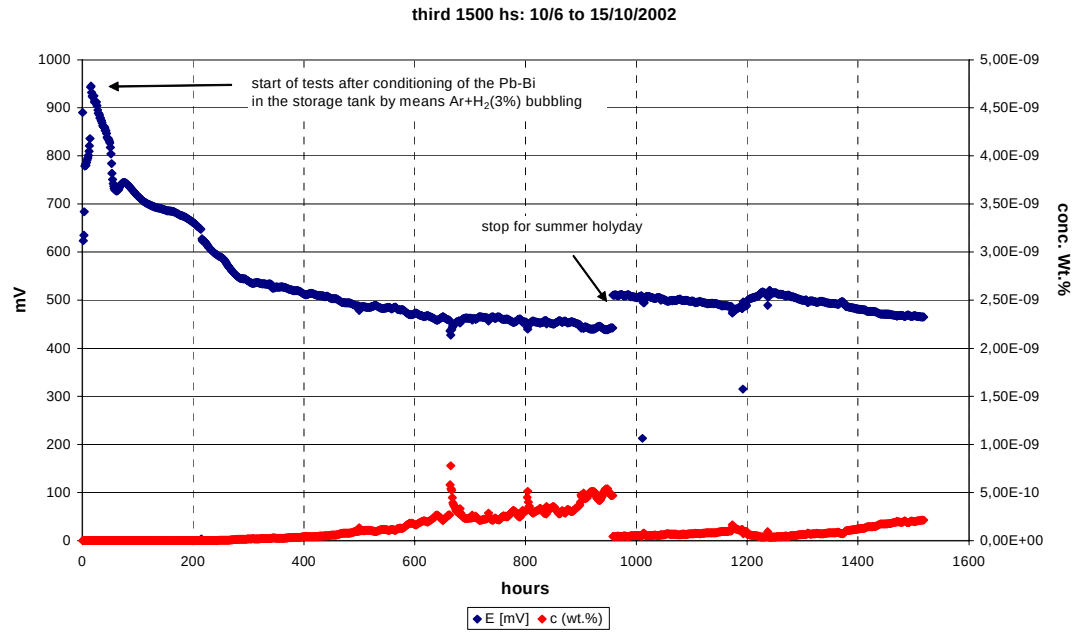

Figure 5-13: signal of LECOR sensor during the third 1500 hs of test.

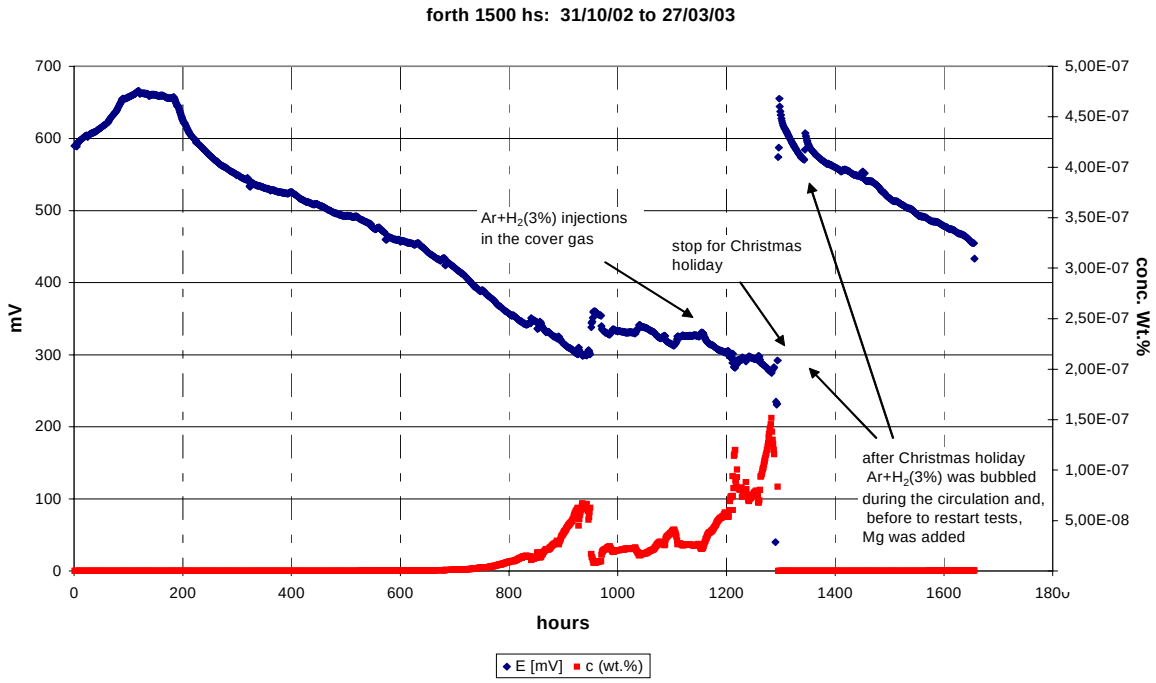

Figure 5-14: signal of LECOR sensor during the fourth 1500 hs of test

From the listed figures it is noticeable how the oxygen concentration has an oscillating behaviour. This result has to be considered excellent, being these variations very small. In particular, after the LBE conditioning the sensor signal starts from very high mV values and later lowers towards the acceptable value of 500 mV ca, indicating slightly more reducing conditions than the minimal required signal (>350 mV). An example of sensor conditioning of LBE in the storage tank is plotted in ***Figure 5-15***. The Ar+H_2(3%) is bubbled, with a flow of 200 Nl/h, till the difference of ppm values of the inlet and the outlet of the storage tank (signal of two Hygrometers) goes down and becomes constant.

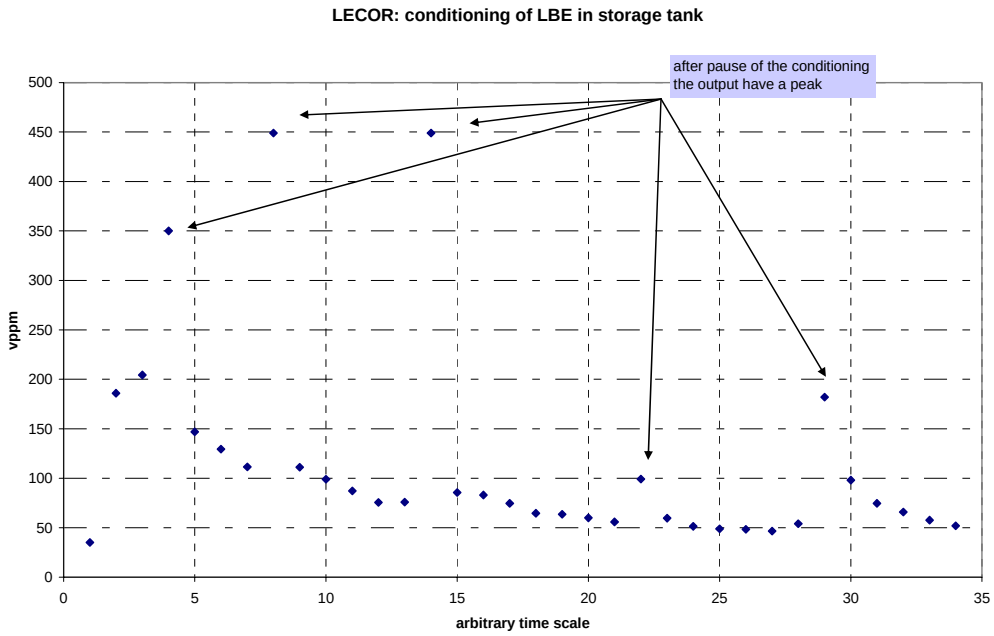

Figure 5-15: Conditioning of LBE via Bubbling of Ar-H_2 (3%) in the storage tank, with a flow of 200 Nl/h.

In|In_2O_3

After the first 1400h a historical reconstruction of its signal is possible. In ***Figure 5-16*** it is clearly visible the reducing action performed in the first days in the storage tank. When the test campaign started the injection of Ar/H_2 was stopped. In the graph ti is possible to see how the oxygen content slightly increase.
This is caused by the mass transfer between the passivated pipe walls and the reduced LBE.

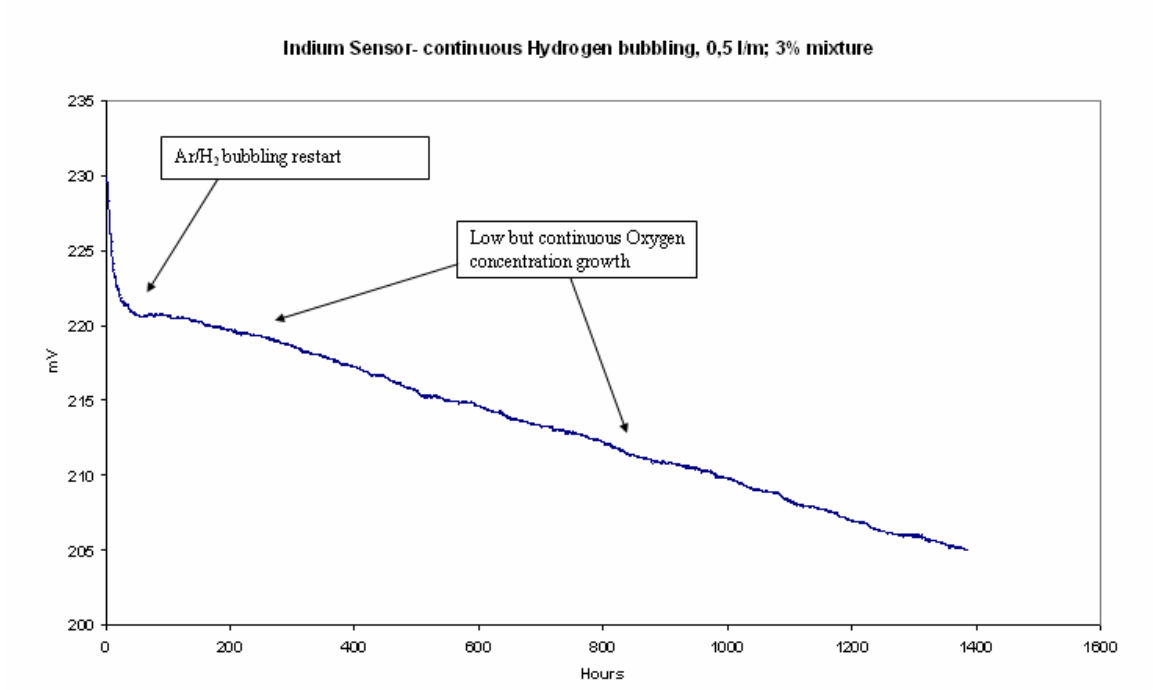

Figure 5-16: Conditioning of LBE via bubbling of Ar-H_2 (3%) in the storage tank, with a flow of 0,5 l/h.

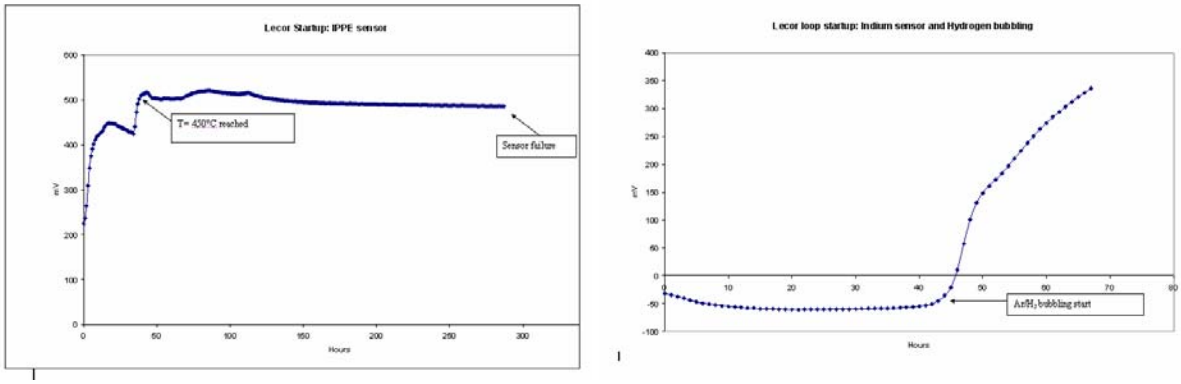

Figure 5-17: Comparison between the start up of the Russian sensor and the ENEA's one

A comparison between the behaviour of the two different sensors is shown in *Figure 5-17*.
As it can be observed the output signal is in the first case positive and it grows up to a constant value (~ 500mV). Two slopes are clearly identified. They show two Ar+H_2 bubbling series. After the first one the O_2 content increased a little, while after the second one the oxygen content remains almost constant.
The second case the signal is negative and changes to positive values due to gas bubbling.
The two sensors, with a very good agreement, show that the H_2 bubbling method is effective in order to reduce the oxygen content.

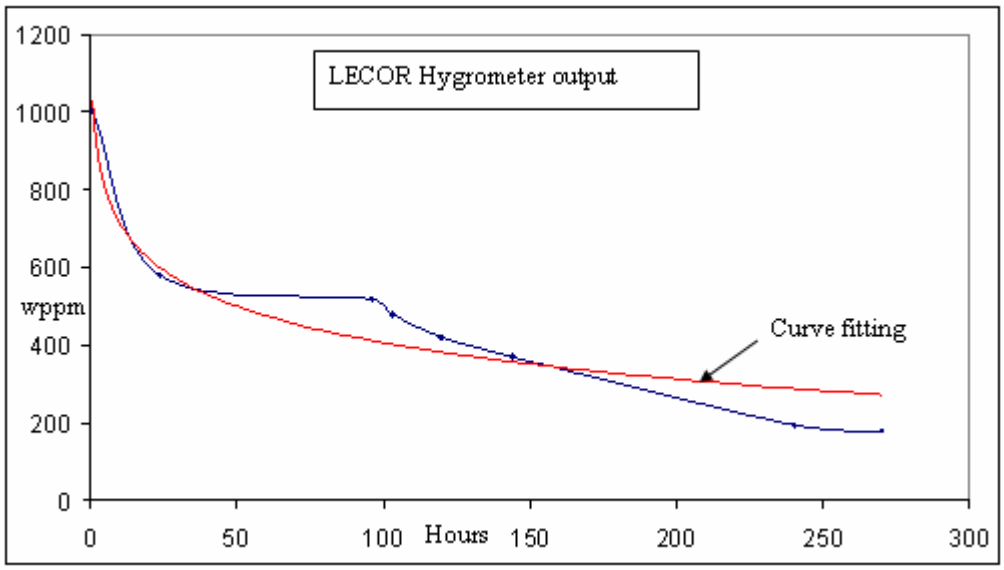

Figure 5-18: Hygrometer output

Since a hygrometer is set on the outgas of the storage tank, it was possible to record the water produced during the hydrogen bubbling.

Integration of the curve area after fitting:

$$\int_0^{270} -135{,}22 * \ln(x) + 1029{,}6 dx = 1{,}101 * 10^5$$

Corresponding to the global extraction of 445g of dissolved oxygen in the LBE.

CHEOPE III loop data

In the CEOPE III loop were performed 10000h of corrosion tests in Lead Bismuth. During the hole duration of the campaign the O_2 content was measured with a $Bi|Bi_2O_3$ sensor and recorded.
After the conclusion of the tests the loop was emptied cleaned and re filled with pure Lead, in order to start another 10000h material compatibility test with a different liquid metal.
The $Bi|Bi_2O_3$ sensor was calibrated again and its output data collected.
The historical behaviour of the signal in both cases.

$Bi|Bi_2O_3$ in LBE

The historical reconstruction of the oxygen sensor ($Bi|Bi_2O_3$) signal of CHEOPE III loop (T=673 K, constant) is shown in ***Figure 5-19***.

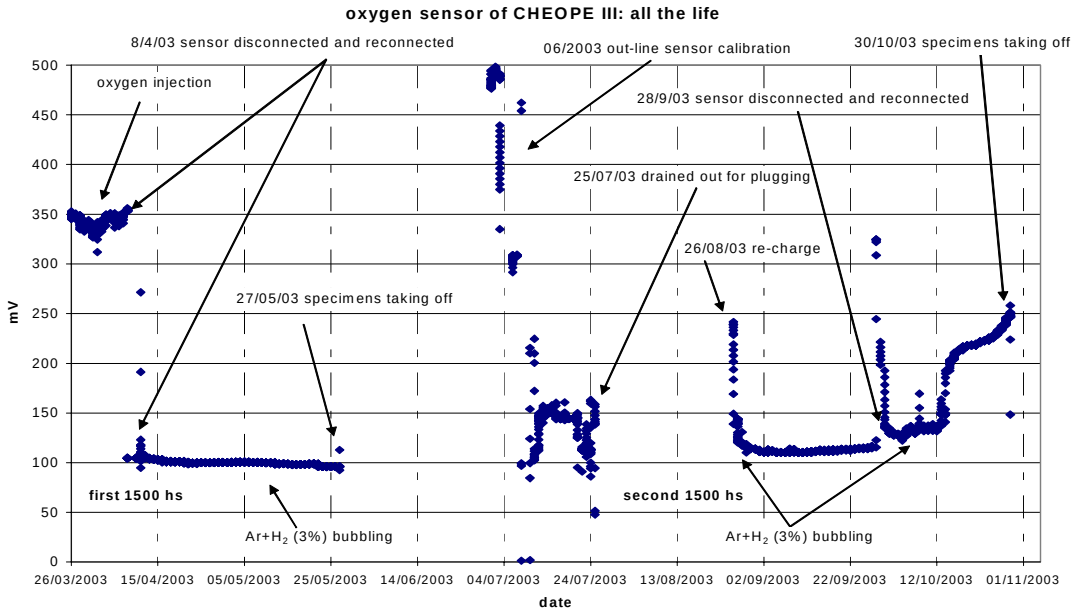

Figure 5-19: reconstruction of whole activity of CHEOPE III sensor

The operation oxygen concentration range is 10^{-5}-10^{-6} wt%, corresponding to a 150-200 mV signal ca. These conditions is very close to the saturation value for PbO (10^{-4} wt%, i.e. 76 mV ca.) and for this reason are very difficult to be exactly controlled. This could be seen comparing the two historical pictures of the two facilities: in the CHEOPE III one, plant stops and technical problems are much more frequent, where the following analyses of the impurities gave PbO as the main result. From this behaviour it is possible to infer that the sensor signal, even so near to the lead oxide saturation, is reliable.

The sensor response to the on line gas bubbling is not immediate. Some weeks are necessary to stabilize the signal, as depicted in ***Figure 5-20***, showing the sensor signal after one month while some bubbling were performed.

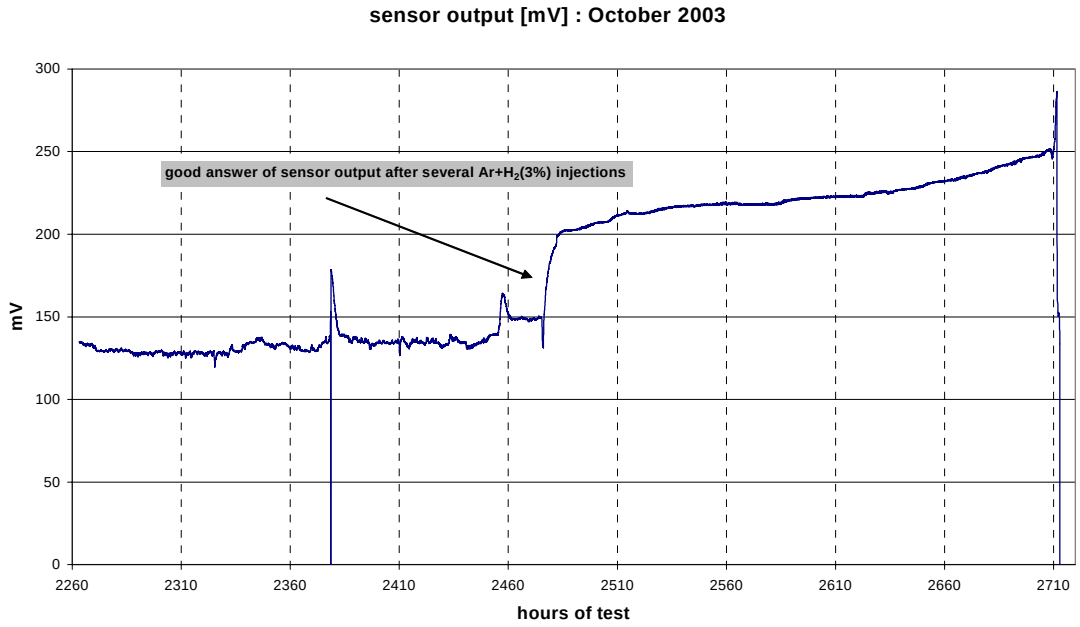

Figure 5-20: Answer of the sensor output after several gas bubblings within one month.

As summarized in ***Table 27***, flow rate variations and sensor responses are consistent. The flow rate of LBE in the LECOR loop (but this result has been considered useful also for the CHEOPE loop) was changed and the sensor output variations were recorded.

Flow rate [l/h]	E [mV]
1250	302
1350	300,4
1450	300,1
1600	298
1250	302

Table 27 : Behaviour of the oxygen sensor output with the flow rate change

These results are indeed very important, because they underline the dependency of the sensor signal from the LBE flow rate and open an interesting research field for future new sensors for large scale facilities.

Bi|Bi_2O_3 in Lead

After the conclusion of the corrosion tests in LBE, in the frame of the 6the framework programme, the PbBi was substituted with pure Lead. This in order to perform new compatibility tests.
The Bi|Bi_2O_3 sensor installed in the plant was recalibrated and set in the third test section in order to monitor the content of the oxygen dissolved in the Lead, during the tests.
In ***Figure 5-21*** the first 2000h are graphed. It is possible to see that during the first 500h the oxygen dissolved increased and how it decreased after the injection on Ar/H_2. The gas mixture was bubbled for 10^5 minutes at a flow rate of 0,5 l/min. When the bubbling of the mixed gas was suspended the oxygen content increased.

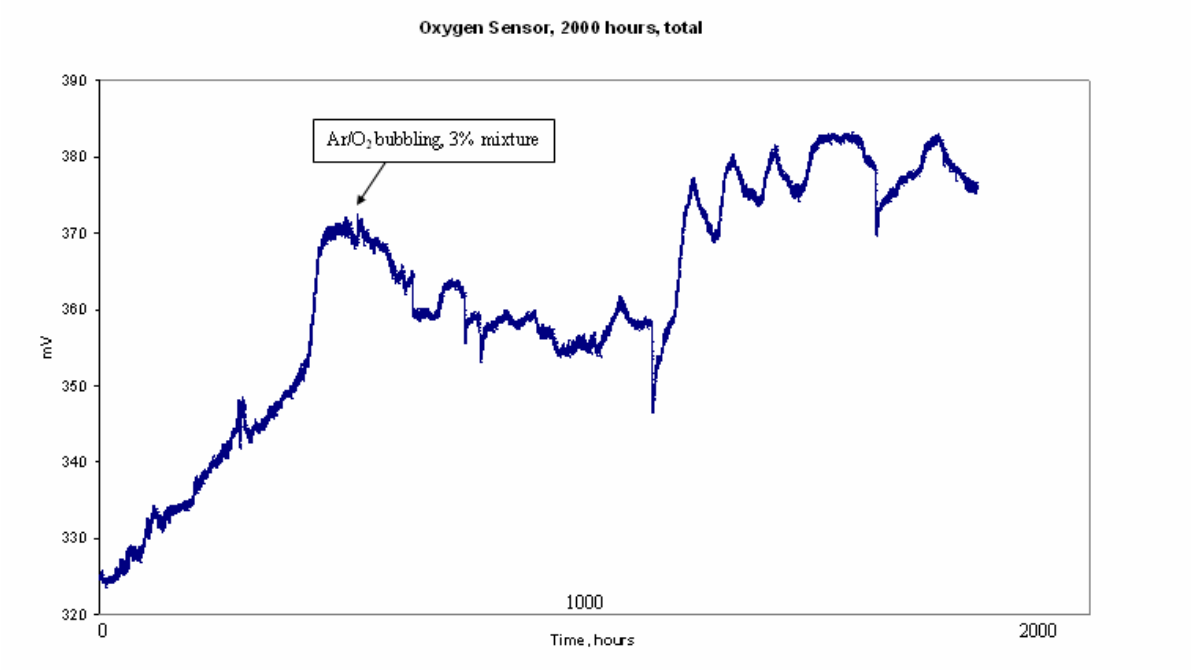

Figure 5-21: Cheope III sensor historical outcome signal

It is possible to graph also the start up of the facility. During the first seconds the signal oscillates then after the pump started to work it grows up to 300mV. The signal becomes constant when the loop reaches the test temperature.

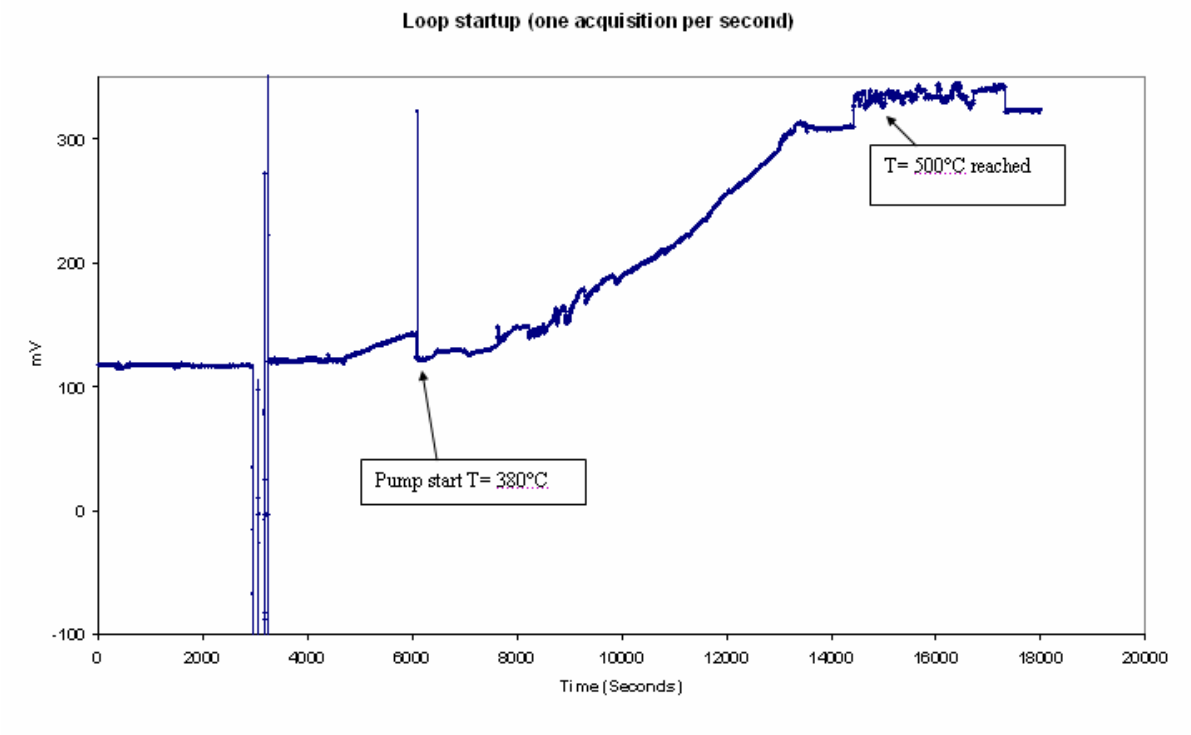

Figure 5-22: Cheope III start up

Conclusions

In PbBi, the two $Bi|Bi_2O_3$ sensors gave signals which were in good accordance with the theoretical ones in both plants. Also the $In|In_2O_3$ sensor gave outcome signals coherent with the theoretical data.
Moreover the two sensors gave coherent signals in similar working conditions, allowing to start the design of a sensor for a pool configuration.
That leaded to the design and construction of an oxygen sensor adapt to pure Lead. In this case it was a technological innovation since, up to now, few data are available. The $Bi|Bi_2O_3$ sensor was recalibrated in pure lead and showed a behaviour comparable to the one in PbBi.
Only the magnitude of the outcome signal is slightly lower than in the LBE case.
The next step is to design and construct an oxygen sensor for a pool type reactor. This sensor will be tested in the frame of experimental campaigns, which will be performed in the CIRCE facility next year.
For the new "pool" sensor some obstacles should be overcome, such as the higher pressure filed, the temperature variations and the insulation of the electrical cables.
As a matter of fact, in order to monitor the oxygen content in a pool deep nine meters, it is necessary to install some sensors.
Due to the different deepness they are loaded differently along their length and this can affect the ceramic glove. Moreover the temperature gradient along the pool affect both the ceramic and the electrical cables with the possibility to break the sensor.

Bibliografy

[1] Asher R. C.; Harper D. C.; Kirstein T. B. A.; Leach F.; Taylor R. G. (1988): "Recent developments in the design, performance and application of HARWELL oxygen sensors and Harwell carbon meters", 4th international conference on liquid metal engineering and technology (LIMET), 17-21 Oct., Avignon-France.

[2] Askhadullin R.S.; Martynov P. N. et al (2005): "Development of oxygen sensors, systems of control of oxygen content in lead coolants for test loops and facilities", International Science and Technology Centre contract n°3020.

[3] Askhadullin R.S.; Martynov P. N.; Simakov A. A.; Emepiantseva Z. I.; Sisoev O. M.; Lanskikh V.S.; Gulevskiy V.A; Chernov M. E. (2003): "Regulation of the thermodynamic activity of oxygen in lead and lead-bismuth by the dissolution of the oxides in heat transfer systems", proceedings of the Fast Neutrons Reactors conference, Dec 8-12, Obninsk, Russian Federation (in Russian).

[4] M. Azzati, A. Gessi, G. Benamati (2003): "Experimental results on oxygen control systems - TECLA D28", ENEA FIS ENG Technical Note, December 5th.

[5] Chernov M. E.; Martynov P. N.; Gulevskiy V. A. (2003): "Development of electrochemical capsule oxygen sensor for control and monitoring of heavy metal coolant condition", Proceedings of the fast neutrons reactors conference, Dec 8-12, Obninsk, Russian federation (in Russian).

[6] Colominas S.; Abella J.; Victori L (2004): "Characterisation of an oxygen sensor based on In/In2O3 reference electrode", Journal of Nuclear Materials, Vol. 335, pp 260-263.

[7] Courouau J-L (2000): "Oxygen control systems, comparison between oxygen probes", Proceeding of the 1st MEGAPIE Technical Review Meeting, Cadarache-France, 14-15 June.

[8] Courouau J-L.; Deloffre P.; Adriano R. (2002b): "Oxygen control in lead-bismuth eutectic: first validation of electrochemical oxygen sensor in static conditions", Journal de Physique IV, France 12, Pr8, pp 141-153.

[9] Courouau J-L. (2003a): "Impurities and purification processes in Lead-Bismuth systems. TECLA deliverable n°25", CEA Technical note DER/STR/LCEP 03/001.

[10] Courouau J-L.; Pignoly L.; Delisle C.; Deloffre P.; Balbaud F. (2003b): "Report on the long term validation of electrochemical sensor: TECLA Deliverable n°32", CEA technical note DER/STR/LCEP 03/031.

[11] Courouau J-L. (2004a): "Electrochemical oxygen sensors for on-line monitoring in lead–bismuth alloys: status of development", Journal of Nuclear Materials, Vol. 335, pp 254-259.

[12] Courouau J-L.; Sellier S.; Chabert C.; Pignoly L. (2005b):

[13] "Electrochemical oxygen sensor for on-line measurement in liquid lead alloys systems at relatively low temperature", to be issued in AFINIDAD, journal of theoretical and applied chemistry, chemistry institute de Sarria (IQS), Barcelonna, Spain. "Electrochemical Sensor. The Calibration and Control", D. Emerenkov. Private paper..

[14] FAZIO C.; AZZATI M.; BENAMATI G. (2000): "Oxygen control strategies in large loop, critical analysis of the different process", ENEA FIS ENG Technical Note HS-A-R—007.

[15] Fernandez J. A.; Abella J.; Barcelo J.; Victori (2002): "Development of an oxygen sensor for molten 44.5% lead_55.5% bismuth alloy", Journal of Nuclear Materials, Vol. 301, pp 47-52.

[16] Ghetta V.; Fouletier J.; Henault M.; Le Moulec A. (2002): "Control and monitoring of oxygen content in molten metals, application to lead and lead-bismuth melts", Journal de Physique IV, France 12, Pr8 123-140.

[17] Gromov B. F.; Shmatko B.A. (1997), Izvestiya Vischikh Uchebnikh Zavedenii – iyadernïï energiya (transaction of higher educational institutions – nuclear energy), N6, pp14-18 (in Russian).
[18] Gromov B. F.; Orlov Y. I.; Martynov P. N.; Gulevskiy V. A. (1998):" the problems of technology of the heavy liquid metal coolants (lead-bismuth, lead)", Proceedings of the conference of the Heavy Liquid Metal Coolants in Nuclear Technology, Obninsk, Russian Federation, October 5-9, pp 87-100.
[19] Konys J.; Muescher H.; Voß Z.; Wedemeyer O. (2001); "Development of oxygen meters for the use in lead-bismuth", Journal of Nuclear Materials, Vol. 296, pp 289–294.
[20] Konys J.; Muescher H.; Voss Z.; Wedemeyer O. (2004)): "Oxygen measurements in stagnant lead–bismuth eutectic using electrochemical sensors", Journal of Nuclear Materials, Vol. 335, pp 249-253.
[21] Korotkov V. V.; Ivanov K.D.; Salayev S. V. (2003): "The results of the experimental investigations using IPPE test facilities in support of the technological regimes of maintaining the lead coolant quality and the purity of self contained BOR-60 reactor channel", proceedings of the Fast Neutrons Reactors conference, Dec 8-12, Obninsk, Russian Federation (in Russian).
[22] Li N. (2003), in advanced fuel cycle initiative, Quarterly report, Vol. 1, Jan-Mar 2003, Sand2003-2060P.
[23] Muescher H.; Konys J.; Voß Z.; Wedemeyer O. (2001): "Measurement of oxygen activity in lead bismuth eutectic by means of the EMF method", FZKA Report 6690, January 2001.
[24] Ricapito I.; Fazio C.; Benamati G. (2002): "Preliminaries studies on PbO reduction in liquid LBE by flowing hydrogen", Journal of Nuclear Materials, Vol. 301, pp 60-63.
[25] Shmatko B.A.; Rusanov A.E. (2000): "Oxide protection of materials in melts of lead and bismuth", Materials Science, vol.36, N°5, pp.689-700.
[26] Subbarao E. C. (1980): "Solid electrolyte and their applications", Plenum press.
[27] Takahashi M.; Sekimoto H. et al. (2002): "Experimental studies on flow technology and steel corrosion of lead-bismuth", Proceedings of ICONE 1O, n°22226, Arlington, Virginia USA.
[28] Zrodnikov A.V.; Efanov A.D.; Orlov Y.I.; Martynov P.N.; Gulevskiy V.A.; V.M. Troyanov V.M. Rusanov A.E. (2003):" Heavy liquid metal coolants technology (Pb-Bi and Pb)", 3rd International Workshop on Materials for Hybrid Reactors and related Technologies, Rome, October 2003.
[29] FZK Internal comunication - 2001

6. Nak sensors production

Abstract

The use of liquid metals for an industrial application is presented. In particular, the use of the sodium-potassium alloy for pressure transducer applications.

A collaboration with GEFRAN S.p.A. started during the spring of 2005, aimed to investigate the possibility to use the NaK alloy as filling fluid for pressure transducer. Gefran is a leader company in the field of systems and components for automation of industrial processes, and was interested to improve its capability in offer high temperature pressure transducers for "melt" applications. Moreover, the production of sensors Hg free is considered strategic by Gefran, due to the RoSH directive (2002/95/CE).

Within this collaboration, the compatibility of the NaK alloy with the existing industrial manufacturing process has been evaluated; then, a suitable filling process has been developed and a dedicated small facility has been designed and realised.

The qualification campaign performed on the sensors manufactured indicates as the objective of produce NaK pressure transducers of high quality has been achieved.

Intoduction

One of the main issue in high temperature pressure measurement is the necessity to maintain at relative low temperature the sensible element of the measurement instruments. One of the possible solution to this problem is to use a transmission media able to transfer the pressure signal from the high temperature environment to the sensible element, kept in a lower temperature environment.
On this base, pressure transducers filled with a transmission liquid have been developed from a long time. Typically, the most popular filling fluid is mercury, accomplishing the task with very good performance. Oils are often used too with good results, even if the performance are lower then in the case of Mercury.

However, both mercury and oil suffer in the case of measurement environment temperatures higher than 300 °C. In fact, sensors filled with mercury can't overcome 300°C due to the Hg low boiling temperature, while oils (suitable for filling scopes) undergo to thermal dissociation phenomena.
For this reason, the possibility to use a different filling media able to work at higher temperatures was considered of interest by Gefran S.p.A.

Moreover, the 2002/95/CE Directive (RoSH directive), concerning the use of dangerous products in the electric and electronic equipments, states that Mercury should be abandoned, due to its proven pollution effect on the environment.
So, the capability to offer high standards pressure sensors Mercury free was considered strategic by the Company.

The eutectic 22sodium-78potassium alloy, NaK, is a reliable alternative to Mercury. In fact, its thermo-physical properties indicates a good attitude to the task of pressure transmission media in a wide range of temperatures. However, NaK alloy is a very reactive liquid, so that its use in an industrial process is more complex than in the case of other fluids.

In 2005 Gefran was owner of a well tested filling process developed for oil and Mercury and consolidate in a long time of experience. On the other hand, this process could not simply transferred to the case of NaK alloy, due to safety reasons.

The work performed in collaboration with Gefran was aimed to verify the possibility to use NaK in an industrial manufacturing process as close as possible to its standard process, to design a prototypical facility and to manufacture it, in order to start with a new industrial production of NaK filled pressure sensors. All these objectives have been successfully reached.

NaK thermo-physical properties

Introduction

The NaK alloy was extensively studied in the past in the field of nuclear power plants as possible coolant. Thus, its thermo-physical properties are well known in a wide range of temperature. With reference to its use as filling fluid, it was important to know several of those properties to understand its behaviour both in terms of process as well as in terms of performances. For instance, the viscosity, the vapour pressure and the density of the alloy will affect mainly the process, while its compressibility and thermal expansion attitude will affect the performance of the sensor. Then, a review of NaK properties, focused on those which could affect both the production process and the working behaviour, has been carried out, as far as a comparison with the same properties of other filling fluids.
Moreover, in order to design properly the facility and to choice the suitable materials to be used, a literature research concerning the NaK compatibility with other materials has been performed too.

NaK: chemical physical proprieties

The NaK eutectic alloy is a silver metallic colour odourless liquid under normal conditions (1 bar, 20°C).
In Figure 6-1 is represented the phase diagram of the Na-K binary system[14]. Sodium (Na) and Potassium (K) elements are miscible in every percentage. Their alloy presents the eutectic point for when the Na and the K rich the 22% and the 78% each. According to the diagram, its freezing point is -12.5 °C at 1 bar, while its boiling temperature is 785°C, so that the alloy exist under liquid state in the usual range of temperature for melt pressure sensors (20 – 500).

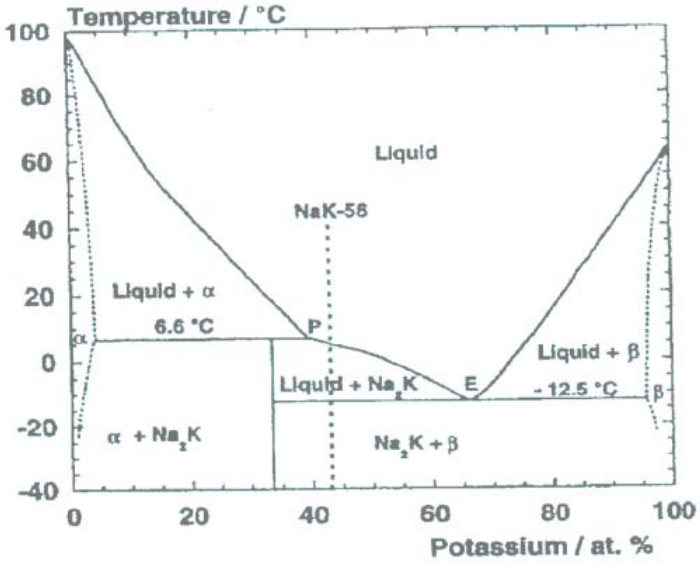

Figure 6-1 – Phase diagram of the NaK alloy

Density[8][11]

At room conditions (20 °C, 1 atm) the NaK alloy shows a density a bit lower than water (0.866 g/cc). As for others liquid metals the evolution of the density with temperature is linear, decreasing when temperature increases. In Figure 6-2 the NaK density is compared to the density of its compounds.

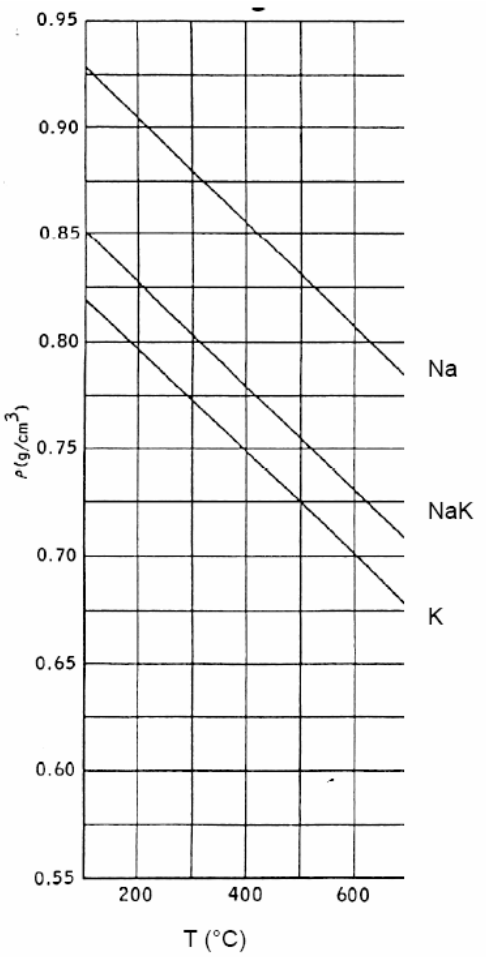

Figure 6-2 – Density of the NaK alloy compared to its compounds in the range 100 – 700 °C

In figure 3 the NaK density is compared to the density of the Mercury as well as of the oil used by Gefran as filling fluid. As can be seen, NaK shows a density very close to the Oil ones in the whole considered range of temperature, while the mercury is one order of magnitude heavier than both.

Viscosity[8][11]

At room conditions the NaK alloy shows a viscosity of about 0.74 cP, lower than water, characterized by a trend slightly decreasing with the temperature (0.5 cP at 100°C); moreover, among the three liquids considered it presents the lowest viscosity. In Figure 6-4 the viscosity of NaK as well as its compounds is displayed, while in Figure 6-5 the viscosities of NaK, mercury and oil are compared between 10 to 100 °C. Note as the difference between NaK and oil is much more important around the room conditions, that are the typical process conditions.

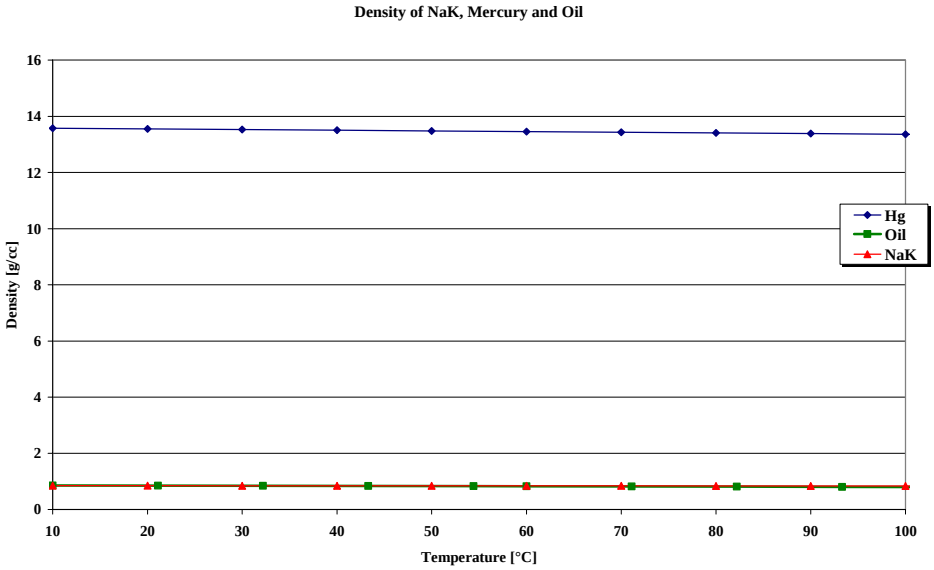

Figure 6-3 – Comparison between the densities of NaK, Mercury and Oil in the range 10 – 100 °C

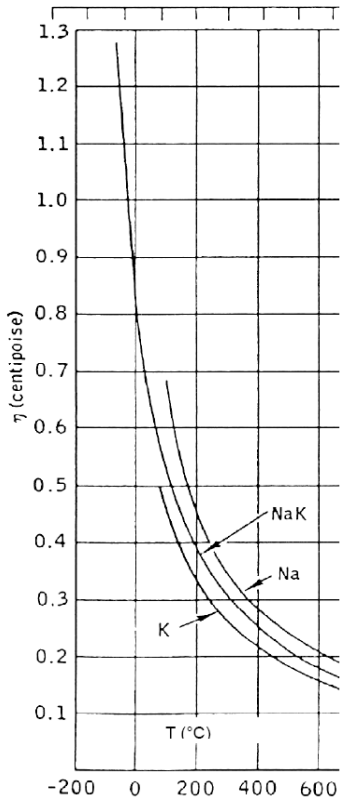

Figure 6-4 – Dynamic viscosity of the NaK alloy and its compounds.

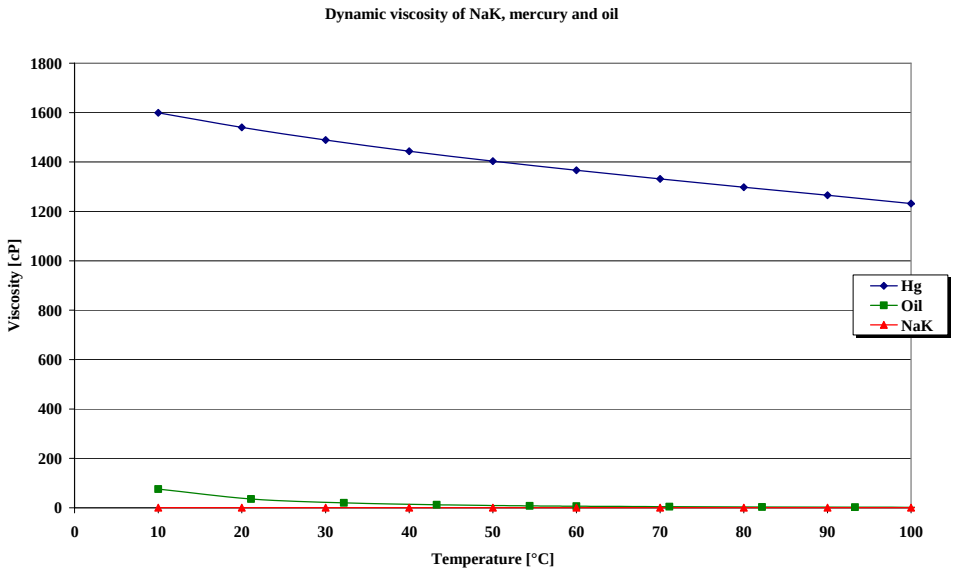

Figure 6-5 – Dynamic viscosity of the NaK, mercury and oil between 10 and 100°C.

Vapour pressure [16][17]

Equation (1) gives the vapour pressure of the NaK alloy as function of the temperature. In figure 2 the evolution of the alloy vapour pressure with temperature is compared to the ones of its compounds.

$$\log p_{atm} = 4.111 - {}^{4367}\!/_{T(K)} \qquad (1)$$

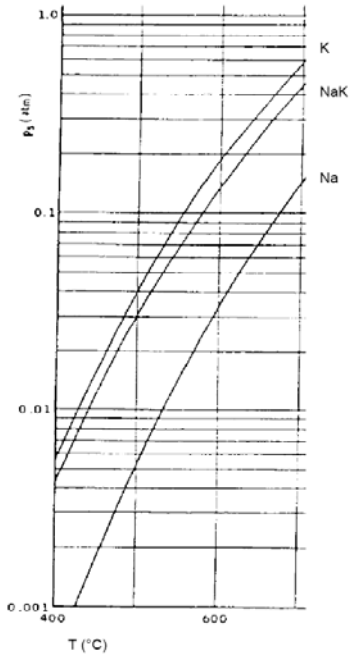

Figure 6-6 – Vapour pressure of the NaK alloy compared to its compounds in the range 400 – 700 °C

With reference to the mercury, the vapour pressure of the NaK alloy is lower at each temperature. This parameter is important for the process as far as the alloy shall be exposed to very low pressures (order of few mTorr).

Specific heat and thermal conductivity [16][17]

Even if these two properties are less important than the others for the process, for compliance the comparison between the specific heat and the thermal conductivity of the alloy and its compounds is shown in figure

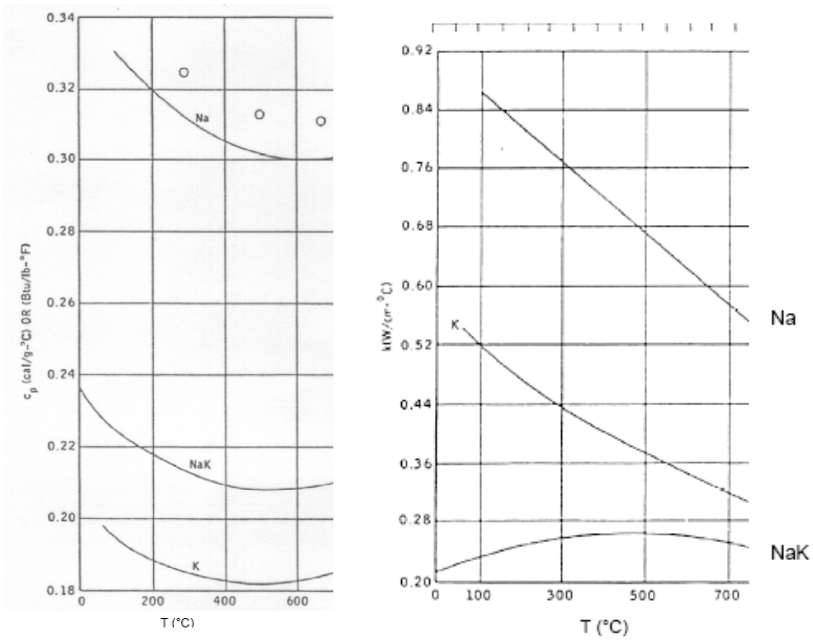

Figure 6-7 – Heat and thermal conductivity

Other properties [18][19][20]

Two other properties are worth of consideration: the surface energy and the isothermal compressibility. In terms of process, another the surface energy of the alloy is an important property to take in account, being its wettability strictly connected to it. In general, an high surface energy indicates that the liquid will show a low wettability; this could produce a higher difficulty in the filling process of the capillary. Even if few data have been found in literature about this property, the NaK alloy show a surface energy quite constant and close to 0.1N/m up to 100 °C; compared to the mercury at room temperature, this value is quite five times lower, being the surface energy of the mercury about 0.48 N/m. This suggests that the filling process could be easier in the case of the NaK alloy, since other conditions remain the same. On the other hand, the mercury is advantaged by its higher density, since the process is based on a "gravimetric fall" inside the capillary

Concerning the isothermal compressibility, this properties is important in terms of performance of the sensor. In fact, note as the ideal filling fluid is perfectly incompressible. Unfortunately, the data available in literature are spare. At 100°C, the isothermal compressibility of the NaK alloy is about $35*10^{-11}$ m^2/N (higher than mercury but lower than the Oil). This suggests that the behaviour of a NaK sensor should lie between the behaviour of the sensors filled by the two other fluids

NaK compatibility with the materials

The compatibility of the NaK alloy has been studied in order to identify the correct materials to be used in the construction of the plant.

Thus, the research was focused on the behaviour of the liquid metal with both inorganic (structural alloys, air and water) and organic elements.

Behaviour towards the structural materials

In the Table 6-1 the solubility of some elements is listed. The solubility is given at 400°C in weight part pre millions.

Elemento	Solubilità a 400°C in Wppm
Fe	0.04
Cr	9×10^{-5}
Ni	0.55
V	-
Ti	-
Al	24.2

Table 6-1 – Metallic elements solubility in NaK

From 400°C up to 430°C (Figure 6-8) the solubility of both Fe and Cr is negligible and also Ni solubility is very low (~1 wppm), even if its actual value is higher then the others.

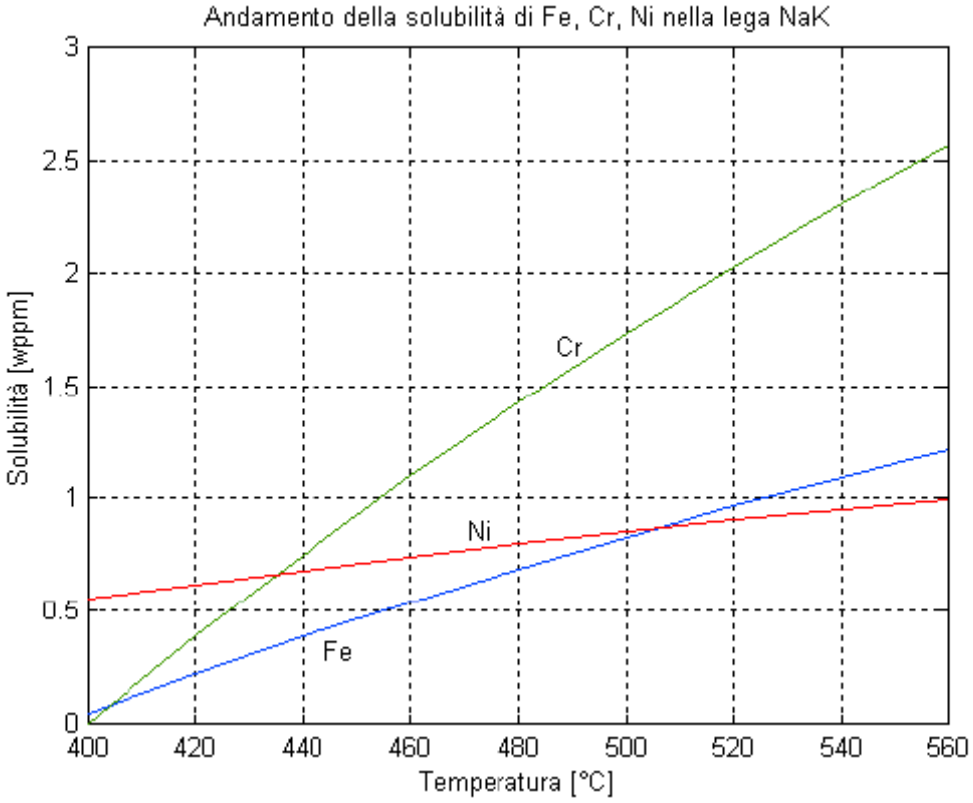

Figure 6-8 – Solubility trend of Fe, Ni and Cr

Corrosion phenomena can eventually lead to the formation of a thin ferrite layer on the surface.

NaK reactivity with water and oxygen

The Ellingham – Richardson diagram describes the Gibbs free energy curves characteristic of the formation of oxides due to the reaction between NaK end Oxygen[8].

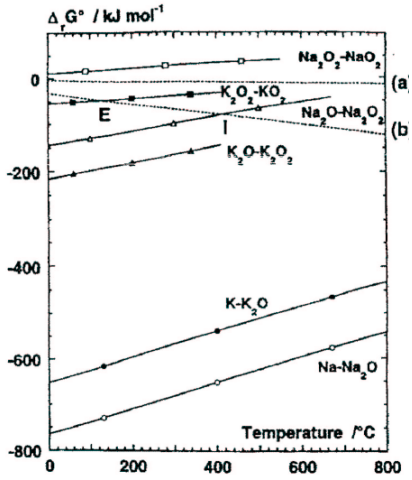

Figure 6-9 – Ellingham – Richardson diagram

Here below are listed some of the most common reactions between NaK (in its two components Sodium and Potsssium) and the oxygen dissolved in the alloy[8].

$4Na + O_{2(g)} = 2Na_2O_{(s)}$ $\Delta G^0 298 = -758$ KJ/mol

$2Na_2O + O_{2(g)} = 2Na_2O_{2(s)}$ $\Delta G^0 298 = -141$ KJ/mol

$4K + O_{2(g)} = 2K_2O_{(s)}$ $\Delta G^0 298 = -646$ KJ/mol

$2K_2O + O_{2(g)} = 2K_2O_{2(s)}$ $\Delta G^0 298 = -211$ KJ/mol

$K_2O_2 + O_{2(g)} = 2KO_{2(s)}$ $\Delta G^0 298 = -53$ KJ/mol

All these reactions (the kinetic formation of the superoxides, the thermo dynamic formation of the oxides and the DISPROPORZIONE) are strongly exothermic.
The reaction with the water vapour is preferred due to the stronger hygroscopic behaviour of the oxides layers. An example of such a kind of reaction is:

$Na_2O_2 + 8H_2O = Na_2O_2*8H_2O_{(s)}$ $\Delta G^0 298 = -193$ KJ/mol

All the products are solid below the 130°C. They look like a thick yellow-grey crust laying on the surface of the liquid metal.
Usually it is formed by a thin layer of K_2O and Na_2O and of a second higher layer formed by Na_2O_2 and KO_2. The first thinner layer is in direct contact with the metal surface. Even if the crust density is higher then the NaK one, it float on the surface due to its porous nature. Thank to the porosity, the wettability between the oxides crust and the liquid metal is very low.
If the crust breaks and the external layer reaches the alloy, it reacts strongly with it. The reduction of the peroxides and of the hydrate compounds driven by the NaK is strongly exothermic and it could, also, generates explosions.
Here below are listed some of those reactions:

$2KO_{2(s)} + 2K_{(l)} = 2K_2O_{(s)} + O_{2(g)}$ $\Delta G^0 298 = -164$ KJ/mol

$2KO_{2(s)} + 2Na_{(l)} = K_2O_{(s)} + Na_2O_{(s)} + O_{2(g)}$ $\Delta G^0 298 = -220$ KJ/mol

$$Na_2O_2*8H_2O_{(s)}+8Na_{(l)}= Na_2O_{2(s)}+ 8NaOH_{(s)}+ 4H_{2(g)} \qquad \Delta G^0298= -1000\ KJ/mol$$

$$NaOH*H_2O_{(s)}+ Na_{(l)}+ 2NaOH_{(s)}+ 1/2\ H_{2(g)} \qquad \Delta G^0298= -132\ KJ/mol$$

$$KOH*H_2O_{(s)}+K_{(l)}= 2KOH_{(s)}+ 1/2\ H_{2(g)} \qquad \Delta G^0298= -130\ KJ/mol$$

The heat freed by these reactions is capable to ignite and to explode the gaseous H_2 and O_2.
Another reaction which could cause an explosion is the one between the NaK alloy and the Sodium peroxide multi-hydrate, which reaction chain is described here below:

$$NaK_{(l)}+Na_2O_2*2H_2O_{(s)}=NaOH_{(s)}+KOH_{(s)}+ Na_2O_{2(s)}+H_{2(g)} \qquad \Delta G^0298= -242\ KJ/mol$$

$$Na_2O_{2(s)}+H_{2(g)}= 2NaOH_{(s)} \qquad \Delta G^0298= -339\ KJ/mol$$

$$2Na_2O_2*2H_2O_{(s)}= 4NaOH_{(s)}+2H_2O_{(g)}+O_{2(g)} \qquad \Delta G^0298= -33\ KJ/mol$$

$$2H_{2(g)}+ O_{2(g)}= 2H_2O_{(g)} \qquad \Delta G^0298= -483\ KJ/mol$$

These reactions are simultaneous and strong exothermic and potentially explosive.

NaK reactivity with organic compounds

The reactivity of the alkali metals with the Carbon (C) compounds is remarkable. The value of this activity is related to the ionic character of each metal. The higher is this characteristic the higher will be their reactivity.
In the Table 6-2 Table 6-2 – Ionic percentuage behaviour of alkali metalsis reported the ionicity (in %) of each alkali element[14].

Metallo	*K*	*Na*	*Li*	*Mg*	*Zn*	*Cd*
Carattere ionico %	51	47	43	35	18	15

Table 6-2 – Ionic percentuage behaviour of alkali metals

It is evident that both Sodium and Potassium are the most reactive among all.
The alkali metals are used often in the organic synthesis, as compounds of the intermediate reactive elements.
Moreover the Na and K compounds react also with the ether elements through a nucleon substitution[13][15][16].

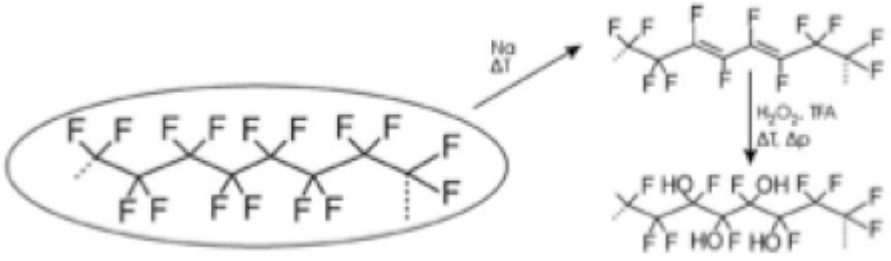

Figure 6-10– Chain reaction of the NA and TEFLON®

Both Sodium and Potassium (and, of course, their eutectic alloy) show a big reaction rate also with the halogenates as well as the fluorites (such as TEFLON®) compounds. In Figure 6-10 the chain reaction between Na and TEFLON® is shown.
As a matter of fact these materials have a very low activation energy. For instance NaK and TEFLON® start to react at room temperature already. Since it is strongly exothermic the temperature increase quickly since the reactions becomes quantitative at 120°C and the polymer loses its characteristic.

NaK sensors industrial manufacturing and qualification

Description of the filling facility

The facility consists of different units and systems integrated one to each other, each one aimed to different scopes. Following a schematic description, four main units can be recognised (see Figure 6-11):

- The Storage Unit (SU)
- The Handling Unit (HU)
- The Vacuum Unit (VU)
- The Filling Unit (FU)

All these units consist of transfer lines, vessels and valves, and are equipped by standard instrumentation to measure the process variables, such as temperature, pressure and levels. Auxiliary systems, such as a heating system and a safety pressure relief system, serve the facility. Moreover, the HU is connected to a pressurised gas distribution line by an Electronic Pressure Regulator Valve (EPRV).
The Data Acquisition System, collecting the data from the installed instrumentation, and the Monitoring and Control System (MCS) based on a process software developed in Lab View 8.0, allow to operate safely the facility in an almost automatic way.

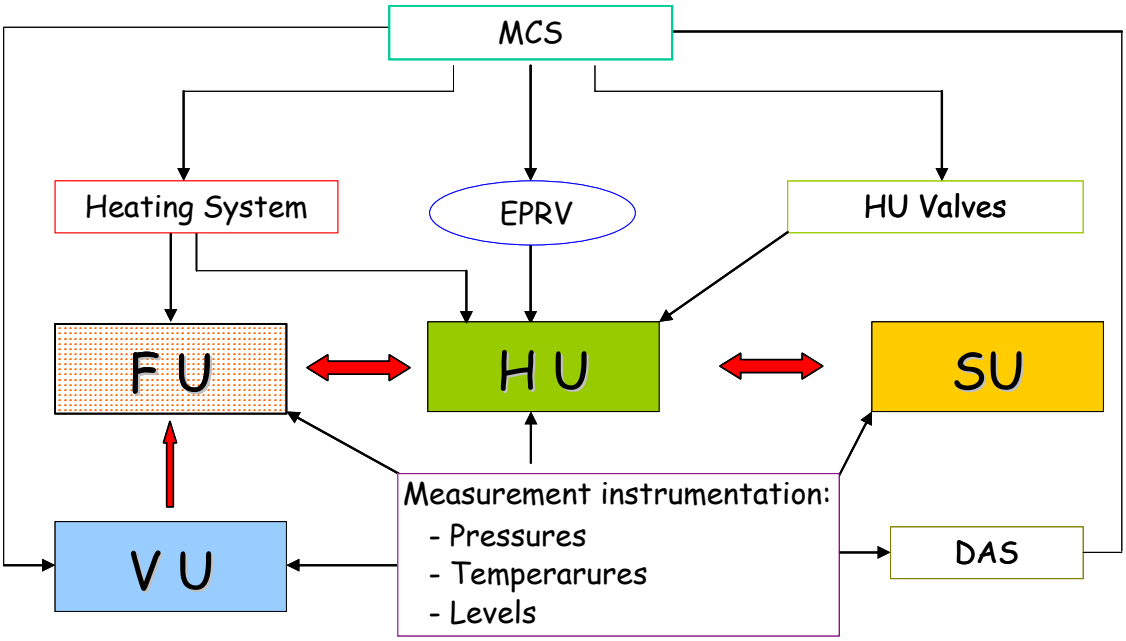

Figure 6-11 – Flow chart of the operational procedure of the facility

For example, since the transfer of the liquid metal from the SU to the HU is required, the MCS allow a proper pressurization of the storage vessel contained in the SU acting on the EPRV as well as on the valves of the HU. When the DAS indicates that the desired level in the vessel of the HU is reached, the MCS breaks the pressurization, insulates the HU vessel and acts on the valves in order to release the overpressure from the storage vessel. However, in several steps of the process the user must accomplish particular operation manually; for example, the load of the sensors to be processed on the Filling Unit, as well as their download when the process is completed. Moreover, at the beginning of each new operative phase, the confirmation to proceed is required to the user by the software. In this way, the user is able to follow the process step by step, checking the key variables during the filling of the sensors.

Except of for the control PC where the software is installed, the FU is the only interface between the user and the facility during the operative process. It consists of a battery of several “filling line”, each one equivalent to the others, connected to a collector supplied both by the HU and the VU. The interface with the user is realised by a glove box, where the filling lines end. Each one of these in its terminal part is equipped by a suitable union able to insert and safely connect the feeding capillary pipe of the sensors to the process. The sensors have to be inserted in their housing (ref Figure 6-12)inside the glove box and connected to the filling lines. When the process is ended and the FU is completely vented by the liquid metal, the user downloads the sensors from the glove box.

Figure 6-12 - Pertucular of the connection between the feeding pipe and the sensor capillar

Description of the filling process

As already described, the facility can be conceptually divided in two parts, the first devoted to the safe containment and handling of the liquid metal, the second dedicated to the filling process. However, these two parts interacts strictly during the process. In the following a general description of the most important operative steps is reported.

Assuming to follow the facility during a cycle of normal operations, six important steps can be highlighted:

- transfer of the liquid metal from the SU to the HU;
- load of the sensors to be filled inside the FU;
- evacuation of the FU by means of the VU;
- feeding of the FU by the HU and filling of the sensors;
- draining of the liquid metal to the SU and venting of the FU;
- download of the filled sensors from the facility.

During the first of these phases, the NaK alloy is moved from the SU to the surge vessel of the handling unit. Here the liquid metal is maintained, its temperature and level monitored as well as the pressure of the cover gas.

After this, the MCS ask the user to load the sensors in their proper housing inside the FU; during this span, the MCS disable the manual control of several systems, such as the insulating valves of the HU and the vacuum pump of the VU, in order to avoid any incorrect activation by the user.
Then, the user gives his confirmation to proceed.

Once the sensors are properly connected to the feeding lines, the glove box is closed and the process continues with the evacuation of the sensor capillary; to perform this, the MCS activate the VU and

operate its insulation valves in order to evacuate the FU. After a short transient, the pressure in the system fall to few mTorr. However, it is necessary to maintain this low level of pressure in the system for some hours, since the capillaries offer a strong resistance to the evacuation.

This phase is of critical importance for the process: a good quality of the void in the capillaries is one of the most important parameters to obtain a good filling and then a good sensor. On the other hand, a loss of integrity of the system during this phase could result in an accident, since air could be sucked inside the lines of the system. In this case, the liquid metal could be accidentally exposed to a mixture of air and humidity, so exothermal reactions could occur.

During this phase the MCS monitors the pressure in the interested units by a "vacuum meter"; Once a steady level of pressure is reached (below to a set point of 10mTorr), the MCS insulates the VU and monitors the pressure in the system for a fixed span; any increase of pressure with a rate higher than 1 mTorr/h is considered by the MCS as a loss of integrity of the system. In this case the MCS stop the process, drain the facility, insulate the SU and give an alarm message.

When the former phase is completed, the MCS starts with the further step, consisting in the filling of the capillary with the NaK alloy. The Handling Unit floods the lines of the FU and the NaK alloy begins to fill the connected capillary. A small overpressure is constantly maintained on the free level of the liquid metal in the vessel of the HU, to aid the process. Once the step is completed and the capillary are filled by the NaK, the MCS asks the user to close the capillary and to disconnect them from the feeding lines. The closure of the capillaries is preliminary performed pinching them. Then, each capillary is disconnected from its feeding union and its end closed by a locking screw cap.

After this, the user gives his confirmation to proceed and the MCS starts with the last phase of the cycle, draining the liquid metal to the SU and venting the lines of the FU by Argon. When the lines are vented, the user has to close their opened ends by a proper locking cup. Only after this the glove box can be opened and the sensors downloaded from the facility.

From this point, the manufacturing process of the sensors follow the same standard path adopted for the Mercury and Oil filled sensors, that consist in the completion with the electronic components and the closure in a standard steel case. After that, each sensor manufactured is tested and qualified, in order to produce all the documentation that will be supplied with it when delivered to the customer.

Working principle of a "Melt" pressure transducer

Different technologies in the field of pressure transducers are nowadays available for high temperatures applications. Among these, the one based on the use of a strain gauge coupled to a transmitting liquid is certainly the most popular. As known, one of the main issue in high temperature pressure measurement is the necessity to maintain at a relatively low temperature the sensible element of the instrument. The hydraulic transmission of the pressure by a proper media allow to solve this problem.

In Figure 6-16 a sketch of a sensor is reported. As shown, two thin membranes are connected by a capillary, filled by a liquid. The first membrane is directly exposed to the measurement environment, while on the top face of the second one a strain gauge is mounted.
When a pressure acts on the first membrane, it undergoes to a mechanical deformation that is hydraulically transmitted to the second one, since the filling liquid can be considered incompressible. Here, the mechanical deformation is converted in an output signal by the strain gauge. In fact, the strain gauge consists of a metallic grid onto a thin insulation layer. On the grid 4 resistors are arranged according to a Wheatstone Bridge; since a constant input is supplied to the bridge, a constant output is obtained. The mechanical deformation of the membrane results in a variation of the bridge resistance, giving an output proportional to the acting pressure.

Qualification of the prototypes

After the first operative cycle was completed, the manufactured sensors were tested in order to verify the obtained accuracy.
In general, the accuracy of a sensor gives a global information on the maximum error that will affect the measurement performed by the sensor itself. According to the CEI 65-4 (UNI 9546 or DIN 16086) it represent the combined error due to three contributes:

- Error of linearity
- Error of repeatability
- Error of hysteresys

The error of linearity gives information about how far is the real characteristic of a sensor from the theoretical linear behaviour. According to the CEI rules, it is possible to use two method to estimate this contribution:

- The End point Method
- The BSFL Method

In the first case the error of linearity is calculated as the difference between the real characteristic of the sensor and the straight line which runs from one extreme to the other of the characteristic itself. It is expressed in %, with reference to full scale. This is also reported as the “dependent linearity error”.

According to the second method, the error of linearity is calculated as the difference between the real characteristic of the transducer and the straight line which better approach the real curve, in the sense of least square roots. The error calculated in this way is also reported as the “independent linearity error”. It is expressed in % with reference to the full scale in this case too.

The error of repeatability gives information about the attitude of the sensor to reproduce the same output when the same pressure is applied, under the same conditions and the same direction (increasing or decreasing values of pressure).

The error of hysteresys is the maximum difference in output, at any measured within the specific range, when the value is approached first by increasing and then by decreasing the pressure.

In graph from Figure 6-13 to Figure 6-15 the three terms for the sensor characteristic, its lienearu error and hystersys.

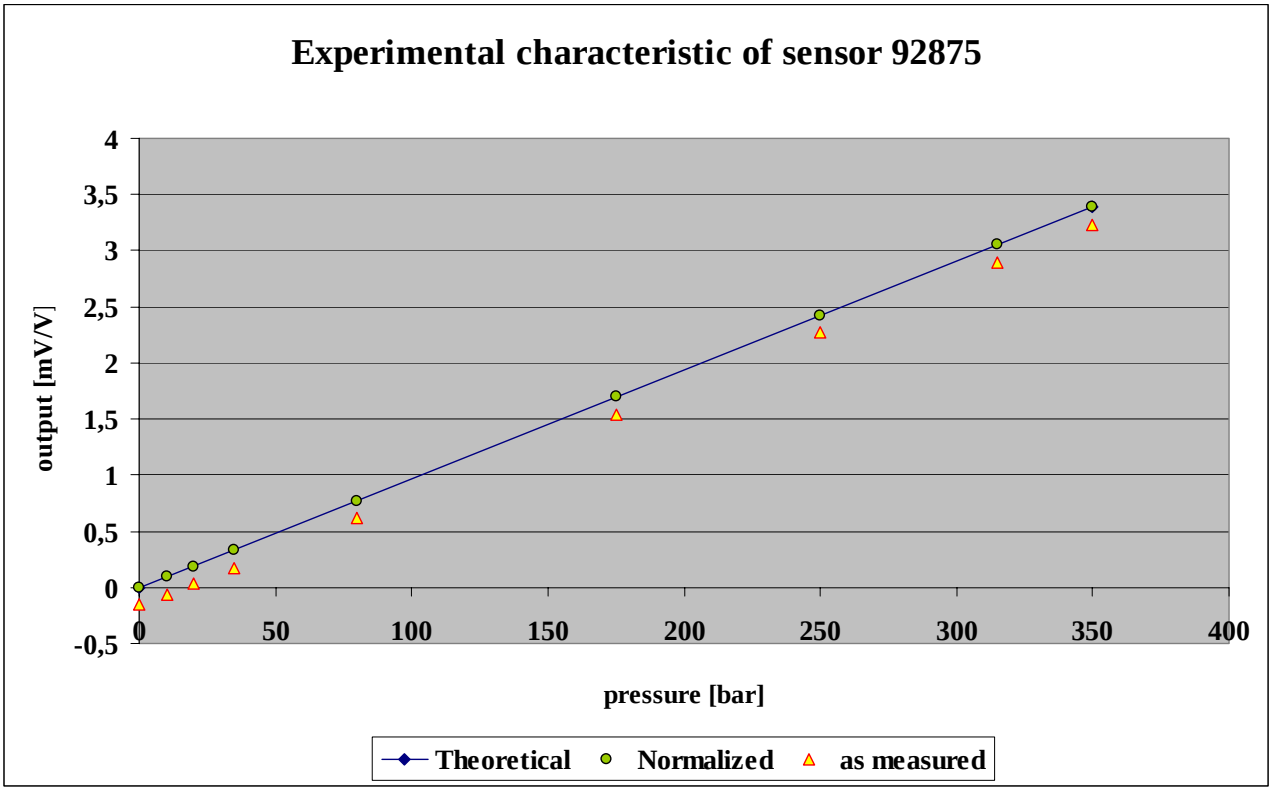

Figure 6-13– Experimental characteristic obtained for one of the five prototype manufactured. The "normalised" series is obtained by a simple translation of the measured points in order to have zero output when none relative pressure is applied.

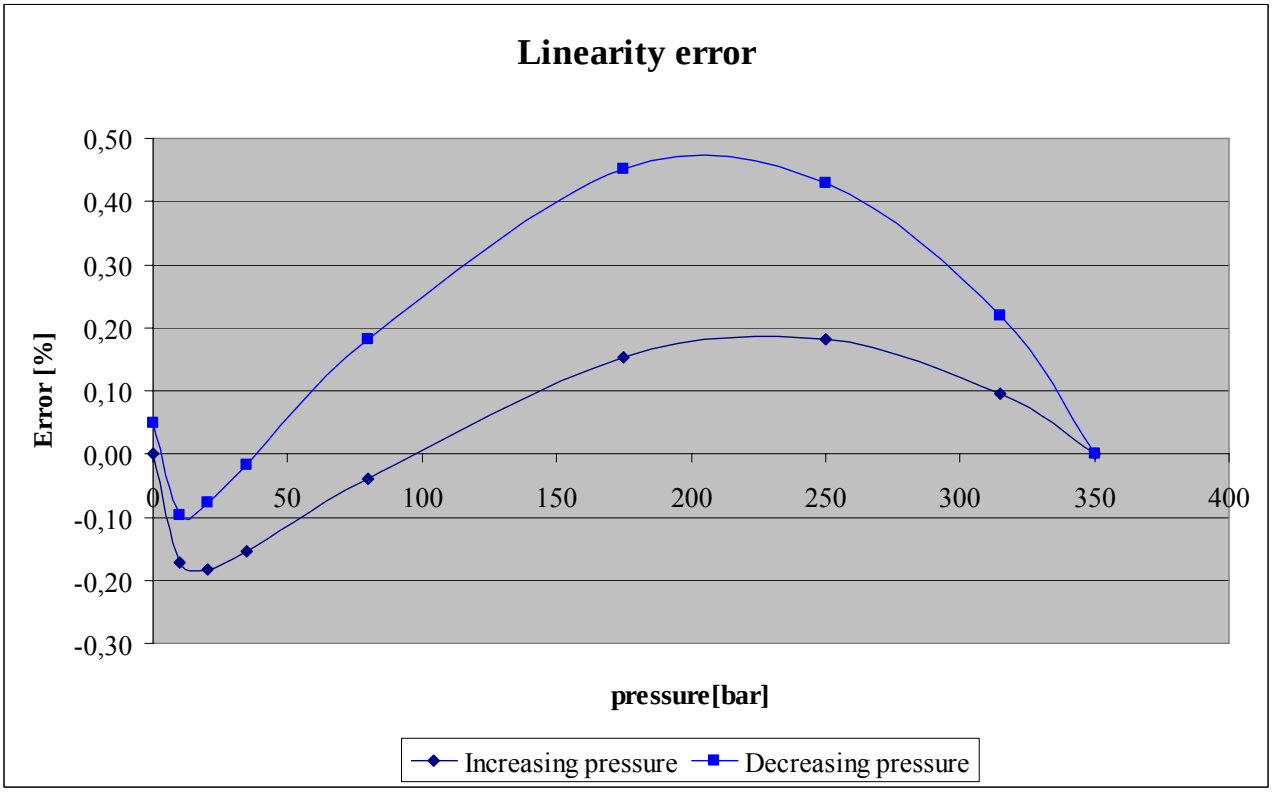

Figure 6-14 – Dependent linearity error for one of the three prototypes manufactured (n. 92875). All the five sensors show the same order of linearity error.

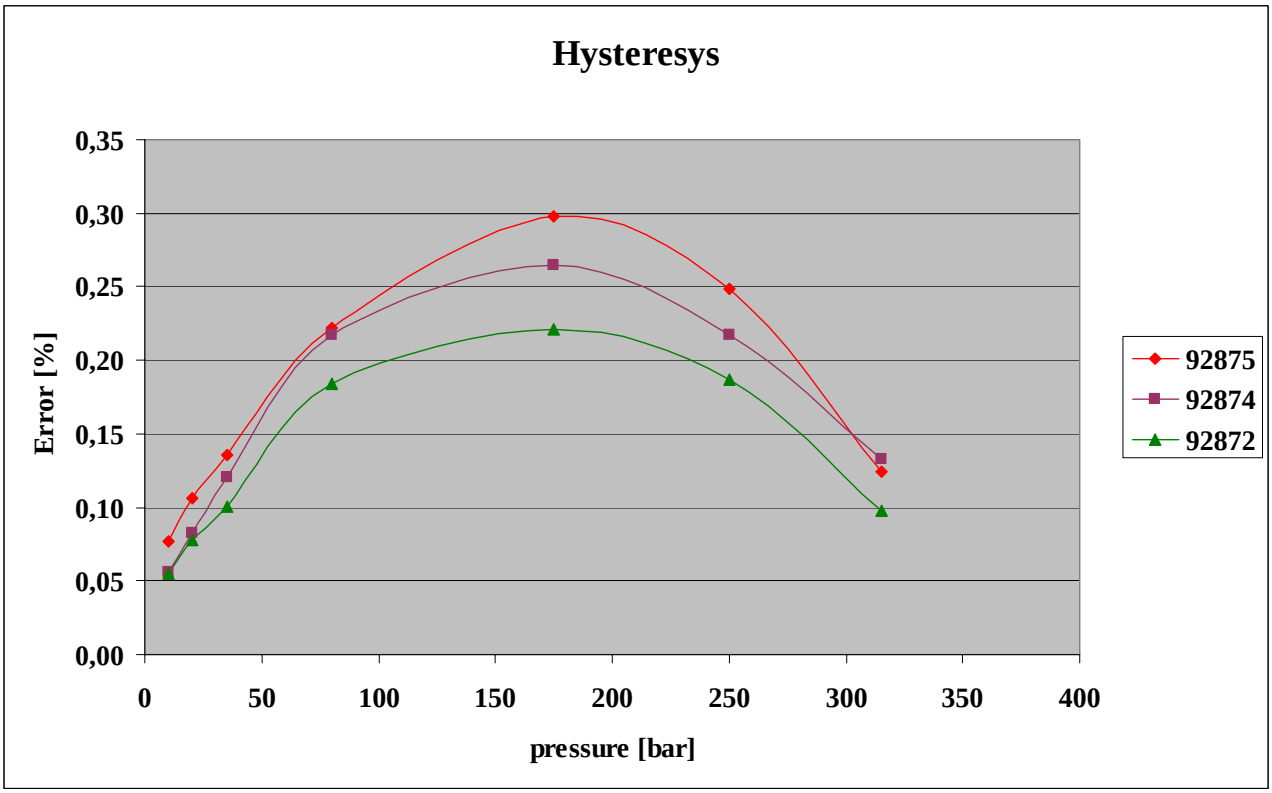

Figure 6-15 – Hysteresys error for the three prototypes manufactured.

Finally, the accuracy of the sensor can be expressed as:

$$Accuracy = \pm\sqrt{\frac{Linearity^2}{\sqrt{3}} + \frac{Hysteresys^2}{\sqrt{3}} + Repeteability^2}$$

For all the prototypes manufactured the accuracy is lower then 0.5 % of the full scale (note as, according to the previous definition, lower is the accuracy, higher are the performance of the sensor).

Another important parameter to take in account is the thermal drift of the characteristic. Also in this case the results obtained confirm the good quality of the sensors manufactured, being the drift lower than 0.03 bar/°C. Note as this value is 0.02 bar/°C in the case of the mercury filled sensors, while it is 0.04 bar/°C in the case of oil as filling fluid. As expected, the NaK sensor performances lies between the other two types.

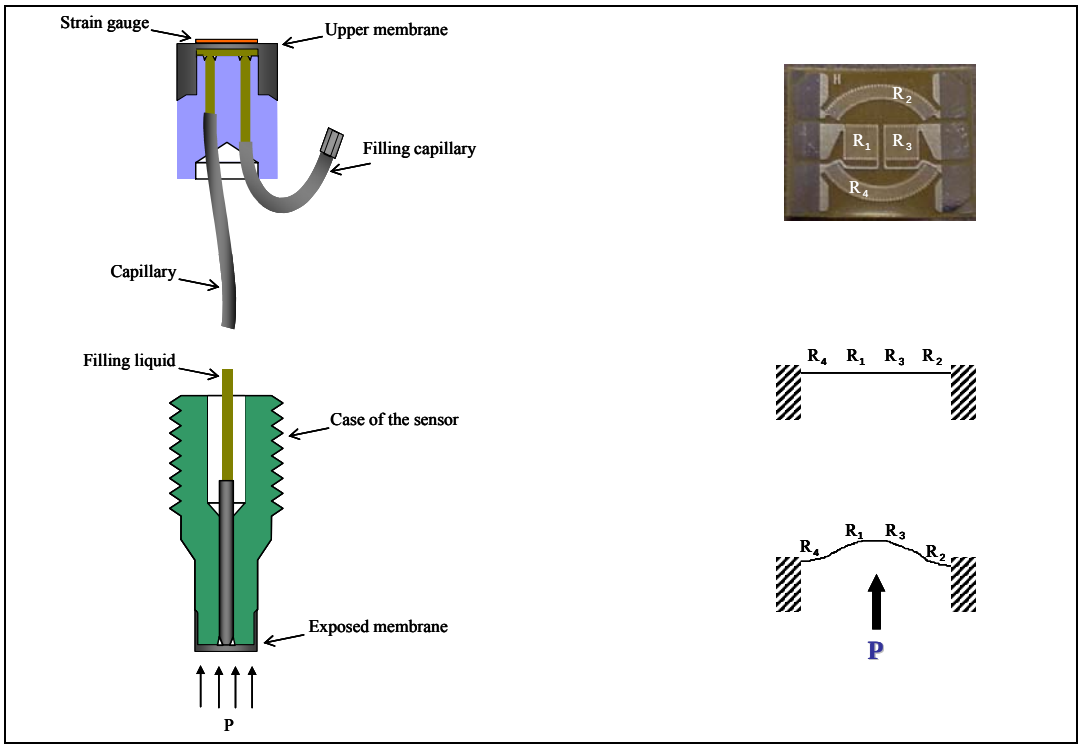

Figure 6-16– ***Sketch of a sensor (on the left);On the right: View of the strain gauge; when a pressure P acts on the membrane, the resistances R1 and R3 undergoes to a tensile stress, while R4 and R2 to a compressive stress. This results in a disequilibrium of the bridge and an output proportional to the pressure is obtained.***

Conclusion

A collaboration with GEFRAN S.p.A. started during the spring of 2005, aimed to investigate the possibility to use the NaK alloy as filling fluid for pressure transducer. Gefran was interested to improve its capability in offer high temperature pressure transducers for "melt" applications. Within this collaboration, the compatibility of the NaK alloy with the existing industrial manufacturing process has been evaluated; then, a suitable filling process has been developed and a dedicated small facility has been designed and realised.
From the test campaign performed in order to qualify the upgrade of some GEFRAN S.p.A. pressure transducers, it is clear that they fulfil the working behaviour requested.
Moreover, they are also able to work at higher temperatures then the previous sensors filled with Oil and Mercury.

Bibliografy

[8] J. Desreumaux, M. Calais Et al., *Eur. J. Inorg. Chem*., 2000, 2031-2045
[9] J. Desreumaux, *Physico Chemie du NaK,* Ecole du Sodium, 1995
[10] A. G. Mozgovoi, *High Temperature,* 41-3, 340-345
[11] N. E. Dubinin, A. A. Yuriev, *Thermodinamica Acta,* 316 (1998), 123-129
[12] K. Natesan, C.B. Reed, R.F.Mattas, *Fusion Engineering and design,* 27 (1995), 457-466.
[13] P. Sykes: *A Guidebook to mechanism in Organic Chemistry,* Longman Scientific, 1992
[14] R.O.C. Norman: *Principles of Organic Synthesis,* Chapman&Hall, 1982.
[15] T.W. Graham Solomons: *Organic Chemistry,* John Wiley & Sons, 1988.
[16] E.E. Shpil'rain et. Al., *High Temperature,* 39 (4) 2001, 511-517.
[17] E.E. Shpil'rain et Al., *High Temperature,* 41 (1) 2003, 23-31.
[18] H. Eslami, *International Journal of Termophisics,* 20 (5) 1999, 1575-1585
[19] S. Malang, H.U. Borgsted et Al., *Fusion Engineering and Design,* 27 (1995), 570-586.
[20] G. Abowitz, R.B. Gordon, *Journal of Chemical Phisics,* 37 (1), 1962.

7. Conclusion

Since the work performed during these three years covered different topics, which were developed in parallel, it is not possible to draw a general conclusion. Anyway it is possible to discuss the results of each activity as follows:

Enhanced circulation

The possibility to enhance the LBE circulation by gas injection has been confirmed in the CIRCE facility, that is representative of the reference ADS plant.
The results obtained show that for Ar flow rates higher than 1 Nl/s is possible to entrain a steady flow of LBE trough the test section adopted. A relation between the entrained liquid metal flow rate and the injected one has been carried out by best fit of experimental data.
This relation follows a power law and a theoretical justification of the result has been carried out too.
The second experimental campaign on the gas enhanced circulation has been successfully accomplished on the CIRCE facility. All the results obtained during the first campaign, in particular the possibility to establish a steady liquid metal flow rate higher than 200 kg/s, have been confirmed. However, at gas flow rate lower than 1Nl/s, the occurrence of instability phenomena has been confirmed too.
Differential pressure measurement allowed to obtain data on the localised loss of pressure as well as the distributed one. In particular, the results indicate that the loss coefficient related to a calibrated orifice located in the single phase region to simulate the loss of head of the reference core is not constant and depends from the liquid flow rate.
The loss of pressure measurements performed along the riser allowed to say that the pressure drop in the two phase region is essentially due to the gravimetric head, being the acceleration term negligible. Moreover, these measurement allowed to estimate the void fraction in the riser.
The analysis performed allowed to characterise the two phase flow that is responsible for the liquid circulation in the system.
The temperature of the liquid metal can be considered as a variable of secondary importance, being its influence on the circulation parameters very weak. For this reason, the characteristic curves obtained by best-fit of the experimental data are temperature independent.
The enhanced circulation has been described in terms of flow rate and volumetric flux curves and relations able to predict the response of the liquid phase to a defined injection of gas have been obtained.
Even if a direct observation of the flow pattern during the tests has not been possible, the results obtained give indirect information that suggest a kind of bubbly flow regime. Moreover, it seems consistent with the results the possibility of a flow pattern transition toward a churn-bubbly flow at gas flow rates higher than 8 g/s.
The information obtained on the void fraction as far as on the slip ratio confirm that the use of a separate flow model to describe the behaviour of the system is a good choice.
Finally, the analysis performed on this pumping technique highlighted the trend of the main important performance parameters, pointing out as the pumping power developed is close to a cubic function of the liquid flow rate and as the efficiency of the lift pump assumes its highest values in correspondence of a well defined range of the gas flow rate.

Aerosols qualification

The two different campaigns performed allow to confirm some literature information and to add something new to the knowledge of the phenomena.
In the first test with PIF I, the lead Bismuth has been reduced. When the test was stopped a negligible amount of dust was, actually, found. This confirms that the LBE vapour pressure contributes marginally to the formation of the power.
It is possible that some oxygen dissolved in the alloy. Anyway the total amount of powder was so few that it was not possible to weight it.
The SEM analysis showed that the few quantity of powder detected was composed mainly by Lead and Magnesium oxides.
It is possible to suppose that the presence of floating oxides on the free surface of the liquid metal obstacles the transfer of the oxides from the liquid to the gas.
In the second campaign a mixer was installed in order to fight the crust formation and to simulate the real liquid turbulence in a pump tank or in a pool configuration facility.
From this first run some very interesting data were collected and it was possible to find a correlation between the powder production rate vs the time, at fixed temperature and O_2 concentration (ref Figure 4-13)
In the future, new test are foreseen in order to confirm the first test outcome.

Oxygen monitoring and control

In PbBi, the two $Bi|Bi_2O_3$ sensors gave signals which were in good accordance with the theoretical ones in both plants. Also the $In|In_2O_3$ sensor gave outcome signals coherent with the theoretical data.
Moreover the two sensors gave coherent signals in similar working conditions, allowing to start the design of a sensor for a pool configuration.
That led to the design and construction of an oxygen sensor adapt to pure Lead. In this case it was a technological innovation since, up to now, few data are available. The $Bi|Bi_2O_3$ sensor was recalibrated in pure lead and showed a behaviour comparable to the one in PbBi. Only the magnitude of the outcome signal is slightly lower than in the LBE case.
The next step is to design and construct an oxygen sensor for a pool type reactor. This sensor will be tested in the frame of experimental campaigns, which will be performed in the CIRCE facility next year.

Industrial application

A collaboration with GEFRAN S.p.A. started during the spring of 2005, aimed to investigate the possibility to use the NaK alloy as filling fluid for pressure transducer. Gefran was interested to improve its capability in offer high temperature pressure transducers for “melt” applications. Within this collaboration, the compatibility of the NaK alloy with the existing industrial manufacturing process has been evaluated; then, a suitable filling process has been developed and a dedicated small facility has been designed and realised.
From the test campaign performed in order to qualify the upgrade of some GEFRAN S.p.A. pressure transducers, it is clear that they fulfil the working behaviour requested.
Moreover, they are also able to work at higher temperatures then the previous sensors filled with Oil and Mercury.

General remarks

As a general remark it is possible to say that in these years the technology related to the liquid metal system has been developed and completed even if a lot of work is still needed.
This allow to foresee a future application in the realization of the new generation nuclear plants such as GIV reactors and ADS.
An important outcome of this work is also the transfer and adaptation of the know how gained about the liquid metals in the nuclear field to an industrial application.

I. APENDIX: The CIRCE facility

Intoduction

In support of the HLM cooled ADS design, R&D activity programs are in progress all over the EU. ENEA is strongly involved in these activities, and many loops and devices have been operated in order to perform studies on material compatibility, chemical control, thermal hydraulic and other specific topics to produce data needed for the design.

In this frame has been realized and operated the CIRCE (CIRcuito Circolazione Eutettico) facility, to perform large-scale tests in flowing lead-bismuth eutectic (LBE). Actually, CIRCE is a large test facility, located at the Brasimone ENEA Research Centre (near Bologna), in principle designed to operate with liquid LBE and aimed to verify key operating principles of the LBE cooled 80 MWth Experimental Accelerator Driven System (XADS). For instance, some of the main topics for CIRCE are to verify the possibility to assure a reliable chemical control of the melt in order to prevent or minimize the corrosion issues as well as to study the natural circulation and the gas-injection enhanced circulation.
In particular, the injection of argon in the riser channels above the core is considered of main importance in the design of the LBE cooled XADS, to safely remove the heat produced by the fission reaction chain in the subcritical core.
Then, one of CIRCE main goals is to investigate and confirm the possibility to use this technique to obtain a steady flow of liquid metal in representative conditions for the 80 MW XADS.

Description of CRICE

CIRCE is a large test facility, located at the Brasimone ENEA Research Centre (near Bologna), designed to operate with liquid lead-bismuth eutectic (LBE) and aimed to verify key operating principles of the LBE cooled 80 MWth Experimental Accelerator Driven System (XADS). In particular, the aim of the facility is to perform experimental activities to investigate the hydraulic, chemical and mechanical issues related to the development of the LBE-cooled XADS in a pool configuration [15][16].

It basically consists of a Main Vessel (S100), capable of about 90 tons of LBE and able to house different test sections. Actually, S100 have been designed to scale the LBE cooled XADS. In fact, it is a reduced diameter (1:5 the 80 MWth XADS vessel diameter), full-height cylindrical vessel, capable of about 90 tons molten LBE, with argon cover gas and recirculation system, LBE heating and cooling systems and auxiliary equipment for eutectic circulation [10]. In its final configuration CIRCE will simulate the whole thermal hydraulics of the primary and secondary XADS systems, and will be able to perform an active chemical control of the melt (for corrosion protection of the austenitic stainless steel structures), as planned for the ICE activities.

The facility is complete of a LBE storage tank (S200), of a small LBE transfer tank (S300) and of the data acquisition system, as more in detail described in the further paragraphs.

CIRCE main components and systems

The facility can be considered made up of two parts, dedicated to the LBE containment and management the first, and consisting of the auxiliary systems the other. In figure 2.1 an isometric view of the facility is shown, whereas in Figure i-2 the P&I of the plant is displayed.

Concerning the first part, the main components are: the test vessel S100, the storage tank S200 and the intermediate vessel S300, used during the handling of the LBE between the two other vessels: during the load operations, the LBE is gradually transferred from the storage tank to the S300 vessel. Then, by the pressurization of the S300 cover gas the liquid metal is moved to the test vessel. In this way, step by step, the test vessel is gradually filled from the bottom. The synoptic panel of the management program for the LBE transfer between the storage tank and the main vessel is shown in Figure i-3

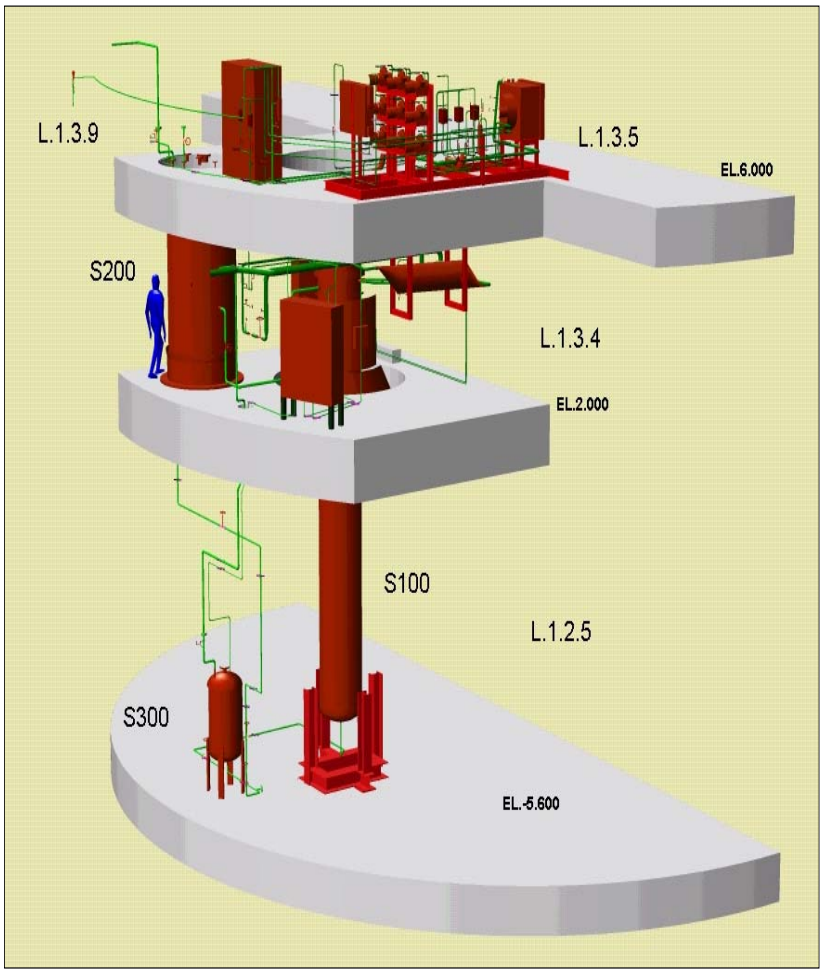

Figure i-1- CIRCE isometric view

Parameters	value
Main Vessel	
Outside Diameter, mm	1200
Wall thickness, mm	15
Material	AISI 316L
Max LBE inventory, kg	~ 90000
Electr. Heat tracing, kW	47
Cooling air flow rate, Nm^3/s	3
Temperature range, °C	200 to 550
Pressure	
Operating, kPa (gauge)	15
Design, kPa (gauge)	450
Argon gas	
Max Flow rate, Nl/s	7.5
Injection pressure, kPa (gauge)	600

Table 3- CIRCE main parameters

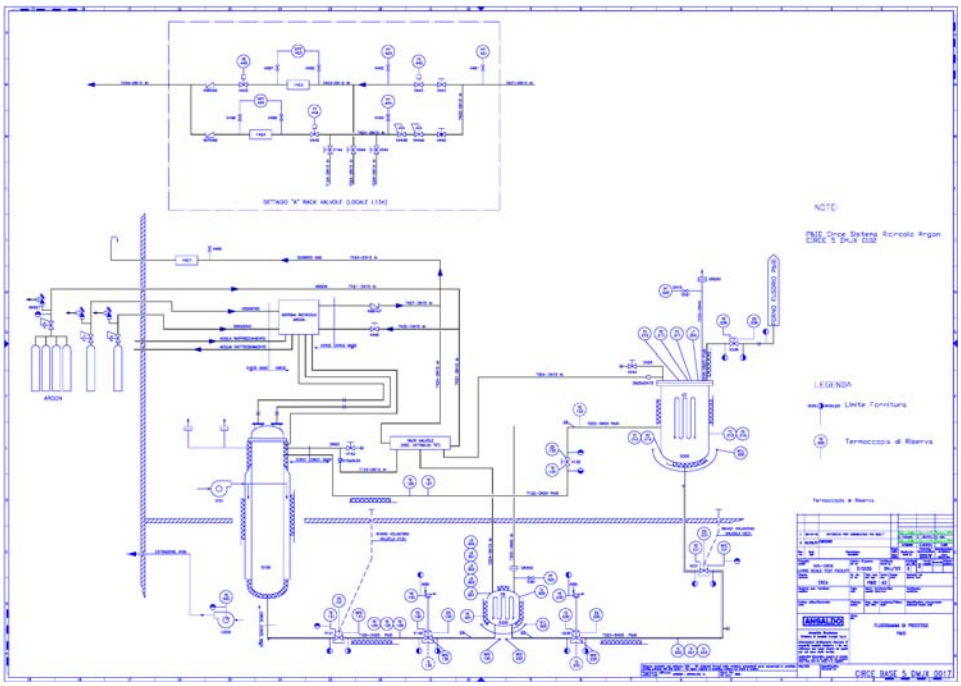

Figure i-2- P&I of the CIRCE facility

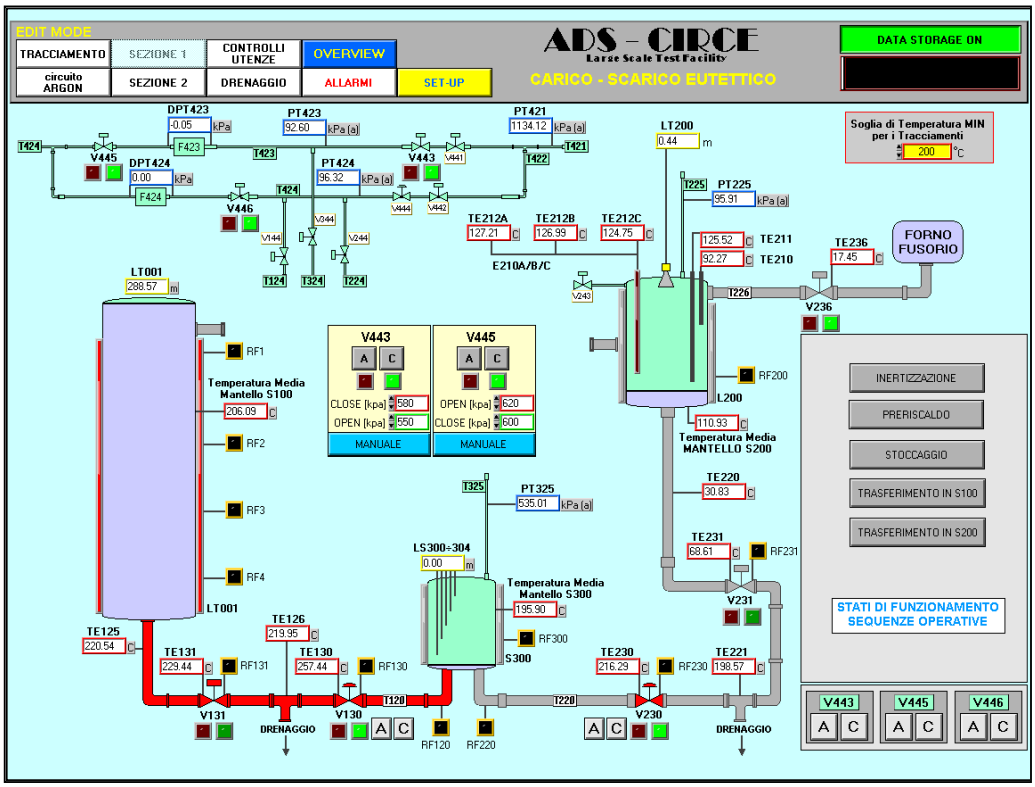

Figure i-3- Synoptic panel of the LBE transfer between storage tank and main vessel

The main vessel S100 consists of a vertical vessel 8.5 m height, connected by gates to the other systems, both LBE and gas side. It is equipped with electrical heating cables, installed on its bottom and cylindrical surface. This heating system allows to operate in the nominal temperature range of 200 ÷ 400°C, as required by test specifications. However, an improvement of the heating system has been planned, since the future experiments foreseen on the plant will concern an integrate Hot source - Cold sink system, characterised by a nominal thermal power of 750 kW.

Heat insulators cover all the external surface, except the top ferrule. Actually, this top part is arranged to assure the possibility of a quite fast cooling by forced air circulation, if required. The heating insulator thickness was calculated to limit heat dispersions toward the housing room. Then, in order to prevent any injury to the plant staff, the max temperature allowed on the external surface of components is 50 °C

The main vessel is also equipped by a skimming line and passive pressure safety system, in order to guarantee the LBE top level and to prevent accidental overpressures. The main parameters relevant to the test vessel are listed in Table 3.

Pressure and level measurement systems

In the CIRCE plant, small diameter gas injection tubes (shortly “bubble tubes”) have been installed to transfer pressure signals from the Pb-Bi alloy to differential pressure cells operating with gas at room temperature. The use of standard instrumentation can be difficult, mainly due to the thermal and chemical interactions between the LBE and the measurement devices. For this reason, a simple measurement technique based on “bubble tubes” has been tested in a dedicated device and finally applied to the CIRCE facility. In fact, bubble tubes injecting argon below the molten metal level,

have been installed to transfer pressure signals from the LBE alloy to differential pressure cells operating with gas at room temperature. In such a way, level, pressure and differential pressure measurement are performed in the CIRCE pool
In particular, the Level Measurement System (LMS) and the Differential Pressure Measurement System (DPMS) make use of the above instruments to perform their tasks.
To calibrate this instrumentation, which is innovative in the field of molten LBE, a small-scale auxiliary apparatus has been used [9] .

The Argon recirculation system

The Argon Recirculation System (ARS) take part in the experimental tests execution, as required in test specifications [11]. Its main goal is to feed and recirculate the cover gas in upper plenum of S100, as well as to provide gas during the tests if required and for the instrumentation. However, the system feeds the cover gas of the storage vessel and of the transfer vessel too. The main parts of the system are:

1) Main Vessel cover gas
2) Test section n1 distribution lines
3) Test section n2 distribution lines
4) Compressors set

Moreover, mechanical filters have been recently included in the system, to prevent that powders and aerosol, whose formation could take place from the melt in the main vessel during normal operations, could reach the blowers, causing plugs and fault. Indeed, the installation of filters based on silica gel to prevent moisture contamination in the melt has been planned too, in order to build up an effective purification system for the chemical control of the liquid metal.

By mean of a flexible metallic sheathing an injection line connects the main distribution line directly to the top of the main vessel. This line is then completed by each test section distribution line to, to provide atmosphere washing before the LBE loading and to feed all the utilities integrated in the test sections, such as the bubble tubes of the DPMS and LMS.

The test section N° 1 distribution line consists of a pressurization / depressurization pipe, connecting the inner compartment of the test section to the main distribution system. A vent line is also included, to allow the Ar flow toward the outer compartment cover gas. A metallic drilled disk, R03, with calibrate hole is installed on this line (see Figure i-4), to induce a controlled gas flow during the Venturi-Nozzle calibration tests. The distribution line also feeds the bubble tubes of the DPMS and LMS
The test section N° 2 distribution system consists of a suction pipeline from the main vessel to the compressors set and a delivery line from the compressors set to the main vessel, were it feeds the injection line integrated in the test section. A connection line between the test conduit and the CIRCE's gas dump line completes the system.

The compressor set consists of five positive displacement blowers; by a suitable management of the blowers and the by pass line, it is possible to cover a range of gas flow rates from 0.056 to 7.5 Nl/s. In Fig.4 the synoptic panel of the ARS is shown.

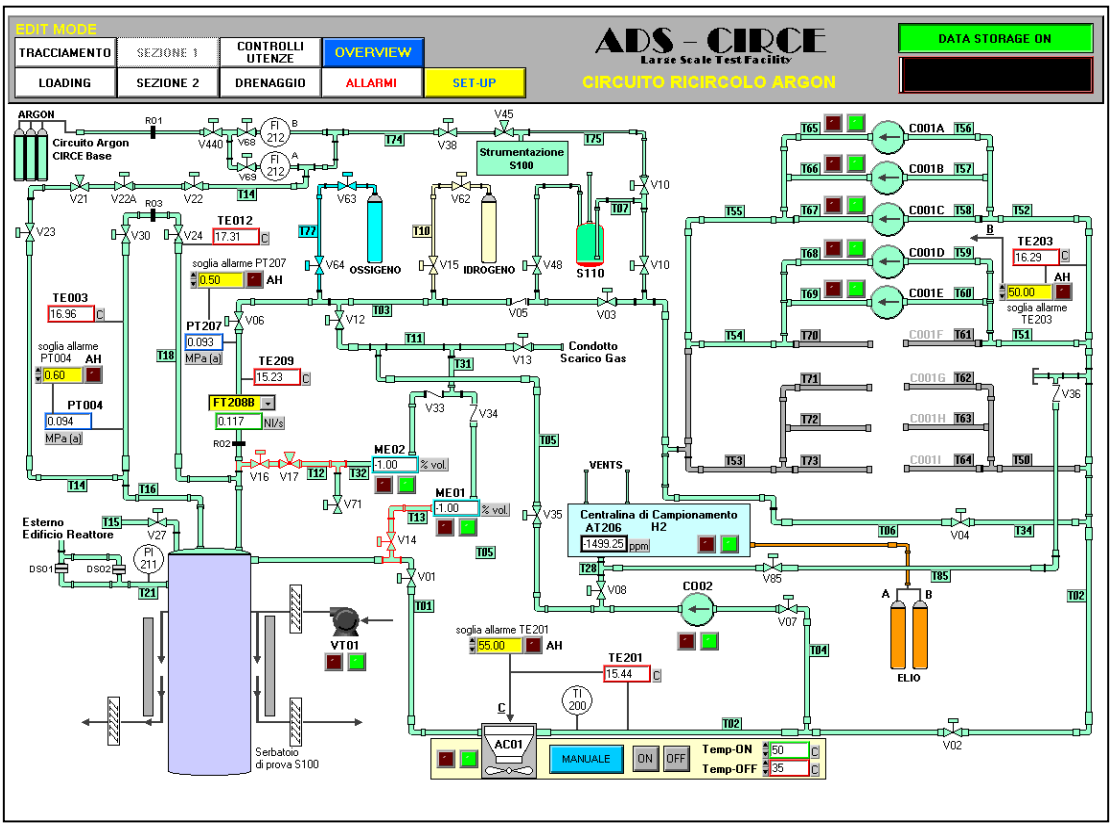

Figure i-4- Synoptic panel of the Argon Recirculation System. Note the line used during the tests for the calibration of the flow meter, on which the disk R03 is installed

Gas injection system

The Gas Injection System (GIS) is a subsystem of the Argon Recirculation System (ARS); it consists basically of the injection line integrated in the test section n°2, connected upstream to the compressor set of the ARS. This connection is realized by mean of a "flow measurement block" (see figure, consisting of three parallel lines equipped by gas flow meters of different measurement range. Downstream this block the main injection line reaches the upper flange of the main vessel, then it runs inside the riser. The line ends at the bottom of the riser with an "U" bend on which an injection nozzle is installed

Concerning the gas flow meters [12], they have different measurement range as previously reported. In particular the first flow meter (FT208A) works in the range [0.056÷0.56 Nl/s], the second (FT208B) in the range[0.35÷3.5 Nl/s], while the third works in the range [2.2÷22 Nl/s].

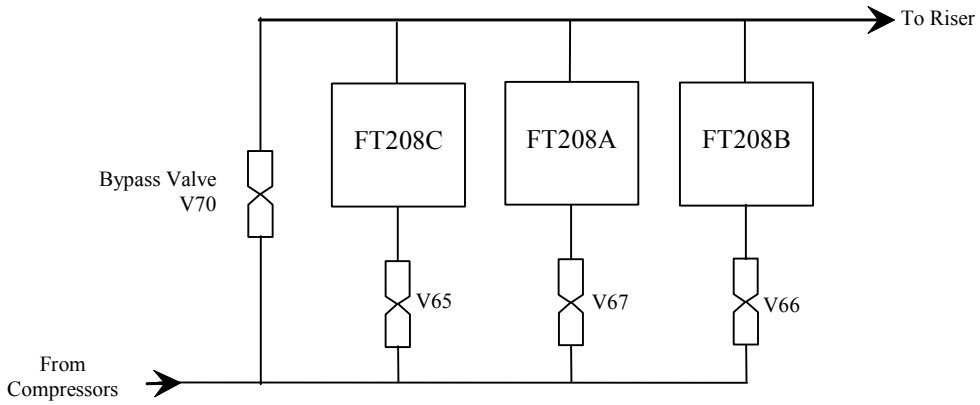

Figure i-5- Sketch of the flow measurement block of the GIS.

The Data Acquisition System

The Data Acquisition System (DAS) is based on National Instruments data input instrumentation and uses a computer program written in Bridge View, a particular and well known version of Lab View. The main components of the DAS are:

- Personal Computer
- Analogical and digital acquisition and processing modules
- Digital output modules, to control the installed instrumentation by interface device (electric board)
- Analogical output modules, 4-20 mA signal to regulate the installed instrumentation by interface device (electric board)
- I/O boards to perform the connection to the PC
- Data acquisition and processing boards
- Printer

All the input signal are processed by the acquisition modules and then elaborated by the acquisition board. The user interface is based on synoptic pages that allow to controls all the measured variables, as well as to set the parameters relevant to the data storage. A synoptic page of the operating test section is available too, to follow the evolution of the most important variables during the tests. The system stores all the acquired data in the PC hard disk.

Bibliografy

[9] C. Foletti, G. Scaddozzo, M. Tarantino, A. Gessi, G. Bertacci, P. Agostini ,G. Benamati – "Italian experience in LBE technology**"** – 2006 "*International Journal of Nuclear Materials";*

[10] CIRCE 1 SIEX 0001, General Specifications rev 2 (in Italian), 8/06/2001, DNU-STL

[11] Report ANSALDO CIRCE5SMFX0090, Rev.1, Design Specification of the Argon Recirculation System (in Italian)

[12] Report ANSALDO CIRCE 8 SATX 0129, "*Specifica tecnica di approvvigionamento: misuratori di portata sul circuito di ricircolo dell'argon*", February 2001 (*in Italian*);

Acknowledgements

There are definitely many people I feel to thank because of they have been, in different ways, strongly supporting this activity or helping me over these years. It is a pleasure for me to recall and to express my gratitude to the following people:

Prof. S. Salvigni Università di Bologna (My supervisor)
Prof. E Lorenzini Università di Bologna
Eng. G. Benamati ENEA-Brasimone
Eng. P. Agostini ENEA-Brasimone
Eng. Marcello Perini – GEFREAN SpA
Eng. Marco Casati - GEFREAN SpA
Mr. M. Agostini ENEA-Brasimone
Mr. G. Bertacci ENEA-Brasimone
Dr. F.DiGabriele NRI-Rez
Dr. A. Aiello ENEA-Brasimone
Dr. I. Ricapito ENEA-Brasimone

Many tanks also to the friends and colleagues of the research team with whom I worked with during these years: Andrea Ciampichetti, Alessandro Gessi, Mariano Tarantino, Silvia De Grandis, Donella Pellini Zhang Ping Zhu and Egor Machula.

A special thank goes to the friends who supported me in these last months: Luigi Andrea, Giuseppe, Marco and Fosca, I want to thank them first of all for their friendship and also for their scientific support.

I had not the possibility to perform this work without the support and the love of my family.